POLITECNICO
MILANO 1863

SCHOOL OF INDUSTRIAL ENGINEERING AND INFORMATION
DEPARTMENT OF AEROSPACE SCIENCE AND TECHNOLOGY

Master of Science in Space Engineering

# Design and Simulation of an Experimental Pulse Detonation Engine Setup

Academic Year 2024-2025

**Alessandro Cannavò** 10742675
Relatore: Federico Piscaglia
Supervisor: Francisco Sastre Matesanz

# Abstract

Pulse Detonation Engines (PDEs) offer a promising alternative to traditional propulsion systems due to their higher thermodynamic efficiency, reduced weight, and more compact design. However, their practical implementation remains challenging, primarily due to the harsh detonation environment and the complexity of modelling unsteady flow phenomena. This thesis focuses on the selection, specification, and simulation of components for a PDE experimental setup using hydrogen and air as propellants. Drawing from existing setups, critical elements such as valves, sensors, and protective cooling systems are chosen to ensure robustness and adaptability. A key innovation of this work lies in the design's enhanced versatility for future adaptation to Rotating Detonation Engines (RDEs). Unlike previous setups, this configuration introduces piezoresistive pressure transducers—also suitable for RDEs—and advanced diagnostics such as ion probes and Background-Oriented Schlieren imaging, replacing conventional methods to improve measurement accuracy and system insight. A comprehensive Simulink® model simulates the behaviour of the selected components to assess their influence on flow conditions and engine performance. Key metrics such as pressure and temperature along the feeding line are analysed, highlighting the non-negligible effects of even small inefficiencies. The simulation also enables performance evaluations under varying operational conditions, such as detonation frequency and setup dimensions. This modelling approach provides valuable insight into the interplay between component behavior and overall engine performance and serves as a reference for physical implementation. The findings support the practical realization of PDE systems and provide a pathway for extending the approach to RDE configurations.

Key-words: Pulse Detonation Engines, Rotating Detonation Engines, Hydrogen-Air Detonation, Experimental Setup Design, Simulink Modelling, Thermodynamic Performance Evaluation

# Sommario

I motori a detonazione pulsata (Pulse Detonation Engines, PDE) rappresentano un'alternativa promettente ai sistemi di propulsione tradizionali, grazie alla loro maggiore efficienza termodinamica, al peso ridotto e al design più compatto. Tuttavia, la loro implementazione pratica risulta ancora complessa, principalmente a causa dell'ambiente estremo generato dalla detonazione e della difficoltà di modellare i fenomeni di flusso non stazionario. Questa tesi si concentra sulla selezione, specifica e simulazione dei componenti per un banco prova sperimentale di PDE, utilizzando idrogeno e aria come propellenti. Basandosi su configurazioni già esistenti, sono stati selezionati elementi chiave come valvole, sensori e sistemi di raffreddamento protettivi, con l'obiettivo di garantire robustezza e adattabilità.

Un'innovazione fondamentale di questo lavoro risiede nella maggiore versatilità del design, pensata per un futuro adattamento ai motori a detonazione rotante (Rotating Detonation Engines, RDE). A differenza delle configurazioni precedenti, questa implementazione introduce trasduttori di pressione piezoresistivi — compatibili anche con gli RDE — e sistemi diagnostici avanzati, come sonde a ioni e imaging Background-Oriented Schlieren, che sostituiscono i metodi convenzionali migliorando la precisione delle misure e la comprensione del sistema. Un modello completo in Simulink® simula il comportamento dei componenti selezionati per valutarne l'influenza sulle condizioni di flusso e sulle prestazioni del motore. Vengono analizzati parametri fondamentali come pressione e temperatura lungo la linea di alimentazione, evidenziando gli effetti non trascurabili anche di piccole inefficienze. La simulazione consente inoltre di valutare le prestazioni al variare delle condizioni operative, come la frequenza di detonazione e le dimensioni dell'impianto. Questo approccio modellistico fornisce indicazioni utili sull'interazione tra il comportamento dei singoli componenti e le prestazioni globali del motore, e rappresenta un valido riferimento per l'implementazione fisica del sistema. I risultati ottenuti supportano la realizzazione pratica dei PDE e aprono la strada a un'estensione metodologica verso le configurazioni RDE.

Parole chiave: Motori a Detonazione Pulsata, Motori a Detonazione Rotante, Detonazione Idrogeno-Aria, Progettazione del Banco Prova Sperimentale, Modellazione con Simulink, Valutazione delle Prestazioni Termodinamiche

# Acknowledgments

I would like to express my sincere gratitude to Professor Sastre for the enriching experience in Madrid and for generously sharing his knowledge with me. My thanks also go to Professor Piscaglia in Milan for his guidance as my thesis advisor.

I am deeply grateful to my parents and grandparents for their unconditional support, for always believing in me, and for making my dreams possible.

I am also thankful to all those who have supported me along the way: Matilde, Flavio, Meri, Alex, Lorenzo, Said, Giorgia, Matteo, Alessandro and Tommaso.

To everyone I met in Milan and Madrid—thank you for making these two unforgettable experiences so meaningful. Muchas gracias de verdad.

Finally, I want to acknowledge the sources of inspiration that have guided me throughout life: Stephen Hawking, Margherita Hack and Lady Gaga.

# Contents

# List of Figures

# List of Tables

# Acronyms

| Symbol | Description |
|---|---|
| $BOS$ | Background-Oriented Schlieren |
| $BR$ | Blockage Ratio |
| $CEA$ | Chemical Equilibrium with Applications |
| $CFD$ | Computational Fluid Dynamics |
| $D$ | Tube Diameter |
| $DAQ$ | Data Acquisition System |
| $DDT$ | Deflagration-to-Detonation Transition |
| $E_{max}$ | Peak Thrust |
| $EMF$ | Electromotive Force |
| $EMI$ | Electromagnetic Interference |
| $f$ | Detonation Frequency |
| $FFT$ | Fast Fourier Transform |
| $FS$ | Safety Factor |
| $GSC$ | Grid-Side Converter |
| $HOSVD$ | High-Order Singular Value Decomposition |
| $I_{sp}$ | Specific Impulse |
| $I_T$ | Total Impulse Per Cycle |
| $L$ | Tube Length |
| $MRAC$ | Model Reference Adaptive Control |
| $MSC$ | Machine-Side Converter |
| $M_T$ | Ejected Mass Per Cycle |
| $P_0$ | Initial Pressure |
| $P_{max}$ | Peak Pressure |
| $PDE$ | Pulse Detonation Engine |
| $PIV$ | Particle Image Velocimetry |
| $PLL$ | Phase-Locked Loop |
| $PTFE$ | Polytetrafluoroethylene |
| $p.u.$ | Per Unit |
| $PWM$ | Pulse Width Modulation |
| $RDE$ | Rotating Detonation Engine |
| $RDW$ | Rotating Detonation Wave |
| $RFI$ | Radio Frequency Interference |
| $RMS$ | Root Mean Square |
| $ROM$ | Reduced Order Model |
| $T_0$ | Initial Gas Temperature |
| $t_{off}$ | Relaxation Time |
| $TTL$ | Transistor-Transistor Logic |
| $VDC$ | Direct Current Voltage |
| $\phi$ | Equivalence Ratio |

# Chapter 1

## 1 Introduction

The objective of this thesis is to develop an experimental test rig for pulse detonation engines (PDEs). Beyond its academic significance, this work has practical implications, as the actual implementation of a test setup is planned. This research is part of a project supported by the European Space Agency (ESA), involving several institutions and universities, including the Universidad Politécnica de Madrid. In recent years, interest in pulse detonation technology has grown substantially, particularly in Europe. A PDE is a type of propulsion system that uses detonation waves to combust the fuel and oxidizer mixture: the engine is pulsed since the mixture must be renewed in the combustion chamber between each detonation wave. This increasing focus is driven by the numerous advantages associated with this technology. The key advantages of PDEs include:

- higher thermodynamic efficiency;
- high-energy heat release and substantial thrust generation;
- high specific impulse;
- fewer moving parts compared to conventional propulsion systems;
- hardware simplicity;
- capability to operate over a broad range of flight Mach numbers (from 0 to 5) for air-breathing PDEs. Currently, no single cycle engine exists which has such a broad range of operability;
- reduced weight and compact design, requiring less packaging volume than conventional engines due to inherent simplicity.

Higher thermodynamic efficiency is due to the rapid compression of the fuel-air mixture by a detonation wave, which enables heat addition at constant volume. This mechanism is detailed in Section 1.3. As a result, PDEs do not require conventional moving components such as compressor spools, leading to potential reductions in weight, cost, complexity and possible failures. Moreover, the propellant injection pressures are expected to be much lower than conventional rocket engines, which has the added advantage of eliminating the need for heavy and bulky turbopump machinery that drive propellant feed systems. Despite these advantages, the practical implementation of PDE technology remains challenging. Accurately modelling its operation and capturing the complex physical interactions involved is difficult. As a result, no fully operational PDE-based propulsion system currently exists, and significant research efforts are ongoing to overcome these challenges.

### 1.1 Applications

The primary applications of PDEs include the following:

- military applications: due to their lightweight design and superior performance around Mach 1 compared to existing engine technologies, PDEs are well-suited for propulsion systems in missiles, unmanned aerial vehicles and other small-scale applications. Research in this area is actively being conducted at the NASA Glenn Research Center;

- hybrid pulse detonation propulsion: PDEs can be integrated with turbofan and turbojet engines to create hybrid propulsion systems. This combination has the potential not only to enhance aircraft speed but also to improve efficiency and reduce environmental impact. Theoretically, nitrogen oxide emissions could be reduced by up to 80%;
- space propulsion systems: PDEs have the potential to significantly reduce the cost and complexity of upper-stage and orbit-transfer propulsion systems. Unlike conventional systems, they do not require heavy and expensive pumps and offer improved fuel efficiency. When combined with other propulsion technologies, PDEs could lower the cost of launching payloads into space. Additionally, they are promising for lunar and planetary exploration, particularly for landers and excursion vehicles that require precise throttling for soft landings;
- attitude control for microsatellites: the compact design, miniaturization potential, and ability to generate precise impulse bits in the order of 10 µNs make PDEs suitable for high-precision attitude control in microsatellite applications.

## 1.2 Operating Principles

PDEs operate on the principle of detonation, a phenomenon in which a shock wave is sustained by the energy released during combustion. The combustion process is initiated by the compression induced by the shock wave, which results in high temperatures. Consequently, a detonation arises from the interaction between a hydrodynamic process (the shock wave) and a thermochemical process (combustion).

A detonation can be triggered by igniting a combustible mixture at the closed end of a long tube that is open at the opposite end. As the flame propagates through the mixture, it accelerates due to the expansion of the burned gases confined between the flame front and the closed end. This acceleration leads to the formation of a shock wave that precedes the combustion zone, propagating at supersonic velocities. Thus, a detonation is a violent chemical reaction that travels through the reacted material toward the unreacted material at supersonic speeds.

Detonations enable extremely rapid material and energy conversion. This high reaction rate—or burning rate—does not allow sufficient time for the local expansion of combustion products. As a result, the detonation process thermodynamically approximates a constant-volume process rather than the constant-pressure process characteristic of conventional deflagration based propulsion systems. The higher thermodynamic efficiency of the nearly constant volume combustion process (detonation) stems from the lower entropy increase in the working fluid compared to the constant pressure (deflagration) combustion, as it is illustrated later in this section.

The high-pressure ratios inherent in detonation combustion may eliminate the need for expensive, high-pressure feed systems, thereby reducing the propulsion system's weight, complexity, cost and packaging volume, as mentioned above, among the advantages of this technology. Furthermore, the rapid energy conversion associated with detonation combustion facilitates the development of more compact and efficient propulsion system designs compared to conventional systems currently in use. Figure 1 illustrates a control volume containing the detonation wave, modeled as a strong shock that rapidly compresses the reactants to initiate combustion.

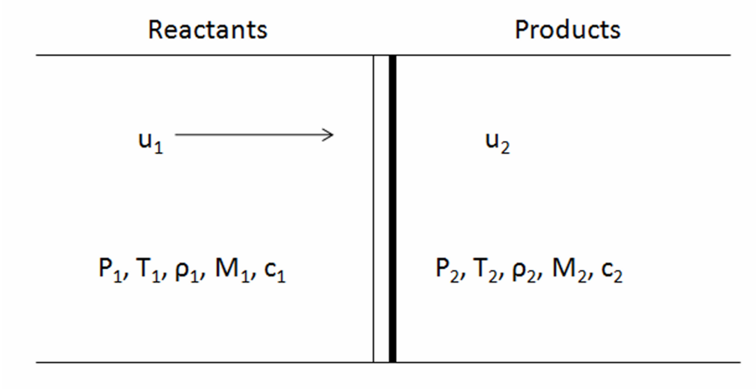

Figure 1: One dimensional detonation wave in a constant-area duct [1]

Qualitative differences between the upstream and downstream properties across the detonation wave are, for the most part, similar to those observed across a conventional normal shock. The primary distinction lies in the downstream velocity: while a normal shock always results in a subsonic downstream velocity, the velocity of a detonation wave is always equal to the speed of sound in the burned gases through which it propagates, which remains constant.
A useful comparison is provided in Table 1 , which presents upstream and downstream Mach numbers along with the ratios of downstream-to-upstream properties. The data illustrate that the property ratios for a normal shock are qualitatively similar to those for a detonation and are of the same order of magnitude. In contrast, a comparison between deflagrations and detonations reveals significant differences: across a deflagration front, the Mach number increases, the velocity rises substantially and the density decreases significantly. These effects are opposite in direction to those observed in both shocks and detonations.

| Property | Normal shock[a] | Detonation | Deflagration[b] |
|---|---|---|---|
| $M_1$ | 5.0 | 5–10 | 0.001 |
| $M_2$ | 0.42 | 1.0 | 0.003 |
| $v_{x,2}/v_{x,1}$ | 0.20 | 0.4–0.7 | 7.5 |
| $P_2/P_1$ | 29 | 13–55 | $\approx 1$ |
| $T_2/T_1$ | 5.8 | 8–21 | 7.5 |
| $\rho_2/\rho_1$ | 5 | 1.7–2.6 | 0.13 |

[a] Properties based on air with $\gamma = 1.4$ and the upstream Mach number arbitrarily assumed to be 5.0.
[b] Estimates from laminar, adiabatic combustion of a stoichiometric methane–air mixture at 1 atm with an initial temperature of 298 K.

Table 1: Typical properties of normal shocks, detonations and deflagrations [1]

Another significant difference is that pressure remains nearly constant across a deflagration (with a slight decrease), whereas a defining characteristic of a detonation is the high pressure downstream of the propagating wave. The only common feature among detonations, deflagrations, and normal shock waves is the substantial increase in temperature across the wavefront.

Although real detonations exhibit a highly three-dimensional structure, valuable insights can be gained through a one-dimensional analysis. The first attempt to explain detonations, undertaken by Chapman in 1899, was based on a one-dimensional approach: an approach that remains useful today as the foundation for a more detailed understanding. The following assumptions are made, referencing the control volume depicted in Figure 1:

- one-dimensional, steady flow;
- constant area;
- ideal-gas behavior;
- constant and equal specific heats;
- negligible body forces;
- adiabatic conditions (no heat losses to the surroundings).

Given that the flow is steady and one-dimensional, the conservation laws can be directly applied to the finite control volume enclosed by the dashed lines in Figure 1. For steady flows, the mass flow rate $\dot{m}$ remains constant; moreover, if the area is fixed, the mass flux ($\dot{m}'' = \frac{\dot{m}}{A}$) is also a constant, leading to the mass conservation equation:

$$\dot{m}'' = \rho_1 v_{x,1} = \rho_2 v_{x,2} \tag{1}$$

Since no shear or body forces act on the control volume, pressure is the only force involved. The conservation of axial momentum is therefore expressed as:

$$P_1 + \rho_1 v_{x,1}^2 = P_2 + \rho_2 v_{x,2}^2 \tag{2}$$

Energy conservation is expressed as:

$$h_1 + \frac{v_{x,1}^2}{2} = h_2 + \frac{v_{x,2}^2}{2} \tag{3}$$

Relating enthalpy to the specific heat at constant pressure ($c_p$), which is assumed to be constant, and introducing the heat release $q$:

$$c_p T_1 + \frac{v_{x,1}^2}{2} + q = c_p T_2 + \frac{v_{x,2}^2}{2} \tag{4}$$

It is important to emphasize that the heat release $q$ is an intrinsic property of the mixture, with its magnitude depending on the specific fuel-oxidizer combination and the equivalence ratio. Additionally, applying the ideal gas law:

$$P_1 = \rho_1 R_1 T_1 \tag{5}$$

$$P_2 = \rho_2 R_2 T_2 \tag{6}$$

$$\gamma = \frac{c_p}{c_v} \tag{7}$$

$$c_p - c_v = R \tag{8}$$

where $R_1$ and $R_2$ are the specific gas constants; $\gamma$ is the ratio of specific heats and $c_v$ is the specific heat at constant volume. Simultaneous solution of the continuity and momentum conservation equations, Equations (1) and (2), leads to the following relationships:

$$\frac{P_2 - P_1}{\frac{1}{\rho_2} - \frac{1}{\rho_1}} = -\dot{m}''^2 \tag{9}$$

or, using the specific volume $v$:

$$\frac{P_2 - P_1}{v_2 - v_1} = -\dot{m}''^2 \tag{10}$$

The plot of $P$ versus $v$ for a fixed mass flux results in the Rayleigh line. By fixing $P_1$ and $v_1$, Equation (10) yields the following linear relationship :

$$P_2 = av_2 + b \quad \text{where} \quad a = -\dot{m}''^2 \quad \text{and} \quad b = P_1 + \dot{m}''^2 v_1 \tag{11}$$

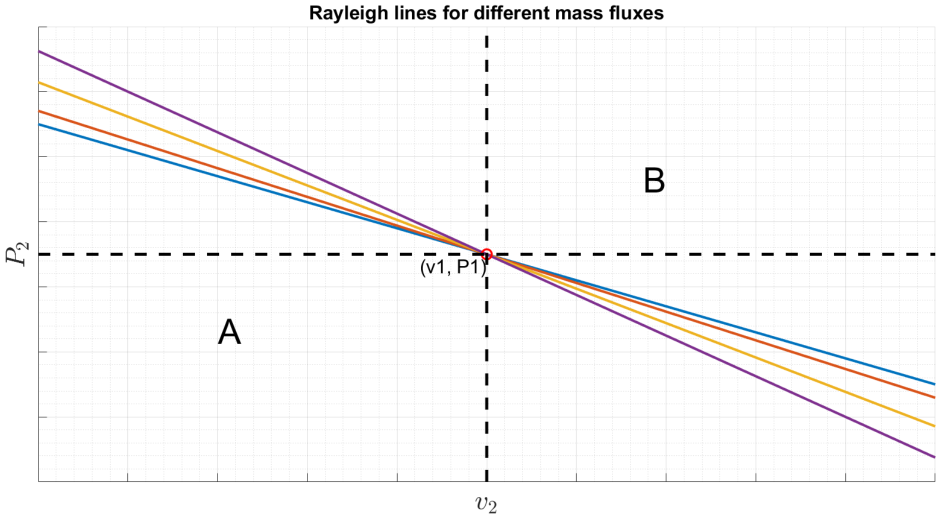

Figure 2: Rayleigh line for flow defined by mass flux, $P_1$ and $v_1$

Figure 2 illustrates the Rayleigh lines for an initial state ($P_1$, $v_1$) with increasing mass flux $\dot{m}''$, ranging from purple to light blue. As the mass flux increases, the lines become steeper, pivoting around the point ($P_1$, $v_1$). In the extreme case of infinite mass flux, the Rayleigh line becomes vertical; in the opposite limit of zero mass flux, it is horizontal. Since all possible mass flux values lie between these extremes, no solutions exist in the two quadrants (labelled A and B in Figure 2) defined by the dashed lines through ($P_1$, $v_1$): these regions are physically inaccessible. This fact will later help determine the possible final states of a detonation wave. The Rankine-Hugoniot curve is obtained by enforcing the energy equation (Equation (4)) in addition to the continuity and momentum conservation equations (Equations (1) and (2)), along with the ideal gas equations (Equations (5), (6), (7) and (8)):

$$\frac{\gamma}{\gamma-1}\left(\frac{P_2}{\rho_2} - \frac{P_1}{\rho_1}\right) - \frac{1}{2}(P_2 - P_1)\left(\frac{1}{\rho_1} + \frac{1}{\rho_2}\right) - q = 0 \tag{12}$$

or equivalently,

$$\frac{\gamma}{\gamma-1}(P_2 v_2 - P_1 v_1) - \frac{1}{2}(P_2 - P_1)(v_1 + v_2) - q = 0 \tag{13}$$

If $q$ is a known parameter and $P_1$, $v_1$ are fixed, as in the plot of Rayleigh line, Equation (13) defines a relation between $P_2$ and $v_2$, or, more generally, between $P$ and $v$, as:

$$f(P, v) = 0 \tag{14}$$

It is now possible to plot the pressure $P$ as a function of specific volume $v$ for given values $P_1$, $v_1$, and $q$, as shown in Figure 3.

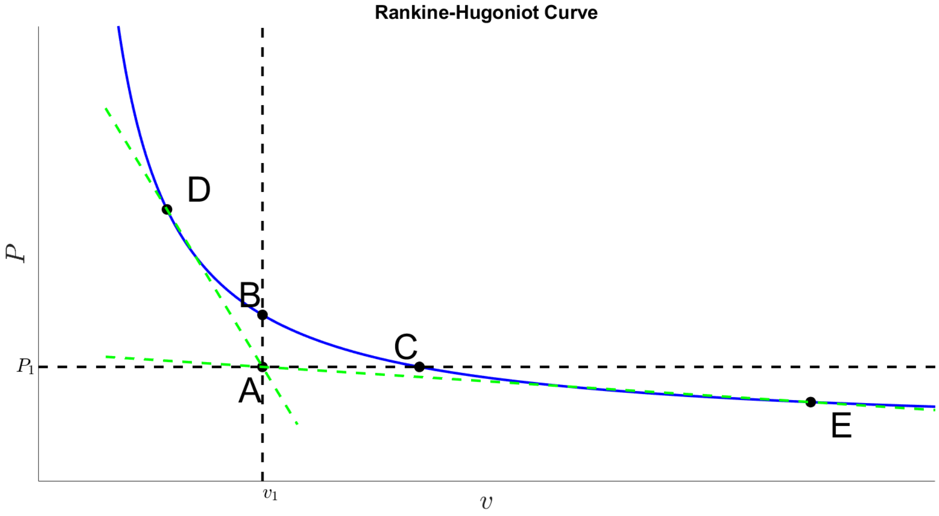

Figure 3: Rankine Hugoniot curve for q, $P_1$, $v_1$ fixed

In Figure 3, point A ($P_1$,$v_1$) is considered the origin since all Rayleigh lines pass through it. The upper branch of Hugoniot curve is defined as those points on the Hugoniot lying above point B, while the lower branch contains points below point C. The next step is to determine which points on the Hugoniot curve correspond to physically realizable states. Since any real process transitioning from state 1 to state 2 must satisfy both the Rayleigh relation (Equation (10)) and the Hugoniot relation (Equation (13)), points between B and C on the Hugoniot curve are unrealizable, as no valid Rayleigh line can be drawn between A and any point in this region (between B and C). In fact, between B and C no real solutions exist, as a positive-slope Rayleigh line is unphysical, as illustrated in Equation (9). Additionally, it can be noted that for the upper branch of the Hugoniot, there exists a limiting Rayleigh line tangent to the Hugoniot curve at point D. Point D corresponds to the scenario where $P_2$ is greater than $P_1$ and therefore is indicative of a detonation reaction. Conversely, point E is the case in which $P_2$ is less than $P_1$ and is therefore indicative of a deflagration reaction. These points of tangency are known as the Chapman-Jouguet points:

- the upper Chapman-Jouguet point corresponds to detonations, where the burned gas velocity, $v_{x,2}$, relative to the travelling detonation wave equals the local sonic speed;
- the lower Chapman-Jouguet point is similarly defined for deflagrations.

Above the upper Chapman-Jouguet point (D) are states associated with strong detonations. While mathematically valid, strong detonations are difficult to achieve due to their inherent instability. Between B and D lies the region of weak detonations, which require special conditions such as very rapid reaction rate to occur. Although real detonations are not one-dimensional, conditions at the upper Chapman-Jouguet point reasonably approximate those associated with actual detonations. The physical characteristics associated with each Hugoniot segment are summarized in Table 2.

| Region/segment of Hugoniot curve | Characteristics | Burned Gas Velocity $v_{x,2}$ |
|---|---|---|
| Above D | Strong detonation | Subsonic |
| D-B | Weak detonation | Supersonic |
| B-C | Inaccessible | - |
| C-E | Weak deflagration | Subsonic |
| Below E | Strong deflagration | Supersonic |

Table 2: Physical phenomena associated with various segments of the Hugoniot curve [1]

### 1.3 Efficiency Comparison

For traditional engines, thermal efficiency ($\eta_B$ ) is determined using the Brayton cycle, which depends on the temperatures ratio before ($T_0$) and after ($T_1$) the isentropic expansion (see Figure 4), as expressed in Equation (15):

$$\eta_B = 1 - \frac{T_0}{T_1} \tag{15}$$

On the other hand, detonation engines are modeled as Humphrey cycles in order to account for the nearly constant volume pressure increase during the cycle. The Humphrey cycle efficiency ($\eta_H$) depends not only on the temperature ratio before and after the isentropic expansion ($\frac{T_0}{T_1}$), but also on the ratio of temperatures before ($T_1$) and after ($T_2$) combustion, as shown in Equation (16):

$$\eta_H = 1 - \frac{T_0}{T_1}\gamma \left[ \frac{\left(\frac{T_2}{T_1}\right)^{\frac{1}{\gamma}} - 1}{\frac{T_2}{T_1} - 1} \right] \tag{16}$$

Thus, the difference between the Brayton and Humphrey cycle efficiencies is determined by the following $\frac{T_0}{T_1}$ multiplier:

$$\gamma \left[ \frac{\left(\frac{T_2}{T_1}\right)^{\frac{1}{\gamma}} - 1}{\frac{T_2}{T_1} - 1} \right] \tag{17}$$

For detonation combustion, this term is always less than one. As a result, the efficiency of a Humphrey (detonation) cycle is greater than the efficiency of the Brayton (deflagration) cycle.

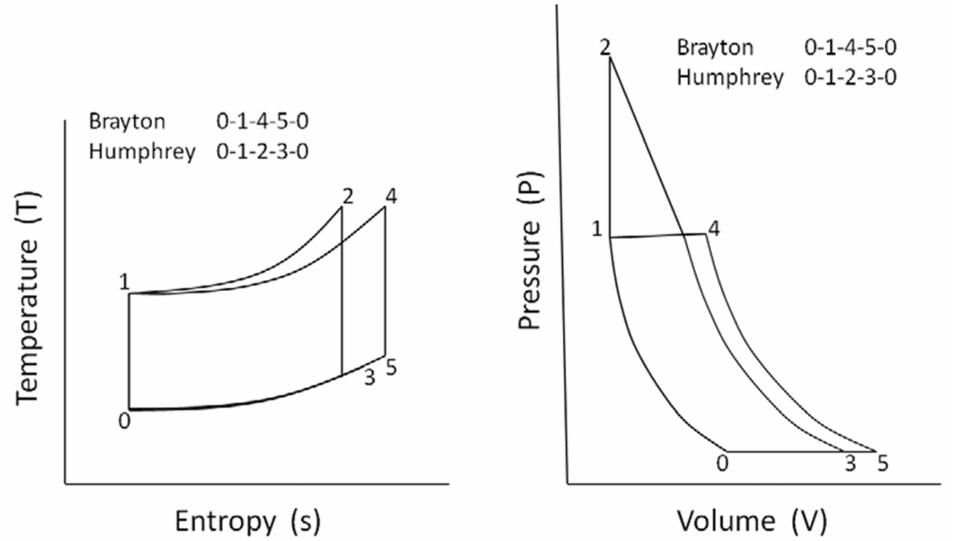

Figure 4: Temperature-entropy and pressure-volume diagrams of Brayton and Humphrey cycles [2]

As shown in Figure 4 and as already stated, detonation has the minimum entropy generation among combustion modes, providing a potential thermodynamic advantage. Additionally, the total area under the Humphrey $P - v$ curve is greater than that under the Brayton $P - v$ curve, indicating greater availability of useful work from the Humphrey cycle.

The Brayton cycle consists of two constant pressures and two isentropic processes. It represents the constant pressure heat addition of deflagration combustion. On the other hand, the Humphrey cycle consists of four processes, considering Figure 4:

1. isentropic compression (0-1): occurs ahead of the detonation wave in PDEs;
2. constant-volume combustion (1-2): a rapid pressure increase due to detonation;
3. isentropic expansion (2-3): the combustion products expand back to atmospheric pressure, primarily driven by rarefaction waves in PDEs;
4. isobaric process (3-0): completes the cycle, returning to the initial state.

## 1.4 PDE Cycle Operation

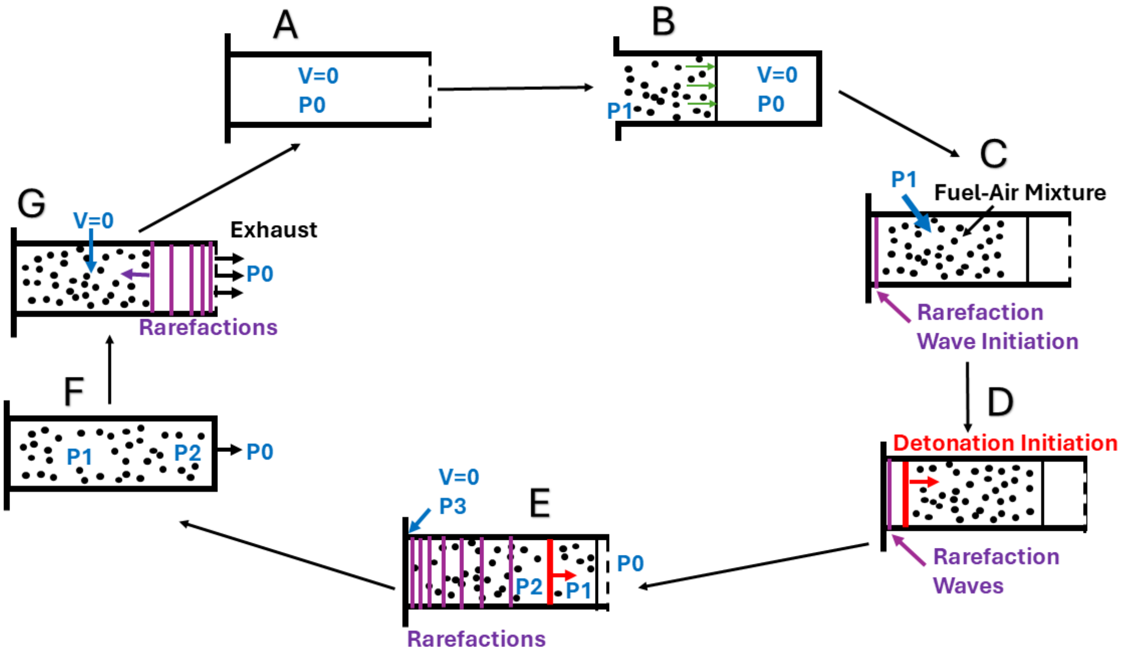

,

Figure 5: PDE cycle operations [2]

Figure 5 illustrates the sequence of events in a single detonation cycle within a tube with one closed and one open end.

The detonation initiates near the closed end, beginning with an empty chamber (Figure 5 A). Moving clockwise, a fuel-air or fuel-oxidizer mixture is injected at the closed (valved) end at pressure $P_1$ and temperature $T_1$ (Figure 5 B), determined by flight conditions and inlet design. Once the chamber is fully loaded, the valves close (Figure 5 C), ensuring that the propellant mixture and the detonation wave reach the combustor exit simultaneously to prevent any unburned gases from escaping and lowering the operational efficiency. An ignition source then initiates combustion, transitioning from deflagration to detonation (Figure 5 D). An expansion zone is created between the closed end of the chamber and the detonation wave since the velocity must be zero at the closed end.

Rarefaction waves are generated at the closed end of the chamber and proceed towards the open end of the chamber, to satisfy the constraint of zero axial fluid velocity normal to the wall. The strength of the expansion region is influenced by $\gamma$, the ratio of specific heats of the burnt gases, which affects the axial velocity of the gases behind the detonation wave. These burnt gases must be decelerated to satisfy the closed end boundary condition.

Once the detonation is initiated, the detonation wave propagates towards the open end of the chamber (Figure 5 E). Ideally, the detonation propagates at the Chapman-Jouguet velocity, creating high-temperature, high-pressure combustion products behind the wave; while expansion near the closed end lowers temperature and pressure.

As the detonation exits, the chamber contains combustion products at varying pressures and temperatures (Figure 5 F): conditions along the chamber vary from T3 and P3 at the closed end to P2 and T2 at the open end. The axial velocity of the combustion products ranges from zero at the closed end to supersonic values outside the chamber exit. A pressure differential at the open end generates rarefaction waves that propagate back into the chamber,

expelling the combustion gases. These waves propagate at the speed of sound of the combustion products, accelerating the burned gas toward the open end.
After the primary combustion products are expelled from the chamber, the remaining gas within the chamber is at a pressure near $P_3$. (Figure 5 G). The chamber undergoes an unsteady blowdown process, characterized by alternating compression and rarefaction waves that further expel gases until pressure and temperature decay to ambient levels. Once conditions are suitable, a fresh fuel-air or fuel-oxidizer mixture is introduced, and the cycle restarts. To prevent premature ignition, an active purge removes residual combustion products before refilling the chamber.

## 1.5 Structure of the shock

The objective of this discussion is to highlight the key gas dynamic interactions and processes that govern impulse generation in a PDE, analysing in details the situation depicted in Figure 5 D.

A PDE thrust tube with a uniform, constant diameter and an overall length L is considered, which is initially filled entirely with a gaseous detonable propellant, as illustrated in Figure 6. The detonable propellant is separated from the ambient environment by an idealized contact surface located at the chamber exit plane. For simplicity, it is assumed that both the detonable propellant and the contact surface are initially at rest. Upon ignition, a detonation wave is assumed to be instantaneously initiated at the head end of the thrust chamber, propagating towards the chamber exit. This detonation wave is immediately followed by a self-similar rarefaction wave, also referred to as the Taylor wave, as visible in Figure 6. The rarefaction wave decelerates the gas from a high velocity to a stationary state, ensuring compliance with the closed-wall boundary condition at the head end of the chamber.

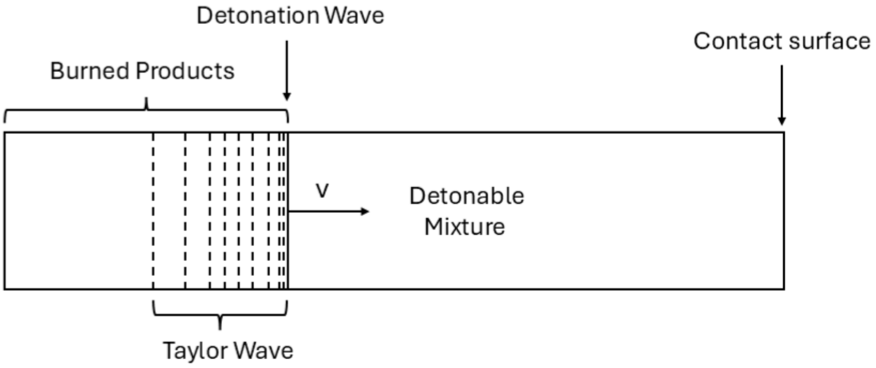

Figure 6: Schematic of the starting flow field following detonation initiation in a fully filled PDE [3]

As the detonation wave reaches the contact surface, it generates an unsteady shock wave that propagates into the surrounding ambient gas. Concurrently, a reflected wave travels upstream into the burned detonation products toward the head end of the chamber. The strength of the transmitted shock wave is determined by the change in acoustic impedance across the contact surface. Meanwhile, the reflected wave may manifest as a reflected shock, a Mach wave, or a rarefaction wave. Following the reflected interface wave, an exhausting rarefaction wave propagates toward the thrust wall at the head end of the chamber. This wave serves as the primary mechanism driving the gasdynamic blowdown of the thrust chamber to ambient conditions. Consequently, the exhausting rarefaction wave accelerates

the high-pressure burned products out of the chamber.
Similarly, once the exhausting rarefaction wave reaches the head end of the chamber and reflects, the pressure on the thrust wall gradually decreases toward ambient conditions. The interaction between the detonation wave, Taylor wave, reflected interface wave and exhausting rarefaction wave constitute the fundamental gasdynamic processes in such a system and must be accurately modelled to analyse the single-cycle performance of a fully filled PDE.

## 1.6 Propellant comparisons

Fuel selection is driven by specific mission applications. High-speed aircraft applications may favor hydrogen fuel, whereas volume and weight limitations of missile systems may favor higher density liquid fuels and of microsatellites, which are likely to employ ethylene/oxygen mixtures. The selection of the propellant is a critical factor in the development of the experimental test rig, as it directly influences various aspects, including the system's size, component selection, operating conditions (such as pressure, temperature and detonation parameters), oxidizer-to-fuel ratio, as well as associated risks and safety considerations.

### 1.6.1 Hydrogen

Hydrogen has been extensively studied in PDEs, particularly in numerical simulations due to its relatively simple chemical kinetics and ease of detonation.
It's a carbon free fuel suitable for both air-breathing and space-based propulsion systems.
Light fuels like hydrogen require less initial pressure and temperature to detonate. It is characterized by high reactivity, low molecular weight and high specific heat, making it a preferred choice for applications requiring high PDE performance.
Hydrogen-air mixtures demonstrate superior detonation properties, achieving the highest detonation velocity and specific impulse. In fact, the combustion products containing simple light molecules tend to generate higher values of detonation velocity and detonate easily.
Hydrogen has a high specific energy content, which translates to a greater amount of energy released per unit mass. This leads to increased thrust and specific impulse values compared to traditional hydrocarbon fuels.
Hydrogen combustion primarily produces water vapor rather than harmful emissions such as carbon dioxide or soot, which are common in traditional fuels. This not only contributes to cleaner combustion but also improves overall system efficiency and reduces environmental impacts. Therefore, hydrogen applications are suitable for sustainability and drop of emissions. The combustion of hydrogen generates high temperatures quickly, which can enhance the performance of the combustor. The resulting hot gases expand rapidly, driving the detonation wave more effectively than in traditional fuel scenarios due to this rapid heat release.

Hydrogen detonation dynamics are highly dependent on the oxidizer. For $H_2/O_2$ mixtures, the detonation cell size is much smaller than for $H_2$/air, leading to a faster deflagration-to-detonation transition (DDT). However, nitrogen in air acts as a heat sink, slowing down combustion compared to pure oxygen. This distinction is crucial for optimizing PDE design and performance.
Also, the $H_2/O_2$ mixture is more sensitive to detonation than the latter because $N_2$ requires a higher temperature to dissociate than for $H_2$/air for the same gas feed pressure. This translates into a faster DDT for $H_2/O_2$ mixture but also a less safe procedure.
If, after constructing the facility, the oxidizer is switched, the change in oxidizer—while

maintaining the same combustor configuration— results in suboptimal oxidizer injection. Consequently, mixing becomes the primary factor contributing to degraded performance in oxygen operation, leading to an increased number of misfires and, ultimately, a reduction in specific impulse under off-design conditions.

Unfortunately, hydrogen combustion requires proper ventilation, leak detection sensors, and safety measures due to its high flammability. Special flame detectors and flame arrestors are commonly used to enhance safety.

### 1.6.2 Hydrocarbons

Hydrocarbon fuels, both gaseous and liquid, have been widely utilized in PDE research. Common gaseous fuels include ethylene ($C_2H_4$) and propane ($C_3H_8$), while liquid fuels include JP-10 ($C_{10}H_{16}$) and kerosene.

In general, they are less explosive than hydrogen but the emission associated to their detonation can be a problem. Moreover, for complex hydrocarbons DDT process is more difficult to achieve in a small volume than with hydrogen. Hence, miniaturization can be an issue.

CFD analysis revealed that detonation wave travel time varies across fuels. Hydrogen reaches the end of the detonation tube fastest, followed by methane and kerosene, correlating with each fuel's heat release rate. In general, fuels having a higher heat release rate consume less time, as the hydrogen. As the number of carbon atoms increases, chemical reaction time also increases as the detonation wave propagates from the closed end towards the open end. The increasing time of the cycle limits the operational frequency of PDE, limiting, consequently, the performances.

Ethylene has been particularly favored in PDE studies due to its well-documented detonation properties, with numerical simulations and experimental data showing strong agreement.

Studies have shown that heating liquid kerosene enhances engine performance and aids the deflagration-to-detonation transition. However, heavy hydrocarbons such as kerosene exhibit lower detonation sensitivity, requiring higher activation energy and longer chemical reaction times with respect to hydrogen. For instance, kerosene-air mixtures have the lowest detonation velocity of 1520 m/s and the lowest specific impulse, as illustrated in Figure 7.

Liquid gasoline has also been explored as a PDE fuel. When vaporized, it absorbs heat from combustion products, acting as a buffer zone, preventing pre-ignition by isolating the fresh fuel-oxidizer mixture from the hot combustion products. This configuration has several advantages, such as reducing the hardware complexity and not having litimitations on the operational frequency.
An additional advantage of employing gasoline is that no forced cooling is required because vaporization of the liquid fuel, after being injected into the tube, would consume a lot of heat that inevitably resulted in a temperature drop of the combustion products. However, it is necessary to include a nitrogen tank to expel gasoline under pressure. Additionally, as with all hydrocarbons, emissions present a critical concern.

Among alternative hydrocarbons, biogas and natural gas have been considered due to their lower gas emissions and cost-effectiveness, though research on their use in PDEs remains extremely limited. Based on the limited experiments conducted, it was concluded that the combustion velocity of biogas is slower compared to propane. Experimental results also indicate that biogas detonates at a lower velocity and with a larger cell width than propane ($C_3H_8$). Consequently, achieving detonation with biogas is more challenging. Theoretically, the use of pure biogas in a PDE may not lead to detonation due to the presence of $CO_2$, which acts as a powerful anti-knock agent. Therefore, a more reactive gas should be introduced as an additive to enhance the mixture. In fact, a higher methane concentration enhances detonation pressure, Mach number and temperature. Increasing the hydrogen content in biogas improves its detonation properties, while it is inversely proportional to the cell width size: a larger cell implies that detonations are less easily instigated.

## 1.7 Other solutions

In pursuit of sustainable propulsion, ammonia has been investigated as a potential PDE fuel due to its lower carbon footprint. However, ammonia suffers from low flame propagation velocity and a slow heat release rate, which hinder its large-scale adoption. Compared to traditional combustion, detonation offers higher thermodynamic efficiency, potentially compensating for ammonia's poor combustion characteristics. One approach for improving ammonia detonation performance is blending it with hydrogen or oxygen, significantly enhancing ignition and stable propagation of the detonation wave. However, despite the additional measures, achieving detonation with ammonia has proven difficult to date. Furthermore, the successful attempts necessitate a long cycle time, which consequently results in reduced performance.

Another innovative approach involves blended fuels. Studies have demonstrated that hydrogen-methane, hydrogen-kerosene and methane-kerosene blends can be effective PDE fuels, mitigating the challenges associated with pure hydrogen. For example, a 50% hydrogen-kerosene blend achieves a detonation velocity of 1822.83 m/s, nearly matching pure hydrogen (see Section 1.9). Such blends offer a promising balance between efficiency, emissions reduction and practicality. Unfortunately, almost no studies or experiments have been carried out. Blended fuels, while not dramatically altering thrust performance with respect to hydrocarbons, provide viable alternatives to mitigate hydrogen's drawbacks in PDE applications.

## 1.8 Specific impulse comparison

To compare the various fuels, a set of numerical data has been gathered. A key parameter for this comparison, regardless of whether the oxidizer is air or oxygen, is the fuel-based specific impulse, which solely considers the mass flow rate of the fuel. Consequently, the fuel-based specific impulse is always higher than the general specific impulse. The general specific impulse is strongly influenced by the configuration of the detonation engine; therefore, only the fuel-based specific impulse is considered for an accurate comparison.

This serves as an ideal representation of the performance of the different fuels. A realistic PDE cycle, however, includes losses due to fill, detonation, blowdown and purge processes, which are not accounted for in this analysis.

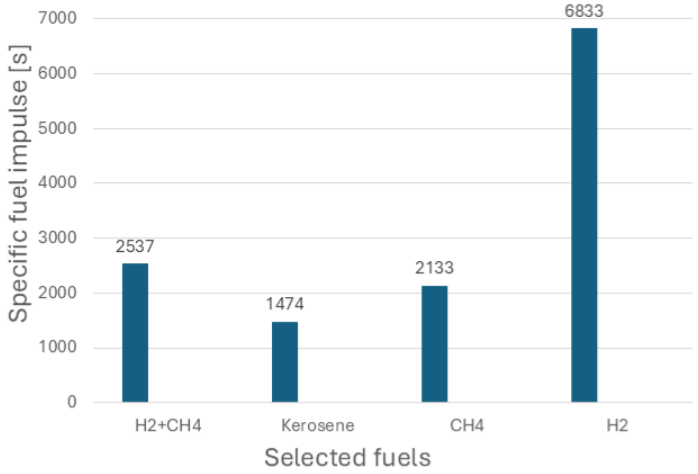

Figure 7: Fuel based specific impulse of PDE operating on different fuels [4]

## 1.9 CEA comparison

The following section presents the computation of detonation performance using the NASA CEA (Chemical Equilibrium with Applications) code. Based on previous studies, the computed results show excellent agreement with experimental data. The evaluation of detonation performance parameters with the CEA code is based on Chapman-Jouguet theory, as outlined in Section 1.2. This theory assumes ideal mixing and complete, instantaneous reaction to equilibrium. The equations implemented in the CEA code are derived from the conservation principles presented in Section 1.2, assuming a constant-area flow hypothesis. The computational procedure involves iteratively solving these equations using the Newton-Raphson method.

Detonation properties are highly dependent on initial conditions. For consistency, the initial conditions are kept the same across all propellant combinations, as follows:

- temperature: $T = 300$ K;
- pressure: $P = 1$ atm;
- stoichiometric mixture considered.

While the same initial conditions are applied for all fuels in this preliminary comparison, an actual analysis would require different initial values of pressure and temperature depending on the specific fuel type. The uniformity in initial conditions is adopted here for simplicity and to facilitate comparative analysis.

Detonation velocity, $v_{detonation}$, is a key parameter in evaluating engine performance, as a higher detonation velocity results in a greater exhaust velocity and, consequently, higher thrust. Moreover, through CEA analysis, the detonation pressure of the mixture is evaluated: this is vital to determine the thickness of the detonation tube, which will be useful for the development of the experimental rig.

### 1.9.1 $H_2$/Air Mixture

| Property | Value |
|---|---|
| $v_{detonation}[m/s]$ | 1964.9 |
| $P_2/P_1$ | 15.5 |
| $T_2/T_1$ | 9.8 |
| $\rho_2/\rho_1$ | 1.8 |

Table 3: CEA results for $H_2$/air mixture at 1 atm and 300 K

The results in Table 3 align perfectly with the properties outlined in Table 1.

### 1.9.2 $H_2$/$O_2$ Mixture

| Property | Value |
|---|---|
| $v_{detonation}[m/s]$ | 2835.7 |
| $P_2/P_1$ | 18.7 |
| $T_2/T_1$ | 12.3 |
| $\rho_2/\rho_1$ | 1.8 |

Table 4: CEA results for $H_2/O_2$ mixture at 1 atm and 300 K

As expected, the detonation velocity increases when pure oxygen is used as the oxidizer instead of air.

### 1.9.3 $CH_4$/Air Mixture

| Property | Value |
|---|---|
| $v_{detonation}[m/s]$ | 1799.9 |
| $P_2/P_1$ | 17.1 |
| $T_2/T_1$ | 9.3 |
| $\rho_2/\rho_1$ | 1.8 |

Table 5: CEA results for $CH_4$/air mixture at 1 atm and 300 K

### 1.9.4 $C_2H_4$/Air Mixture

| Property | Value |
|---|---|
| $v_{detonation}[m/s]$ | 1820.9 |
| $P_2/P_1$ | 18.2 |
| $T_2/T_1$ | 9.8 |
| $\rho_2/\rho_1$ | 1.8 |

Table 6: CEA results for $C_2H_4$/air mixture at 1 atm and 300 K

As expected, hydrocarbon/air mixtures exhibit lower detonation velocities compared to hydrogen/air mixtures.

### 1.9.5 $C_3H_8$/Air Mixture

| Property | Value |
|---|---|
| $v_{detonation}[m/s]$ | 1796.6 |
| $P_2/P_1$ | 18.1 |
| $T_2/T_1$ | 9.4 |
| $\rho_2/\rho_1$ | 1.8 |

Table 7: CEA results for $C_3H_8$/air mixture at 1 atm and 300 K

As anticipated, heavier hydrocarbons are less prone to detonation. In fact, for instance, as mentioned in Section 1.6.2, kerosene is associated with the lowest detonation velocity of 1520 m/s.

### 1.9.6 $CH_4+H_2$/Air Mixture

| Property | Value |
|---|---|
| $v_{detonation}[m/s]$ | 1909.8 |
| $P_2/P_1$ | 15.9 |
| $T_2/T_1$ | 9.6 |
| $\rho_2/\rho_1$ | 1.8 |

Table 8: CEA results for $CH_4+H_2$/air mixture at 1 atm and 300 K

As expected, the blended $CH_4/H_2$ mixture exhibits a higher detonation velocity compared to pure methane (Section 1.9.3), as the presence of hydrogen enhances the combustion characteristics and improves performance. This is the most performing blended mixture: for instance, as already mentioned in Section 1.7, a 50% hydrogen-kerosene blend achieves a detonation velocity of 1822.83 m/s.

## 1.10 PDE and RDE comparison

Until now, the focus was on PDEs; however, another category of detonation engines, namely Rotating Detonation Engines (RDEs), warrants attention. The operating principle of RDEs is based on the same fundamental theory described earlier, and the fuel comparison remains valid for both types of engines.

The key distinction lies in the fact that thrust in RDEs is continuous. Unlike a PDE, which operates intermittently, an RDE generates thrust by exploiting one or more detonation waves that continuously circulate around its annular chamber. This operational difference influences the experimental setup, such as annular combustion chamber for RDEs rather than a straight hollow tube for PDEs, and the working mechanism of the engine.

In a PDE, thrust output is intermittent: the peak thrust is high, but the average thrust can be low due to the periodic operation. Since thrust is generated with each detonation cycle,

increasing the pulsing frequency could help to generate more thrust, but this is constrained by the time required to refill the detonation tube with fresh mixture. Reducing the size of the detonation tube could potentially be advantageous, as it would reduce the time needed for charging the mixture. However, this comes with complications such as issues with valving, mixing, shortened residence time and increased heat loads.
The PDE cycle is inherently unsteady when compared to the deflagration cycle. In contrast, when a detonation wave rotates along the circumference of the annular combustor channel, as in RDEs, continuous detonation is achieved, which enhances propulsion performance.
However, rotating detonation waves (RDWs) lead to an uneven flow field, high local temperatures and high pressures potentially damaging the combustor.

The advantage of RDE is that it only requires one initiation during each run, after which detonation waves continue to rotate within the combustion chamber. There may be multiple RDWs present within the combustor. A detonation wave is formed in the predetonator, which is tangentially connected to the combustor, and injected into the combustor to detonate reactants, thereby forming an RDW, as depicted in Figure 8.

A notable advantage of RDEs is their ability to operate efficiently when coupled with an aerospike nozzle. However, RDEs present several challenges when compared to conventional deflagration engines, including high temperatures and pressures near the RDWs, combustion instability, uneven and unsteady flow fields, and increased mechanical and thermal loads, all of which can damage the engine. These challenges also make it difficult to integrate the combustor with the nozzle.

The flow field within the RDE is quite complex. However, it closely follows the “steady-state” detonation cycle, in contrast to the PDE. One configuration that enables continuous detonation is the annular arrangement surrounding a cylindrical core, as illustrated in Figure 8. In this configuration, the combustion or detonation chamber is an annular ring, where a premixed fuel-air mixture is injected axially at the bottom of the combustion chamber. Once initiated, the detonation wave propagates circumferentially around the annular ring near the injection plane. The detonated products are expanded and exhausted out of the top-end of the combustion chamber, which may also accommodate a nozzle to further harness the energy of the exhaust products.
Unlike the PDE, the RDE provides a nearly steady source of thrust without the need for repeated detonations at very high frequencies, as previously mentioned. However, since the detonable mixture is injected axially and the detonation wave propagates circumferentially around the combustion chamber, as displayed in Figure 8, the flow field within the RDE exhibits strong axial and azimuthal components, which complicate the analysis and may hinder efficient engine design. Additionally, because a detonation wave is continuously present in the combustion chamber, managing heat transfer to the walls and controlling the temperature within the chamber become significant challenges.

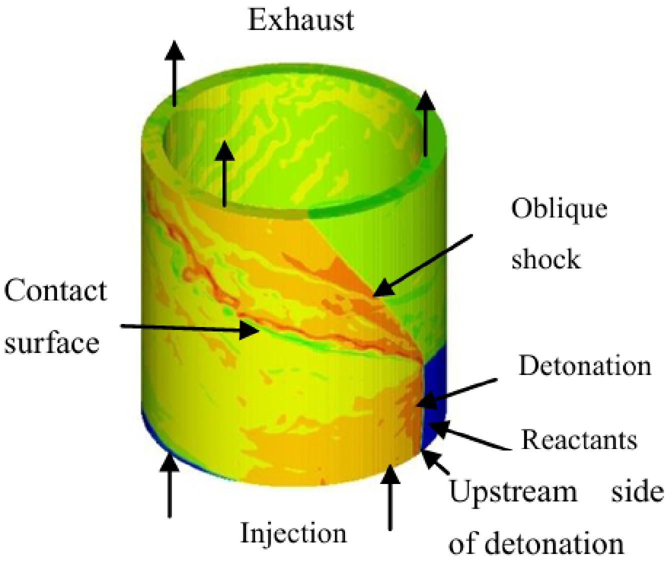

Figure 8: Operating principle of an RDE [5]

RDEs, as PDEs, represent potential replacements for conventional engines, including turbojet, ramjet and liquid rocket engines. In fact, RDEs offer key advantages over conventional engine types:

- for turbojets, RDEs improve performance and simplify the system by reducing the compression stage;
- for ramjets, RDEs offer enhanced performance with a shorter ram combustor and operation at lower Mach numbers. Based on the ideal detonation cycle performance estimate under steady-state operation, the specific impulse for an RDE could reach more than 6000 s, compared to approximately 4000 s for a ramjet at Mach 2.1;
- for liquid rocket engines, RDEs provide improved performance, compactness, lower feeding pressure and thrust vectoring capabilities.

RDEs are expected to deliver higher thrust densities than PDEs due to continuous combustion, making them an attractive option for aerospace applications such as rocket and airplane propulsion, as well as gas turbine engines for power generation. Detonation combustion in an RDE occurs over a significantly shorter distance than PDEs: thus, the design results more compact. The minimum cycle frequency to ensure performance of PDEs above classical combustion (deflagration) is 75 Hz, and the state-of-the-art devices range between 100 and 400 Hz. On the other hand, the RDE provides a steady thrust source and can scale up to larger thrust sizes more easily, making it a promising alternative to PDEs.
However, the conditions within the RDE combustion chamber are less understood compared to PDEs, making the design of a combustion chamber capable of withstanding the forces and heat fluxes typical in an RDE more challenging.
Additionally, in the past experiments a situation in which there were two counter-rotating detonation waves occurred. As they collide with each other, they cause detonation failure. Counter-rotating detonation waves are related to the insufficient mixing of fuels and oxidants: hence, this aspect must be carefully analysed. In general, predicting and developing a model for RDEs is more complex compared to PDEs due to these unexplored phenomena. Consequently, simulating such behavior and achieving consistency with experimental

data is extremely challenging. Hence, experimental studies are carried on with lack of a solid theoretical foundation. Therefore, compared to PDEs, a more extensive and cumbersome experimental campaign is necessary, involving the deployment of additional sensors, higher temporal discretization and a high likelihood of failures.
Regarding performance, it is currently estimated that the RDE could outperform the PDE by approximately 33%.
However, one of the most important factors in choosing between PDEs and RDEs is the specific mission requirements. PDEs offer a rapid thrust response to commands, generate highly precise impulses, and can throttle thrust by adjusting the operating frequency. Given these characteristics, RDEs are expected to serve as the primary thrusters for orbital maneuvering systems (OMSs) in spacecraft and rockets, whereas PDEs are well-suited for reaction control systems (RCSs), where high-precision orbit and attitude control are required.

## 1.11 State of the art

Below is a non-exhaustive list of key research institutions and competitors including PDEs and RDEs.

### 1.11.1 Pulse Detonation Engines (PDEs)

- **Romanian National Research and Development Institute for Gas Turbines (COMOTI)**
  *Design:* PDE
  *Propellant:* Hydrogen-air

- **Northwestern Polytechnical University, China & Science and Technology on Space Physics Laboratory, Beijing, China**
  *Design:* Valveless PDE
  *Innovation:* Traditional PDEs use mechanical valves for periodic fuel supply control, increasing hardware complexity and limiting operating frequency. The valveless design achieves inlet-combustor isolation via gas dynamics rather than mechanical valves. Hence, the design is simpler and avoids the disadvantage associated with airflow stagnation in the valved design.
  *Propellant:* Liquid gasoline and oxygen-enriched air

- **Vasad, India (Subhash Chander and Tejinder Jindal)**
  *Design:* Valveless PDE
  *Propellant:* Oxygen and acetylene

- **Moscow Lomonosov University & Kurchatov Institute, Russia**
  *Design:* PDE
  *Propellant:* Acetylene and oxygen

- **NASA Glenn Research Center, USA**
  *Design:* PDE
  *Propellant:* Ethylene and air; experiments also with propane, kerosene and JP-10 with air

- **Air Force Research Laboratory (AFRL), USA**
  *Design:* PDE
  *Propellant:* Hydrogen-air

- **School of Mechanical Engineering, Nanjing University of Science and Technology,**

**China**
*Design:* PDE
*Propellant:* Octane ($C_8H_{18}$) and air

- **Pennsylvania State University, USA**
  *Design:* Valveless PDE
  *Propellant:* Hydrogen-air

### 1.11.2 Rotating Detonation Engines (RDEs)

- **Research Center of Combustion Aerodynamics, Southwest University of Science and Technology, China & College of Engineering, Peking University, China**
  *Design:* RDE
  *Propellant:* Hydrogen and oxygen
- **U.S. Air Force Research Laboratory (AFRL), Wright–Patterson Air Force Base & Innovative Scientific Solutions, Inc., USA**
  *Design:* RDE
  *Propellant:* Hydrogen and air
- **Nagoya University, JAXA, and Muroran Institute of Technology, Japan**
  *Design:* RDE
  *Propellant:* Ethylene and oxygen
- **Beijing University of Chemical Technology & China Aerodynamics Research and Development Center, China**
  *Design:* RDE
  *Propellant:* Hydrogen-air and ethylene-air

# Chapter 2

## 2 Experimental Setup

### 2.1 Selection of the configuration

Based on the comparison presented in Section 1.6, hydrogen/air is selected as the optimal propellant combination due to several advantages highlighted in Section 1.6.1, including its environmental benefits, ease of detonation and superior propulsive performance. Additionally, current research trends favour the use of $H_2$, making it a highly reasonable choice to initiate research with this fuel. Air is chosen as the oxidizer instead of pure oxygen for safety reasons.

Regarding the choice between PDE and RDE, PDE is initially considered for simplicity, while keeping in mind the potential for transitioning to an RDE configuration. Thus, transitioning from a PDE to an RDE would be straightforward and cost-effective. As discussed in Section 1.10, designing an RDE is more challenging than a PDE due to the complex forces, heat fluxes, flow fields, and conditions that are not well understood and are often unpredictable. In the following analysis, the PDE configuration is considered, but the design incorporates features that facilitate a future transition to an RDE, ensuring that the change is as seamless and economical as possible. For instance, the selection of pressure transducers for PDEs would lean towards piezoelectric sensors; however, to accommodate a potential shift to RDE, piezoresistive transducers are also considered so as they can be easily integrated into the experimental setup without significant costs or major modifications.

### 2.2 Comparison of Valved and Valveless Designs

Apart from the choice of fuel and the selection between a PDE or RDE, another critical design decision must be made: whether to adopt a valved or valveless configuration.

As discussed in Section 1.11.1, the valved design utilizes mechanical valves to regulate the periodic supply of fuel. While this approach allows for precise control, it increases hardware complexity and limits the operating frequency. In fact, the maximum operating frequency of a PDE is significantly constrained by the performance of its valves, such as solenoid valves. Although high-speed solenoid valves can achieve frequencies exceeding 100 Hz, their flow rates remain insufficient for practical PDE applications. In contrast, the valveless design relies on gas dynamics rather than mechanical components to achieve inlet-combustor isolation. This simplifies the system and eliminates airflow stagnation issues inherent in valved configurations. On the other hand, mechanical valves are exposed to extremely high operating temperatures, which can significantly reduce their lifespan.

In a valveless configuration, no mechanical valves are used to regulate the supply of propellants. Instead, the periodic fuel intake is governed by pressure oscillations within the detonation tube. Since detonation is a pressure gain process, it generates gas-dynamic valves near the inlet, effectively interrupting the propellant flow. The oscillation frequency of these pressure waves can be significantly higher than that of mechanical valves. However, valveless PDE systems have a higher likelihood of failure and are primarily employed in airbreathing PDEs rather than in space applications,

where they are unsuitable. Moreover, for airbreathing applications, liquid hydrocarbon fuels are generally preferred for the valveless configuration, which is not relevant in the present case. The use of a valveless configuration may lead to unpredictable operating conditions and pose risks to system stability. Furthermore, the inability to control pressure waves due to the lack of valves results in complex wave interactions within the system. Because these waves can travel bidirectionally without redirection or containment, predicting their behaviour becomes challenging. Timing discrepancies in wave arrivals may lead to constructive and destructive interference, causing substantial variations in peak pressures. This unpredictability complicates both engine design and operational stability.
Modelling and simulating a valveless PDE system is considerably more complex, as it requires accounting for multiple interacting waves, thereby increasing both the design complexity and the time needed for optimization. While valveless systems may offer cost advantages by eliminating the need for expensive valves, the extensive computational and experimental efforts required for their optimization can offset these savings.

The use of mechanical valves can enhance the pressure gain, a critical factor influencing overall engine performance, thrust, and efficiency. Mechanical valves create a controlled and stable pressure environment within the combustion chamber, contributing to higher pressure gain. Conversely, when an aerodynamic orifice valve (valveless configuration) is used, studies indicate that the combustor is more likely to fail in achieving pressure gain due to total pressure losses and ineffective filling processes.

In conclusion, while valved PDEs offer advantages in terms of control, performance and pressure gain, valveless PDEs may still provide benefits in terms of mechanical simplicity and potentially lower maintenance requirements. However, achieving high performance levels may require significant design optimizations to mitigate fluid dynamic losses and pressure inefficiencies.
Aside from the various disadvantages of the valveless configuration, the valved design is chosen also because the valveless configuration is not suitable for gaseous fuels such as hydrogen.

## 2.3 Preliminary List of Components

Based on the literature and the analysis of the physical processes, a list of components has been compiled and is presented below, based on the valve configuration, as selected in Section 2.2. Initially, a brief overview of the components, organized by functionality, is provided, followed by a detailed description of each component.

- Structural components: stainless steel tube and support bars;
- Instrumentation: dynamic pressure transducers, thermocouples, ion probes, mass flow meters, load cell, accelerometers and high speed camera;
- Fuel/oxidizer system: supply lines, tanks, injectors, rotary valve, one way valves, flame arrestors and critical flow nozzles;
- Ignition and control: spark plug and emergency shutoff button;
- Detonation enhancement: Shchelkin spiral;
- Data acquisition system (DAQ);
- Cooling system;

- Purge system.

## 2.4 Selection of material

The selection of materials for components, such as the detonation tube and the spiral, is primarily driven by the harsh conditions inside the PDE. Stainless steel is chosen for the following reasons:

- corrosion resistance: a key consideration in a PDE is the presence of reactive gases, such as hydrogen and oxygen, which can lead to corrosion. Stainless steel is highly resistant to corrosion, particularly in aggressive environments, making it ideal for handling reactive gases and preventing material degradation over time;
- high-temperature resistance and thermal stability: stainless steel exhibits excellent resistance to high temperatures and thermal stability, allowing it to withstand the heat generated by detonations without losing structural integrity;
- fatigue resistance: during detonation, the tube experiences dynamic and cyclic loads. Stainless steel is known for its ability to withstand repeated loading cycles without failure, making it critical for components exposed to high-pressure and high-temperature cyclic conditions like those in a PDE;
- resistance to plastic deformation: the material must be hard and resistant to plastic deformation due to the high-pressure shock waves generated during detonation. Stainless steel provides adequate resistance to plastic deformation, maintaining the integrity of the detonation tube and preventing structural failure under pressure;
- workability and availability: stainless steel is relatively easy to machine, weld, and form, making it suitable for the design of structures like those found in a PDE. Additionally, it is widely available and cost-effective, reducing material and manufacturing costs;
- thermal conductivity: although stainless steel does not have the best thermal conductivity compared to metals like copper, it still offers adequate thermal conductivity, enabling efficient heat dissipation during the detonation cycles.

## 2.5 Detailed Description of Components

Now that the configuration type has been selected, the list of components referenced in Section 2.3 is detailed. This includes the type of instrument, key features, as well as its connections and the rationale for selecting each component in relation to the physical process. The total cost is evaluated subsequently, as it depends on the size of the facility. For this purpose, three different sizes of the experimental setup are considered, and a corresponding plot is generated in Section 2.8.

### 2.5.1 Structural components

The PDE consists of a stainless steel tube, closed at the left end and open to the ambient atmosphere at the right end. The tube is mounted at two points onto a sliding mechanism, allowing longitudinal movement along a stationary frame via linear motion bearings, as illustrated in Figure 12. The rationale behind this configuration is discussed in the load cell paragraph (Section 2.5.2).

The PDE is supported by linear bearings: this configuration enables precise thrust measurements.

- The selected bearing model is the THK® SSR20XW1SS(GK) Block, produced by THK® Europe, as shown in Figure 9.

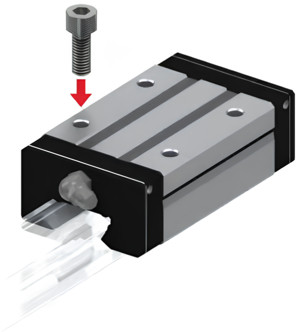

Figure 9: THK® SSR20XW1SS(GK) Block bearing [6]

  This heavy-duty linear guide system, entirely made of stainless steel, ensures high robustness and reliability. It offers excellent load capacity and precision, making it ideal for handling the impulsive forces generated by detonation events. Thanks to its ball recirculation mechanism, it also provides exceptionally smooth motion. The cost per bearing is €126,63. Figure 9 also illustrates the correct installation method on the rail.

- The corresponding linear rail/slide is the THK® SSR20, available in various lengths, such as 500 mm (SSR20-500L) and 800 mm (SSR20-800L) [6]. The rail length is to be chosen based on the final dimensions of the experimental setup. A cost comparison between different rail lengths is presented in Section 2.8. The prices for standard lengths are as follows:

  1. SR20-500L : €66,75;
  2. SR20-800L : €100,80;
  3. SR20-1200L : €146,22;
  4. SR20-1500L : €180,28.

- The PDE and the load cell are rigidly coupled, moving together as a single mechanical unit. This assembly must be mounted onto the THK carriages sliding along the rail. However, since the carriage mounting holes follow a standardized pattern and the PDE/load cell interface may differ, an intermediate plate is necessary. This structural adapter plate ensures both secure mounting and uniform load distribution. The adapter plate can be easily manufactured in a local workshop. As a reference, a compatible model is the Aluminum Plate 10x90 mm Alu DIN/EN-Platte (5083) (10mm thickness - 90 mm width), from Motedis® (Germany) [39]. Each plate costs €55,70. The number of plates required depends solely on the number of bearings and not on the overall dimensions of the setup; two plates are always used.

- The detonation tube is realized using a hollow stainless steel pipe. Its wall thickness must be selected to ensure structural integrity against the high internal pressures generated by the detonation process. To determine the required thickness of the stainless steel detonation tube, a preliminary structural analysis is performed. The primary stress component in this case is the hoop stress, as the internal detonation pressure acts to expand the tube, placing the circumferential fibers in tension. The hoop stress, therefore positive, is given by the following expression:

$$\sigma_{\text{hoop}} = \frac{pR}{t} \cdot \phi \tag{18}$$

where:

- $p$ is the internal pressure. More precisely, it represents the difference between the Chapman–Jouguet pressure and the ambient pressure outside the tube. However, for a conservative (worst-case) scenario, such as operation in a vacuum (e.g., in space), the ambient pressure is assumed to be zero;
- $R$ is the tube radius;
- $t$ is the tube thickness;
- $\phi$ is a dynamic amplification factor that accounts for the fact that the internal pressure is not static. It multiplies the static hoop stress ($\frac{pR}{t}$) to yield the dynamic hoop stress. This factor depends on the velocity of the detonation wave and typically ranges between 1 and 4. Since hydrogen–air mixtures produce one of the highest detonation velocities, a value of 4 is used in this case.

The internal pressure value is obtained from the CEA code results (Section 1.9.1), considering modifications to the initial conditions as necessary. For experimental purposes, the maximum internal pressure considered is not the one starting from atmospheric pressure. Instead, an initial pressure of 11 bar is assumed, as adopted in previous studies in the literature [40]. This approach allows for evaluating the advantages and disadvantages of increasing the initial pressure. Specifically, a higher initial pressure facilitates detonation initiation, reduces the DDT length, and increases the detonation velocity, as demonstrated later through CEA results in Section 2.5.2. Moreover, it minimizes the risk of detonation failure, thereby enhancing the reliability of the PDE.

A value of 11 bar is chosen as the maximum initial pressure for the experiment because the resulting pressure peak will be significantly higher, following the proportionality observed in PDE results. Consequently, a more robust structural design is required to withstand such pressures. If the initial pressure were set above 11 bar, the necessary structural thickness would increase to a point where the engine would become excessively heavy, rendering it impractical for real-world applications. Furthermore, higher initial pressures necessitate the use of heavier pressurized tanks or fuel compressors, further increasing the overall weight of the system. This additional weight must also be factored into the structural considerations, potentially negating the advantages of the PDE.

By equating $\sigma_{hoop}$ to $\sigma_{allow}$, which is the maximum allowable yield strength of stainless steel, the minimum required thickness can be determined using Equation (18). A safety factor (FS) of 3 is applied to account for extreme conditions, including high temperatures and repeated detonations. This value is supported by the literature [41]. Specifically, the high safety factor is justified because Equation (18) does not yet account for several real-world uncertainties, such as:

- material defects;
- manufacturing imperfections (e.g., non-uniform thickness);
- variations in mechanical properties due to temperature fluctuations or material aging;
- additional dynamic loads (vibrations, impacts);
- long-term degradation phenomena such as corrosion and fatigue, especially critical in PDEs due to the extremely high loading cycles.

To validate the use of Equation (18), a comparison with a documented past experiment is provided. In a test conducted by the Air Force Research Laboratory (US), a detonation tube with a 48 mm diameter and a 6.35 mm wall thickness was used.

Applying Equation (18) to this case:

- tube radius: $R = 24$ mm;
- material: stainless steel AISI 316, with a yield strength $\sigma_{\text{allow}} \approx 792$ MPa;
- initial conditions: $T_1 = 293$ K, $P_1 = 11$ bar, stoichiometric hydrogen-air mixture.

CEA results for these conditions are summarized in Table 9:

| Property | Value |
|---|---|
| $v_{detonation} [m/s]$ | 2009.1 |
| $P_2/P_1$ | 16.4 |
| $T_2/T_1$ | 10.6 |
| $\rho_2/\rho_1$ | 1.8 |

Table 9: CEA results for $H_2$/air mixture at 11 bar and 293 K

Thus, the peak detonation pressure is:

$$P_2 = \frac{P_2}{P_1} \times P_1 = 180.4 \text{ bar} = 18.04 \text{ MPa} \tag{19}$$

Using Equation (18), the minimum required thickness is:

$$t = \frac{P_2 \times R}{\sigma_{\text{allow}}} \cdot \phi \times FS = \frac{18.04 \times 24}{792} \cdot 4 \times 3 = 6.56 \text{ mm} \tag{20}$$

This result closely approximates the 6.35 mm thickness used in the experimental setup, confirming the correctness of the analysis [42].

The cost of the stainless steel tube depends on its length and thickness, with the dimensions discussed later in Section 2.8. Following the same procedure used in Equation (20), the required thickness for different tube radii is plotted in Figure 10, assuming:

- initial pressure $P_1 = 11$ bar;
- initial temperature $T_1 = 293$ K;
- stoichiometric hydrogen-air mixture.

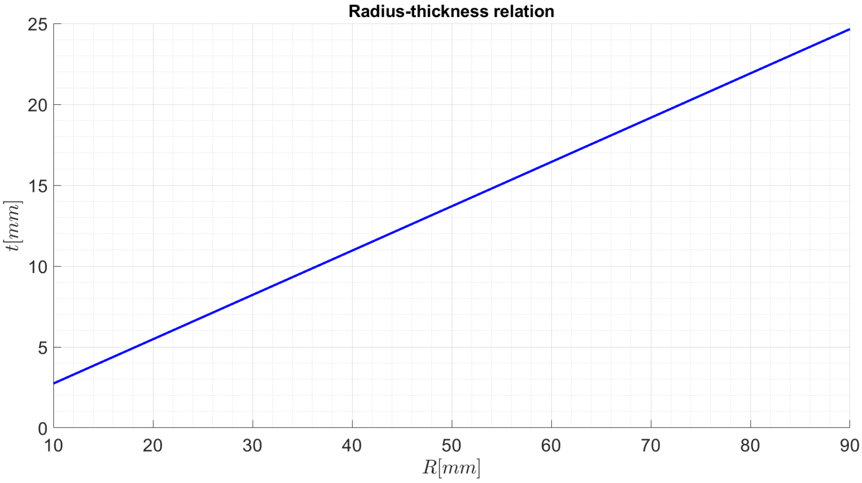

Figure 10: Required tube thickness as a function of radius for the PDE

Currently, suitable off-the-shelf stainless steel tubes are not available for the required dimensions. For instance, although a diameter of 48 mm is required, commercial tubes typically offer a maximum wall thickness of only about 2 mm, which is insufficient. Thus, a custom manufacturing process is necessary. The cost for this custom tube, produced by Fratelli Pinato® (Italy), is €120.

- Thrust stand: the detonation tube and linear guide system require a robust support structure, namely test bench structure. The frame is built using 45x90 mm aluminum profiles, selected for their strength and modularity. The selected model is: Aluminum profile 45x90L, from Nikai® (Spain), shown in Figure 11.

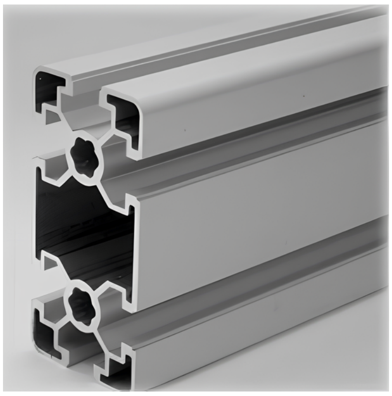

Figure 11: Aluminium profile, Nikai® [7]

Each profile costs €27,40, and approximately four profiles are needed.

A schematic overview of the structural components of the final experimental setup is shown in Figure 12.

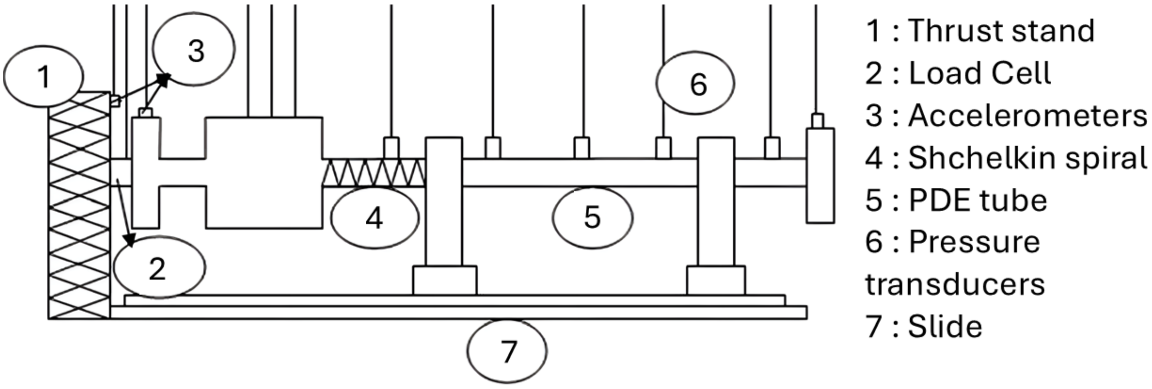

Figure 12: Schematic of the PDE structural components [8]

Note:

- for simplicity, thermocouples are not shown in the schematic. As explained later (Section 2.5.2), thermocouples are co-located with the pressure transducers. Thus, the marker "6" in Figure 12 represents both pressure transducers and thermocouples;
- the number of sensors depicted is only indicative and may differ from the actual number used in the experiment, which is discussed in Section 2.8;
- other components, such as ion sensors, are not depicted in this schematic for clarity, as the main purpose here is to highlight only the structural elements. A complete configuration, including all sensors, is presented in Section 2.7.

### 2.5.2 Instrumentation

**Pressure Transducers** Pressure transducers are mounted axially along the detonation tube to monitor pressure history, track peak pressures, and reconstruct shock wave patterns, which can be used to build models for performance evaluation. It is essential to verify that the transducers can withstand the conditions in the channel by comparing various datasheets to identify the best compromise between efficiency, durability in harsh conditions and cost.

For pressure range measurements, the CEA results for a stoichiometric $H_2$/air mixture starting from 11 bar and 300 K are considered, as this is the maximum pressure of interest for the experiments, as stated earlier in Section 2.5.1. This detonation pressure is used to evaluate the pressure range required for the transducer.

| Property | Value |
|---|---|
| $v_{detonation}[m/s]$ | 2008.6 |
| $P_2/P_1$ | 16.0 |
| $T_2/T_1$ | 10.3 |
| $\rho_2/\rho_1$ | 1.8 |

Table 10: CEA results for $H_2$/air mixture at 11 bar and 300 K

The decision to size the pressure transducer for an initial pressure of 11 bar becomes evident upon comparing Table 10 with Table 3, which refers to an initial pressure of 1 bar. The ratios for 11 bar are higher, indicating that the pressure to sustain will also be greater. Specifically, the detonation pressure, $P_2$, is calculated as:

$$P_2 = \frac{P_2}{P_1} \cdot P_1 = 16.0 \cdot 11 = 176.0\,\text{bar} = 17.60\,\text{MPa} \tag{21}$$

Thus, the transducer's measurement range should exceed this value. Furthermore, as shown in Table 10, the detonation velocity and performance increase with pressure, as previously discussed in Section 2.5.1.

Given the need for a flexible and adaptable design suitable for both PDEs and RDEs, piezoresistive transducers are a more suitable choice than piezoelectric ones. Piezoelectric transducers cannot measure both static and dynamic pressures, making them unsuitable for RDEs. On the other hand, piezoresistive transducers provide a more comprehensive pressure profile, capturing both rapid oscillations and mean pressure trends. Piezoresistive transducers are also more suitable for continuous pressure tracking over time, and their miniaturization makes them ideal for aerospace applications. Furthermore, unlike piezoelectric sensors, piezoresistive sensors do not require external amplifiers or special cables, offering a significant advantage in terms of system simplicity and cost. As discussed in Section 2.5.6, signal conditioning is not necessary, allowing these sensors to be directly connected to the data acquisition system.

The piezoresistive sensor is selected to be made of silicon, which is an excellent piezoresistive material. Silicon's electrical resistance changes when subjected to mechanical stress, with a much larger effect than in metals. As stress is applied, the mobility of charge carriers in the silicon changes, altering its resistivity. When piezoresistors are placed in a Wheatstone bridge configuration, the change in resistance is converted to a voltage output proportional to the applied pressure.

To build the experimental rig, it is crucial to understand how to properly mount the transducers along the detonation tube. The transducers are screwed into a connector, which is sealed with a Bridgman seal, composed of three different materials, as illustrated in Figure 13. This seal is capable of withstanding up to 400 bar, and is specifically designed to prevent gas or liquid leakage in high-pressure systems. The Bridgman seal is particularly effective in high-pressure applications, ensuring gas-tight sealing and measurement accuracy.

Since the mounting of the transducers is critical to their dynamic performance, the same layout must be used for all locations, while maintaining consistent torque settings for all transducers and fittings during shock tube measurements to ensure the reliability and comparability of the results.

Since industrial pressure transducers typically have operating temperatures lower than the detonation tube's temperature, they must be placed inside water jackets to protect them from extreme heat and prevent thermal drift. Water-cooled adapters allow pressure sensors to operate in applications with temperatures well above the operating range of the sensor by providing a stable localized lower temperature environment. The selected material for the jackets is high-strength stainless steel for the motivations illustrated before. This part is detailed later in the cooling section 2.5.7.

For the supplier, European providers are preferred due to faster availability and fewer uncertainties associated with the global market. For this reason, providers such as Kulite® (USA) and Sino CERA® (China) are considered, but the selected choice is Variohm Eurosensor® (UK).

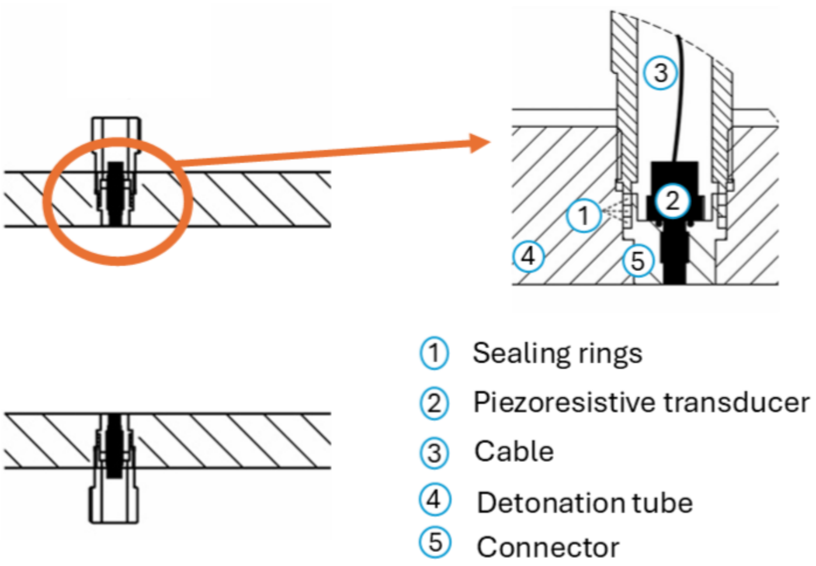

Figure 13: Detailed illustration of the piezoresistive transducer mounted along the detonation tube [9]

Upon comparing the datasheets of piezoelectric and piezoresistive transducers, it can be noted that piezoresistive sensors offer more flexibility in packaging due to the extremely small size of the sensing element. Piezoresistive sensors can have diameters smaller than half that of the smallest commercially available piezoelectric pressure transducers, making them an excellent choice for aerospace applications. As such, piezoresistive sensors are selected for this application, even though they are more commonly used for RDEs. The goal of this test is to make the PDE design versatile, allowing it to be easily converted into an RDE in the future. Moreover, selecting piezoresistive sensors aligns with the growing trend in research towards this technology, as it offers advantages in miniaturization and harsh environment performance. In contrast, piezoelectric sensors typically have a limited pressure range. For example, the Variohm Eurosensor® piezoelectric pressure sensor, EPT2100, has a pressure range from 250 mbar to 40 bar, which is insufficient for the experiment's maximum pressure of 176 bar (Equation (21)). On the other hand, the EPT3100 piezoresistive pressure transducer can measure up to 2000 bar. Since the maximum pressure required for this application is 176 bar, the EPT3100 is selected, with a pressure range up to 350 bar.
The EPT3100 is a high-quality, all-stainless steel pressure transducer. It features additional protection against Electromagnetic Interference (EMI) and Radio Frequency Interference (RFI), as well as low static and thermal errors, and high resistance to shock and vibration. This ensures reliable operation at temperatures of up to 125°C, highlighting the need for cooling due to the operational temperature range. The EPT3100 guarantees excellent accuracy and long-term stability. It already incorporates a Wheatstone bridge, as its output is a voltage (0-10V). Therefore, it can be directly connected to the multichannel system without the need for an amplifier.
The price of the EPT3100-H-25000-B-4-A (94049001) is €163,54 each. The number of pressure transducers required depends on the dimensions of the test.

Figure 14: EPT3100 Piezoresistive pressure sensor, Variohm Eurosensor® [10]

**Thermocouples** High-frequency sensors are essential for combustion wave speed analysis and for confirming the existence of detonation. Similar to pressure sensors, thermocouples are installed along the detonation tube. The number of thermocouples, like that of pressure transducers, depends on the size of the test facility, which is discussed in Section 2.8. The thermocouples selected for this application have a temperature range so as to enable the measurement of wall temperature. The wall temperature increases with both operating frequency and experimental runtime, but typically remains below 800°C. It is important to note that water-cooling measures for pressure transducers may have a slight impact on the measured wall temperature. To minimize this effect, thermocouples are positioned symmetrically with respect to the pressure transducers.
Both pressure transducers and thermocouples are evenly spaced to ensure uniform measurement.

Due to their short response time, thermocouples are the most effective sensors for temperature measurement in PDE applications. The selected thermocouple is Type E, which has an operating temperature range of -200° C to 900° C, making it particularly suitable for tracking rapid temperature fluctuations during detonations. The thermocouple used in this study is the MCT 19 model from Müller Instruments® (Germany), as shown in Figure 15.

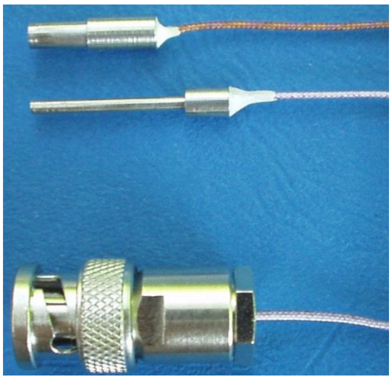

Figure 15: Thermocouple MCT 19, Müller Instruments® [11]

With its compact dimensions (1.9 mm diameter, 26 mm length), this thermocouple can be seamlessly integrated into complex geometries. The thermocouples are coaxial, allowing for high-frequency measurements and adaptability to different surface shapes. From the measured surface temperature, the convective heat flux can be derived, considering the sensor as a semi-infinite body and given the known properties of the wall material.

In PDEs, rapid temperature changes occur during detonations, necessitating a sensor capable of responding instantly. This thermocouple is particularly well-suited for PDE applications due to its fast response time of only $3\mu s$. Type E thermocouples are specifically chosen for their high sensitivity and rapid response, ensuring accurate real-time temperature monitoring. They are composed of:

- Chromel (90% Ni, 10% Cr);
- Constantan (55% Cu, 45% Ni).

This material combination is highly suitable for high-temperature conditions, typical of PDEs. Type E thermocouples have the highest electromotive force (EMF) per degree among common thermocouple types, producing 63 µV/°C, as stated in the datasheet [11]. This high sensitivity is crucial for applications where temperature variations occur rapidly, requiring fast and precise sensing.

Additionally:

- Chromel exhibits high oxidation resistance at elevated temperatures;
- Constantan remains stable and does not degrade easily in extreme environments with combustion gases;
- unlike Type K thermocouples, Type E thermocouples are more reliable in low-oxygen environments where Type K thermocouples may degrade.

Predicting the useful lifespan of a thermocouple is challenging, even with detailed knowledge of the operating conditions. In practice, the best approach is to install, test, and evaluate the performance under actual working conditions. For Type E thermocouples, the expected duration of operation is:

- unlimited at $< 100°$C;
- approximately 35 minutes at $615°$C;
- approximately 8 minutes at $715°$C.

In such cases, the thermocouple can be refurbished by re-grinding the sensor surface, effectively extending its lifespan indefinitely. However, since active cooling is applied in this setup, it is unlikely that refurbishment will be necessary, as the wall temperature is maintained below these critical thresholds.

One significant advantage of the MCT 19 thermocouples is their versatility in installation. They can be directly adhered to the detonation tube surface without requiring special adapters. This eliminates the need for threads or clamps, which would otherwise complicate the installation process. For mounting on a curved wall, as in this case, the manufacturer recommends applying a small drop of glue, such as Stabilit Express. However, deepening the analysis, the most adequate glue is the Epoxy Paste (DP55) of Ardex Cemento® company (Spain). Its cost is €7,15/kg [43].

In applications involving high initial temperatures or elevated pressures, the use of an additional threaded mounting is advised. Therefore, it is deemed appropriate to also acquire the M2 thread for this setup.

To ensure versatility and facilitate a potential conversion to an RDE setup, this thermocouple, being suitable for high-frequency measurements, remains a valid choice.

However, for long-duration or quasi-steady-state measurements, a cold junction compensation with a secondary thermocouple is required. This minor modification would allow the same thermocouple to be effectively used in both transient and steady-state conditions.

It is important to note that the thermocouple measurements reflect only the surface temperature, not the gas temperature. Even though the gas temperature during a detonation can reach several thousand degrees, the inner surface of the chamber, which corresponds to the thermocouple tip temperature, remains significantly lower due to the short duration of the event.
However, by analyzing the temperature variations along with the thermocouple's caloric properties, the heat flux can be determined. For this purpose, the manufacturer strongly recommends using their proprietary Heat Flux Calculator, which processes measurement data and calculates the heat flux within seconds.

The price of the MCT 19 thermocouple is €1195, while the M2 thread costs €80.

**Amplifier** As indicated in the thermocouple datasheet [11], an amplifier is required because thermocouples generate extremely small voltage signals, which must be amplified to be usable by measurement instruments or data acquisition systems. Specifically, the thermocouple used in this study has a sensitivity of 63 $\mu V/K$, as stated earlier. This signal is too weak to be directly read by most data acquisition devices. An amplifier converts the thermocouple's microvolt-level signal into a higher-level signal (in the volt range), making it easily readable by electronic systems. Additionally, thermocouple signals are highly susceptible to EMI from motors, power cables and other electronic devices. An amplifier plays a crucial role in filtering out noise and improving measurement accuracy.

To ensure optimal compatibility, the same provider as the thermocouple is selected: Müller Instruments®. The recommended model, as specified in the thermocouple datasheet, is the Multi-Function Amplifier MFA 1000, shown in Figure 16.

Figure 16: Front and Back side of MFA 1000 including power supply (3rd Generation), Müller Instruments® [12]

The MFA 1000 is a precision high-frequency amplifier with adjustable amplification factors, designed to supply and amplify piezoresistive pressure sensors, thermocouples and similar sensors. It is a fundamental component of this experimental setup due to its wide frequency range, covering all settings above 1 MHz, making it suitable for high-speed data acquisition. Its unique capabilities make it particularly well-suited for experiments involving shock waves and explosion waves, where data must be acquired rapidly. Therefore, it is the perfect choice for this experiment.

Beyond its application in PDEs, the MFA 1000 can also be effectively used in stationary processes. This means that if the experimental setup is later converted from PDE to RDE operation, the amplifier will remain suitable, even when the detonation wave stabilizes.

The MFA 1000 is a high-frequency voltage amplifier with an integrated sensor power supply. It is available in various configurations, housed with 2, 6, or 10 amplifiers. The exact number of amplifiers required is determined once the detonation tube size is discussed, as this defines the number of thermocouples necessary for the experiment. The cost of the voltage amplifier MFA 1000 is €2480.

**Ion sensors** Ion sensors are commonly employed in spark-ignition piston engines to detect knock, misfire and flame flashback. Although their application in PDEs is relatively uncommon, they are considered highly valuable as they enable more precise measurements. Whether a detonation or a deflagration, the heat of combustion and the chemical reactions in the tube of the experiment create ions that are detectable by an ion sensor. For chemical ionization to take place, the energy released during combustion must be comparable to the ionization energy of the atoms and molecules formed. The sensor detects deflagration or detonation when the concentration of ions is sufficiently high to allow electrical conduction within the circuit. This conduction is indicated by a voltage drop across a resistor, followed by an exponential rise as the sensor recharges. By placing two ion sensors at a fixed distance apart, the velocity of the combustion wave can be determined. This velocity measurement facilitates the classification of the event as either a detonation or a deflagration. Although temperature could also serve as an indicator of detonation, even the fastest response thermocouples are not fast enough to accurately capture the rapid temperature increase associated with a detonation wave. Consequently, ion sensor probes are utilized to determine whether the ions generated by the shock wave are detectable. This represents a notable innovation compared to many previous experiments, which have typically not employed ion probes. The use of ion sensors is expected to provide a more detailed and accurate understanding of the phenomena occurring within the detonation channel.

Previous experimental setups that incorporated ion probes primarily focused on hydrocarbon -fueled systems rather than hydrogen-fueled configurations. As outlined in Section 1.6.2, hydrocarbons are less prone to detonation than hydrogen/air mixtures. Consequently, it is more critical and urgent to determine whether detonation occurred in hydrocarbon-fueled cases, as it is inherently less likely to occur compared to hydrogen-fueled systems. However, employing ion sensors in hydrogen-fueled experiments allows for further investigation into the mass flow rate, pressure and temperature conditions necessary to establish the minimum requirements for detonation. Identifying these conditions could lead to a more efficient configuration with reduced mass flow requirements, ultimately decreasing the weight and dimensions of the fuelling system.

The primary advantages of ion sensors include their extremely short response time, design flexibility and ability to directly monitor reaction fronts of varying intensities within combustion chambers. Structurally, an ion sensor resembles a needle, typically composed of nickel or tungsten.
The needle's tip is inserted into the combustor, while the opposite end is soldered to a shielded cable connected to an analog-to-digital converter within the data acquisition system. When a positive potential is applied to the needle, the movement of charged particles near it changes, decreasing the density of positive ions while increasing the density of electrons and negative ions. Electrical conductivity near the needle can then be measured as an electric current via a measuring resistor.

The decision to apply a positive potential to the needle is based on several considerations. In principle, both negative and positive potentials can be applied. With a negative potential, positive ions are attracted to the needle. However, studies on the effects of electric fields on flames indicate that the movement of positive ions can alter the flame shape, leading to the phenomenon of ionic wind. Conversely, when a positive potential is applied, the needle collects negative charge carriers without affecting the flame's shape. The needle's electric field does not create new charge carriers; it only detects those already formed by chemical reactions. Given these factors, applying a positive potential to the needle is preferable. Furthermore, the removal of both negative and positive charge carriers has no significant impact on the chemical reaction process. This ensures that the ion sensor introduces minimal perturbations into the combustion process, maintaining the integrity of the measurements.

Ion sensors based on conventional automotive spark plugs offer several operational advantages:

1. they can withstand extreme temperatures and tolerate significant pressure variations;
2. ion sensors, unlike pressure and optical sensors, are well-suited for long-term testing under repeatable DDT in a PDE or RDE;
3. finally, ion probes are both inexpensive and robust.

The wave speed, $U$, is calculated using the time-of-flight methodology between ion probes, as expressed in Equation (22):

$$U = \frac{X_{IP,(i+1)} - X_{IP,i}}{t_{IP,(i+1)} - t_{IP,i}} \tag{22}$$

The ion probe signals exhibit a rapid voltage drop as the detonation wave passes, allowing the time difference ($t_{IP,(i+1)} - t_{IP,i}$) to be extracted. Given the known spacing between ion probes ($X_{IP,(i+1)} - X_{IP,i}$), the wave speed can be calculated. It is beneficial to mount ion sensors in the middle of the Shchelkin spiral to accurately assess its effect.

Regarding the adaptability of this experimental setup for conversion to an RDE, ion sensors play a crucial role in RDE because:

- they allow the evaluation of the rotation frequency of the detonation wave using Fourier transforms;

- the voltage trace is analysed to identify peaks corresponding to wave arrival times and to derive frequency response and power spectra;
- by comparing the rotation frequency measured by ion sensors with that recorded by pressure transducers, their consistency can be verified;
- using ion probe measurements in combination with known probe positions, wave directionality and speed can also be determined for an RDE configuration.

Therefore, this type of sensor is valuable for both PDE and RDE applications without requiring design modifications of this type of probe. For an annular RDE, ion sensors are installed on the RDE combustor wall with threaded mounts flush with the inner combustor surface, sealed using silicone sealant.
For the RDE case, the time interval between consecutive pulses observed in the ion probe voltage differential data represents the cycle time. This time can be used to estimate the average rotational wave speed. Accordingly, Equation (22) simplifies to:

$$s = \frac{\pi D}{t_{\text{Rot}}} \tag{23}$$

where:

- $t_{\text{Rot}}$ is the time between two consecutive spikes in the ion sensor differential data, corresponding to the time taken by the detonation wave to complete one full rotation within the RDE channel;
- $s$ is the average rotational wave speed;
- $D$ is the outer diameter of the RDE channel;
- $\pi D$ is the outer circumference of the RDE channel.

The possible challenge associated with the employment of ion sensors for PDEs or RDEs is that hydrogen combustion may lead to water deposition on tube walls, forming weak electrolytes that can cause sensor short circuits.

Ion sensors have a wide dynamic range of ion current and a response time of only $2\mu s$, making them perfectly suitable for this experiment. The spark plug selected for the ion sensor is the NGK Spark plug C9E (7499), manufactured by SparkPlugs® (UK). This spark plug features nickel alloy electrodes and is depicted in Figure 17.

Figure 17: Spark Plug NGK C9E (7499), SparkPlugs® [13]

The pure alumina silicate ceramic insulator provides strength and allows operation at extreme temperatures, such as those encountered in a PDE or RDE. As previously mentioned, this sensor is highly cost-effective, priced at €6,68 per unit. As stated earlier, the number of ion sensors is constant (two), regardless of the experimental setup dimensions.

**Flow meters** Accurate measurement of the mass flow rates of fuel and oxidizer is essential for assessing the performance of a PDE, particularly in terms of specific impulse and specific thrust. Another critical performance parameter is the filling fraction of the detonation tube, which refers to the volume percentage occupied by the reactant mixture during the filling phase. Prior studies have demonstrated that partial filling of the detonation tube can enhance PDE performance.
To monitor the fuel and oxidizer mass flow rates, dedicated flow meters are installed in their respective supply lines. This allows for the selection of flow meters most suited to each gas type. Since the flow meters are installed upstream of the detonation tube, they are not subject to extreme pressure or temperature conditions. As one flow meter is used for each of the two propellants, fuel and oxidizer, the total number (i.e., two) and associated cost of these components remain constant, regardless of the detonation tube dimensions. This contrasts with pressure transducers and thermocouples, whose required quantity and cost scale with the size of the tube.

For the oxidizer line, the selected flow meter is the CS Instruments VA 500 (CS Instruments GmbH & Co. KG ®, Tannheim, Germany), as shown in Figure 18a. This sensor features a compact design with an integrated display showing flow rate, gas velocity and temperature. It is compatible with multiple gases, including air, nitrogen, argon, nitrous oxide, $CO_2$, oxygen and natural gas. Because the VA 500 is not compatible with hydrogen, a different flow meter must be selected for the fuel line. The VD 500, manufactured by CS Instruments GmbH & Co. KG ®, is selected as it serves as the hydrogen-compatible counterpart to the VA 500.
According to its datasheet [44], VA 500 can operate at pressures up to 50 bar, well above the 11 bar maximum expected in the oxidizer supply line. Similarly, the VD 500 is rated for operation at pressures up to 20 bar [45], making it fully suitable for the experimental conditions. Regarding the temperatures, the flow meters' datasheets specify a maximum allowable pre-heating temperature that the system can withstand: 70°C for the oxidizer and 180°C for hydrogen. These limits must be carefully considered during the experimental campaign.

The flow meter configuration used in the experimental setup is also applicable to an RDE without requiring any modifications. Consequently, the objective of establishing a versatile experimental configuration is successfully met, even with this type of sensor.

It is crucial that the recorded pressure, temperature and flow rate for each test are synchronized between the two flowmeters to improve data accuracy and enable precise evaluation of performance parameters.
The cost of the VA 500 is €2592, while VD 500 is priced at €4300.
The selected flowmeters are equipped with a Modbus output; therefore, neither an amplifier nor an analog-to-digital converter is required, as the data is already provided in a precise digital format. All data are acquired and logged using LabVIEW® software interfaced with pressure transducers, thermocouples and load cell, or alternatively, using MATLAB®.

(a) CS Instruments VA 500, CS INSTRUMENTS GmbH & Co KG ® [44]

(b) CS Instruments VD 500, CS INSTRUMENTS GmbH & Co KG ® [45]

Figure 18: Flow meters for oxidizer and fuel

The specific impulse can be evaluated from the pressure, temperature and volumetric flow rate data as follows. First, the volumetric flow rate measured by the flow meter is converted to a mass flow rate using the equation:

$$\dot{M}_i = \rho_i v_i \tag{24}$$

where $\rho_i$ is the density of the i-th species (oxidizer or fuel) and $v_i$ is the volumetric flow rate of the i-th species. The density $\rho_i$ is determined using the measured pressure ($p_i$) and temperature ($T_i$) from the sensors incorporated in the mass flow meter, according to the following equation:

$$\rho_i = \frac{p_i}{R_i T_i} \tag{25}$$

where $R_i$ is the specific gas constant. Once the mass flow rates for both fuel and oxidizer are determined, the equivalence ratio $\phi$ is calculated as:

$$\phi = \frac{\dot{M}_{\text{fuel}} / \dot{M}_{\text{oxidizer}}}{\left(\frac{\dot{M}_{\text{fuel}}}{\dot{M}_{\text{oxidizer}}}\right)_{\text{stoichiometric}}} \tag{26}$$

The total specific impulse is then calculated using the mass flow rates obtained from Equation (24), the thrust ($T$, measured by the load cell) and the gravity acceleration ($g$) as follows:

$$I_{\text{sp}} = \frac{T}{g(\dot{M}_{\text{fuel}} + \dot{M}_{\text{oxidizer}})} \tag{27}$$

Finally, the fuel-specific impulse, which is useful for comparisons and is employed in Section 1.8, is calculated as:

$$I_{\text{spf}} = \frac{T}{g\dot{M}_{\text{fuel}}} \tag{28}$$

**Load Cell** A load cell is used to measure the thrust generated by the PDE. Two configurations are considered and compared.

The first setup involves measuring the thrust generated at the closed end of the PDE tube using a load cell integrated into a spring-damper mechanism. The PDE tube is mounted on a low-friction rail that permits motion in the x-direction, as depicted in Figure 19. The load cell is placed vertically beneath the experimental model, connecting the movable system to the fixed test rig. It is axially aligned with the PDE to minimize errors and measure thrust exclusively in the x-direction. The chosen load cell for this configuration is the STA-3-100 from LCM Systems® (Newport, UK) [46]. The cost of this model is €195,28.

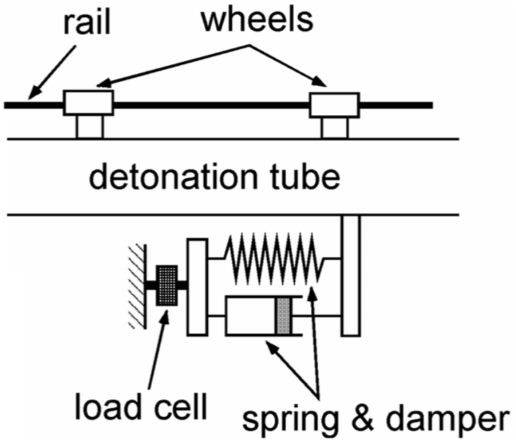

Figure 19: Schematic diagram of the load cell in the experimental setup [14]

The load cell requires signal amplification [46]. However, the amplifier used for thermocouples is incompatible due to differing signal characteristics. The amplifier selected for the first configuration is the Model 9236-V300 from Burster Präzisionsmesstechnik GmbH & Co® (Germany) [47]. The cost of the amplifier (1 channel version) is €322,50.

To mitigate electrical noise, a low-pass filter is to be implemented with a cutoff frequency below 60 Hz. This choice reduces power line interference (typically 50 or 60 Hz) and ensures that only relevant low-frequency signals from the load cell are recorded. The selected filter costs less than €10 and is easily sourced within the university; hence, no specific company is mentioned.

The spring and damper constants (k and c) of the mechanism must be experimentally determined. For this purpose, the history of the impulsive force from the PDE must be evaluated. Thus, the components are not specified yet, as the exact characteristics will be defined during testing. As a price reference, a typical spring suitable for this application costs approximately €5, while the damper does not exceed €100.

The accuracy of spring-damper system may degrade in single-cycle experiments due to structural acceleration and inertial effects. However, this method is well-established in prior experiments, which justifies its detailed discussion above.

For unsteady thrust measurements, a fast-response load cell is favored. This is the second configuration analysed: the PDE is mounted on a nearly frictionless rail and pushes against the load cell during detonation, as shown in Figure 12.

The measurement of unsteady thrust generated by PDEs is further complicated by stress waves, pulse-to-pulse interactions and cyclic oscillations. The high-frequency components introduced by stress waves are specific to each experiment—depending

on factors like material properties, engine geometry, and reflective surfaces—and must be filtered out. Importantly, these sources of error also affect systems using spring-damper mechanisms for time-averaged thrust measurements. Therefore, this issue is not unique to the second configuration and should not be viewed as a specific drawback of that approach.
To extract true thrust values, inertial forces caused by oscillations are compensated for. A transfer function characterizing the rig's dynamic response is obtained through impulse testing. By applying a known input (e.g., a single detonation wave), and measuring the output, the system's transfer function $h(t-\tau)$ is determined. This enables deconvolution of the thrust signal to recover the actual unsteady thrust by alleviating the effects of stress wave propagation and pulse-to-pulse interaction.

However, this deconvolution procedure alone is insufficient to isolate the true thrust, as it does not account for inertial contributions from structural motion. The vibrations of the test rig, particularly when large and massive, introduce additional forces that must be corrected separately. Assuming a linear relationship between the rig's acceleration and the corresponding inertial force, the acceleration-compensated thrust can be expressed as:

$$F_{\mathrm{comp}}(t) = \hat{F}(t) - m_{\mathrm{eff}}\, a_{\mathrm{filt}}(t) \tag{29}$$

where:

- $\hat{F}(t)$ is the deconvolved thrust signal derived from the system's transfer function;
- $m_{eff}$ is the effective oscillating mass of the structure;
- $a_{filt}(t)$ is the filtered acceleration of the thrust measurement rig;
- $F_{\mathrm{comp}}(t)$ is the true thrust output, corrected for inertial effects.

To determine the effective mass, the free vibration response of the system is analysed. This is achieved by delivering an impulsive force using an instrumented impact hammer and recording the structural oscillations with a load cell and an accelerometer mounted on the thrust stand.

Due to the rapid transients involved in PDE operation, the load cell must exhibit a very fast response time. For this configuration, the selected load cell is the 9323AAA, manufactured by Kistler® (Switzerland), as shown in Figure 20. This model offers high measurement accuracy (33 pC/N), as specified in the datasheet [15]. Its force range (0–5000 N) is well-suited to PDE applications. Based on piezoelectric sensing technology, the 9323AAA is particularly appropriate for high-frequency applications. Its mounting system is both simple and adaptable, with flanged connections on both ends allowing for compatibility with a wide range of mechanical setups. The unit cost is €2300.
In general, the thrust is expected to be oriented along the x-direction. In the event of any deviation from the x-axis, the load cell's sensitivity diminishes due to crosstalk [15]. In extreme cases, a multi-sensor setup (e.g., with four load cells) might be required. However, based on previous experiments, the thrust has consistently been along the x-axis. Nevertheless, this factor should be taken into consideration during testing.

Figure 20: Load cell 9323AAA, Kistler® [15]

The signal output from the load cell requires amplification. The recommended amplifier for this application is the 5018A1000, also by Kistler®, depicted in Figure 21.

Figure 21: Amplifier 5018A1000, Kistler® [16]

Only one channel is necessary, as a single load cell is employed. The amplifier is both accurate and versatile. Its price is €5000.

Following a comparative analysis of the two configurations considered, configuration 2 (involving the piezoelectric load cell and amplifier) is selected, despite its higher cost relative to configuration 1 (spring and damper system). This decision is made based on its significantly greater accuracy and its capability to capture rapid changes in unsteady thrust. Although configuration 2 is far more suitable for the intended application, configuration 1 has been described as a viable, cost-effective alternative that has been widely used in past experimental setups.

With regard to the usual emphasis on the versatility of the experimental setup to allow for an easy transition to an RDE configuration, the setup incorporating the load cell is also fully compatible with RDE testing, as illustrated in Figure 22. As in the case of the PDE, the load cell measurements in the RDE configuration must also be complemented by accelerometer data.

It is important to note that the load cell remains a single, fixed component regardless of the engine size, unlike pressure transducers and thermocouples, whose quantity and arrangement may vary depending on the length of the experimental setup.

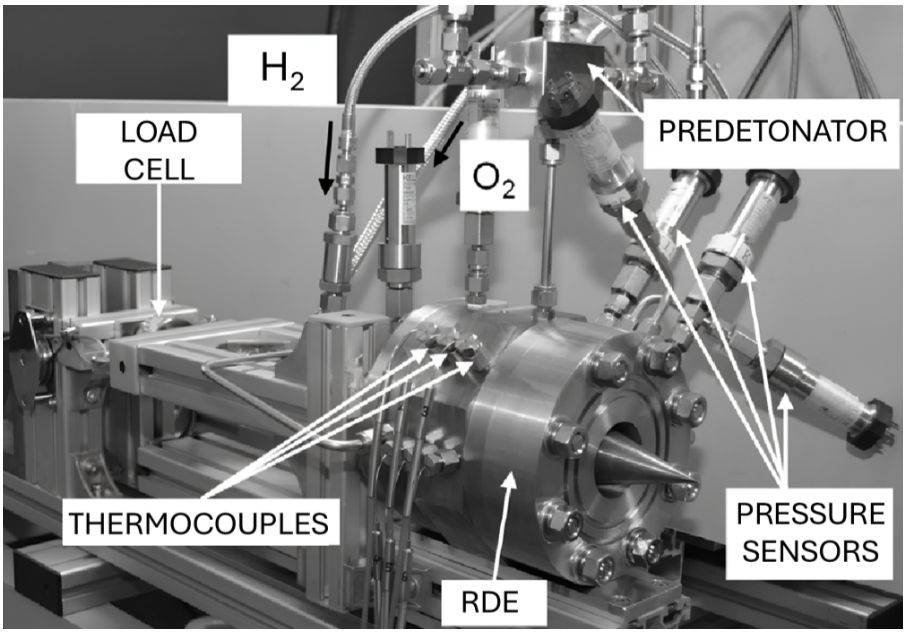

Figure 22: RDE thrust measurement apparatus [17]

As with the other sensors (pressure transducers, thermocouples and mass flow meters), data acquisition is handled via LabVIEW® or MATLAB®.

**Accelerometers** For the acceleration compensation procedure, as described in the section concerning the load cell, two accelerometers are utilized, as illustrated in Figure 12. One is mounted on the engine, and the other on the thrust stand. This configuration enables measurement of the acceleration of the entire structure during engine operation. The selected model is the 353B34 accelerometer from PCB Piezotronics® (German division), shown in Figure 23.

Figure 23: 353B34 Accelerometer, PCB Piezotronics® [18]

This sensor provides high sensitivity and is particularly well-suited for high-frequency applications, owing to its quartz sensing element. Its resonant frequency exceeds 22kHz [18], making it appropriate for use in a PDE system.
Regarding thermal conditions, as depicted in Figure 12, the accelerometers are positioned upstream of the DDT zone—where the Shchelkin spiral is located. Consequently, they are not exposed to the extreme temperatures sustained by the detonation tube. According to the datasheet, the operating temperature range of -54°C to +121°C

is more than adequate for this configuration [18]. The cost of each accelerometer is €560.
The 353B34 model is highly versatile in terms of mounting options, supporting six distinct installation methods, including standard mounting, adhesive mounting and threaded mounting.
It is important to note that the measured acceleration includes all excited vibration modes of the thrust measurement rig, as the selected accelerometer is capable of detecting frequencies up to 12 kHz [18]. Consequently, using the raw acceleration data may result in an overestimation of the inertial forces. Therefore, the signal is filtered before being used to compute these forces. A suitable method for filtering the acceleration signal is through the use of a Butterworth low-pass filter. The MAX291, an 8th-order Butterworth filter from Maxim Integrated® (USA), is selected for this purpose [48]. The unit cost is €9,62.

As previously discussed in the section on the load cell, this design is also compatible with RDEs, requiring no modifications. Furthermore, the cost remains unaffected by the dimensions of the PDE tube, unlike pressure transducers or thermocouples, since the number of accelerometers used remains constant—two units per setup.

Figure 24 illustrates the positioning of the instruments within the experimental setup.

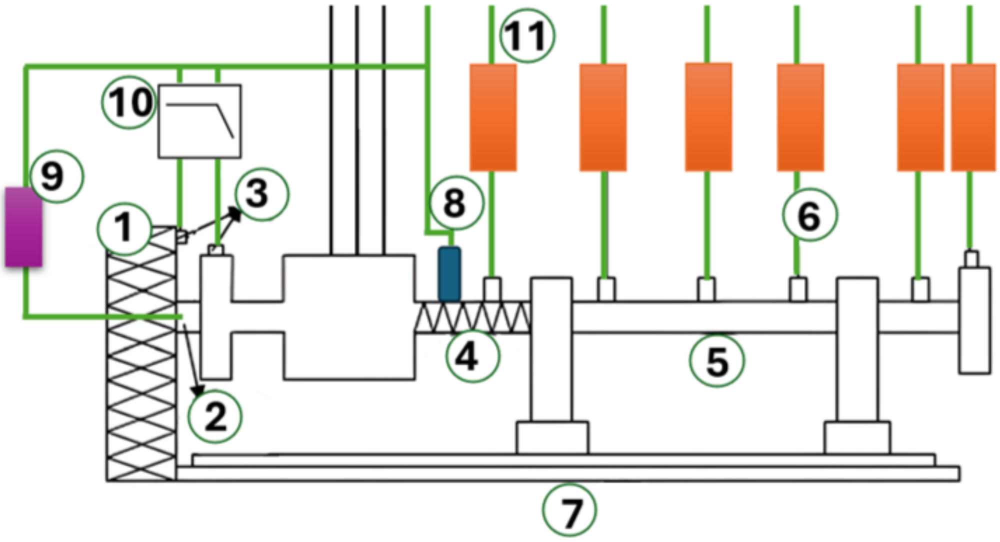

Figure 24: Schematic representation of the instruments in the PDE setup. 1) Thrust Stand; 2) Load Cell; 3) Accelerometers; 4) Shchelkin Spiral; 5) PDE Tube; 6) Pressure Transducers / Thermocouples; 7) Slide; 8) Ion Probes; 9) Amplifier for load cell; 10) Butterworth Low Pass Filter for accelerometers; 11) Amplifiers for thermocouples

For the sake of simplicity and clarity:

- only one ion sensor is shown: however, two are actually installed along the section with the spiral;
- wherever a pressure transducer is indicated, a thermocouple is also present in the same section;
- the number of sensors illustrated is indicative: the final number depends on the dimensions of the setup, as discussed in Section 2.8;

- flowmeters are not depicted in Figure 24, as they are located along the feeding line rather than along the detonation tube. They are included in the final schematic of the setup (Figure 48, Section 2.7).

**High speed camera** The high-speed digital camera is employed in this study to capture rapid transient phenomena associated with PDEs. Specifically, its usage serves the following purposes:

- to investigate whether detonation occurs;
- to analyse the flame propagation and identify the DDT;
- to study the evolution of the shock wave and other shock-dynamic characteristics during the initial stage of the exhaust flow;
- to visualize variations in velocity, density, flow direction and unsteadiness.

High-speed cameras are particularly beneficial in fluid dynamics research due to their high temporal resolution and non-intrusive nature, allowing detailed visualization of flow phenomena without disturbing the flow field.
The Schlieren technique is based on fundamental principles of optics. In a homogeneous medium (e.g., vacuum), light travels in straight paths at constant velocity. However, in an inhomogeneous medium such as a moving fluid, changes in refractive index cause light rays to bend (refract), resulting in observable distortions—known as schliere—which can be visualized using appropriate optical techniques. High-speed Schlieren imaging is therefore employed to capture fine-scale shock dynamics and density gradients in the exhaust region of the PDE.
A high-speed digital camera, Photron® FASTCAM NOVA S-SERIES S9 (Europe division) (Figure 25), is selected for its:

- megapixel resolution;
- ultra-sensitive sensor;
- ultra-high-speed capability (up to 775,000 fps).

These features make it particularly well-suited for capturing fast transient phenomena such as those occurring in PDEs. This represents an enhancement over previous experiments, which employed the FASTCAM SA-5. The NOVA S-Series camera offers several upgraded features, including improved sensitivity, a more advanced design, superior image quality, reduced noise and faster acquisition rates. Additionally, a key advantage of this camera is its upgradeability: it can be easily extended to a higher-end model without the need to purchase an entirely new system. Only certain hardware components need to be replaced. The onboard memory, used for recording events and image sequences, can also be upgraded—from the default 8 GB up to 128 GB. Therefore, if memory requirements are unclear at the beginning, the upgrade can be performed later without significant modifications or costs.
The optimal frame rate must be selected experimentally as it depends on the specific characteristics of the final setup and the speed of the detonation wave. Therefore, this parameter cannot be fixed at this stage.
The camera is available with either a color or monochrome sensor, with the latter being more suitable for this application.
The cost of a new camera of this type is approximately €40 000.

Figure 25: Photron® FASTCAM NOVA S-SERIES S9 [19]

It connects to the control PC via Ethernet, supporting speeds from 1 Gbit up to 10 Gbit. Additionally, an external high-speed drive can be connected for faster data transfer beyond 10 Gbit, allowing data to be written directly to the external drive.

To overcome the complexity and high cost of classical Schlieren setups, the Background-Oriented Schlieren (BOS) method is adopted as a modern, flexible and computational alternative. A schematic of the traditional setup used in previous experiments is shown in Figure 26. This classical z-type Schlieren system employs two 6-inch parabolic mirrors to collimate and refocus the light beam. Although effective, such a configuration requires bulky and expensive components:

- two AD131 parabolic mirrors at €145,31 each (GSO® (Taiwan));
- one knife edge from Edmund Optics® (UK) at €82;
- one collimator from Edmund Optics® (UK) at €370.

The total cost of these components amounts to $2 \cdot 145,31 + 82 + 370 = €742,62$.

To reduce these costs and simplify the experimental setup, the BOS method is implemented (Figure 27). It eliminates the need for large optical elements by relying on digital image processing of a patterned background viewed through a refracting medium. A pulsed LED light source, the Luminus® PT-120TE (Belgium), is selected for its compatibility with high-speed BOS imaging [49]. Its advantages include:

- excellent performance with frame rates exceeding 10000 fps;
- cost-effective solution (€128,48).

To create the random optical background required by BOS, 120-grit ground glass diffusers (Edmund Optics®, UK) are employed [50]. The diffuser must provide:

- uniform diffusion;
- high transmittance to allow the LED light to pass through efficiently;
- compatibility with high acquisition frame rates.

The cost of the diffuser is €17,75. Thus, transitioning from the traditional Schlieren setup to the BOS configuration results in net savings of $€742,62 - 17,75 = €724,87$.

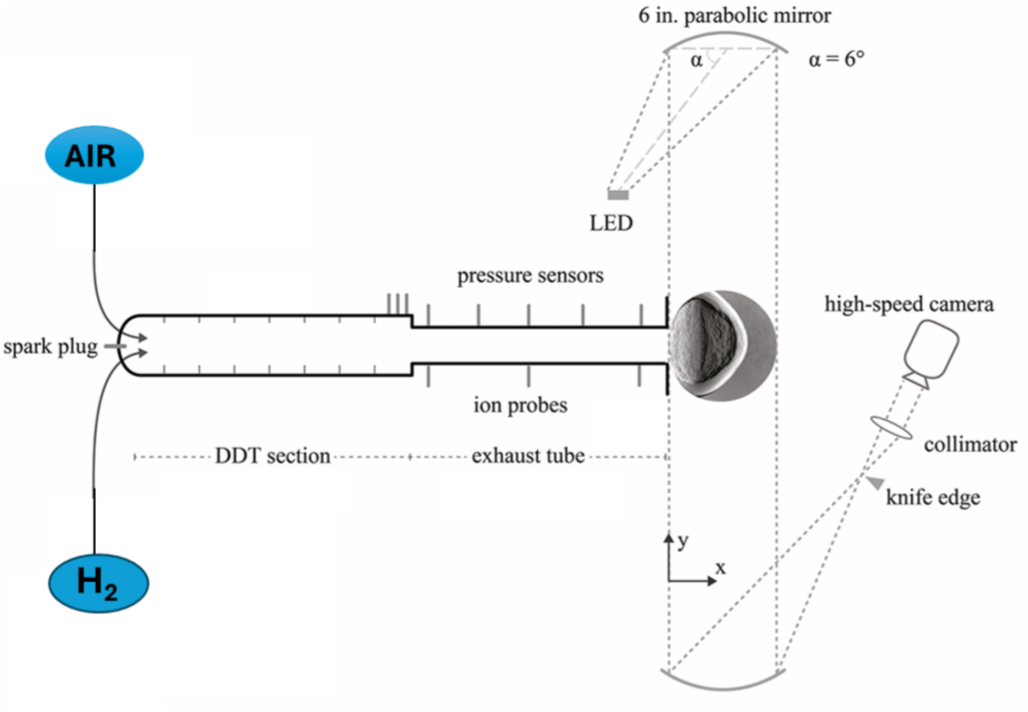

Figure 26: Illustration of the experimental setup featuring the pulse detonation combustor and high-speed traditional Schlieren system [20]

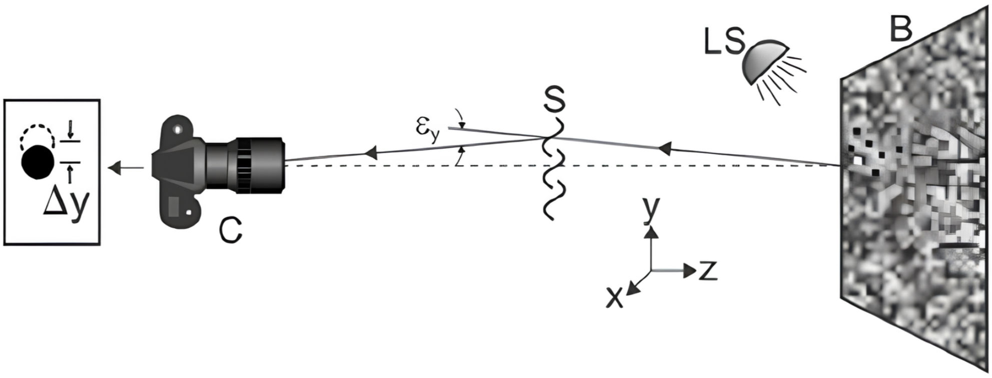

Figure 27: Schematic of the BOS setup [21]

For optimal performance with high-speed imaging systems, the BOS setup is arranged in transmission mode. A pulsed LED source is placed behind the patterned background, acting as a backlight, as shown in Figure 28. This configuration maximizes the light intensity reaching the camera, which in turn minimizes the LED pulse duration, enhancing both measurement sensitivity and spatial resolution.

During engine operation, exhaust-induced density gradients distort the background image. The high-speed camera captures both reference (undisturbed) and flow-disturbed images, which are later analysed using digital image correlation techniques.
Standard FFT-based cross-correlation algorithms (e.g., in MATLAB® or MatPIV®) are used to compute background displacement fields. Additionally, BOS can be used to estimate flow velocity fields by applying Particle Image Velocimetry (PIV) software to the displacement data.

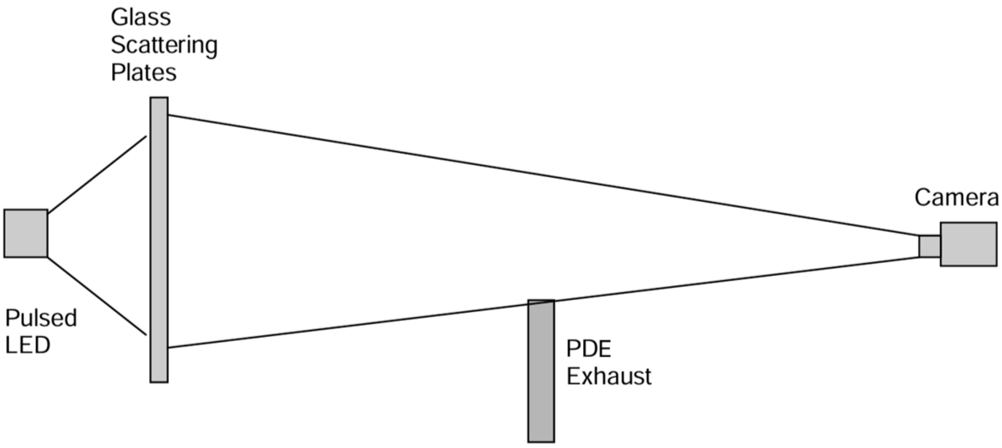

Figure 28: Scheme of BOS setup for PDE experiments [22]

The BOS technique employs a camera that captures images of a patterned background, and any variation in refractive index along the optical path (due to flow-induced density gradients) causes light rays to deviate slightly. These deviations appear as small displacements in the background pattern when compared to a reference image taken in quiescent conditions. As illustrated in Figure 27, a point on the background B that would normally be imaged along a straight (dashed) optical path is instead observed along a refracted (solid) path due to the presence of a Schlieren object S. The resulting lateral displacement $\Delta y$ on the image sensor is caused by the refraction angle $\epsilon_y$, which is related to the gradient of the refractive index. According to Schlieren theory, for a two-dimensional flow field and under the assumption of a constant gradient along the optical axis $z$, the refraction angle is given by:

$$\varepsilon_y = \frac{1}{n}\int \frac{\partial n}{\partial y}\,dz = \frac{Z}{n_\infty}\frac{\partial n}{\partial y} \tag{30}$$

where:

- $\epsilon_y$ is the refraction angle in the vertical direction;
- $n$ is the local refractive index;
- $n_\infty$ is the ambient refractive index;
- Z is the optical path length through the flow;
- $\dfrac{\partial n}{\partial y}$ is the refractive index gradient in the vertical direction.

For more complex or asymmetric flows, additional processing (e.g., Abel inversion or tomographic reconstruction) is required to recover quantitative density fields.
By converting the refraction-induced displacements ($\varepsilon_x$ and $\varepsilon_y$ ) into grayscale values across a 2D image matrix, a pseudo-Schlieren image is generated. This visualization closely resembles traditional Schlieren images and is sufficient for qualitative diagnostics in highly unsteady and complex flow fields, such as those in PDE exhausts.

In conclusion, the BOS technique offers significant advantages over traditional Schlieren methods, particularly in the context of PDE research:

- lower cost due to the elimination of mirrors, collimators and knife edges;

- simplified setup that is more compact and easier to align;
- wide field of view, useful for observing large-scale flow features;
- compatibility with high-speed imaging, enabling time-resolved visualization of transient shock and density phenomena.

For these reasons, it is increasingly recognized as a practical and cost-effective technique for advanced experimental fluid dynamics studies.

Regarding compatibility with an RDE configuration, the selected high-speed camera model is entirely suitable. This is supported by its prior use in RDE-related experimental studies. Similarly, the BOS setup remains fully applicable to RDE investigations, as outlined in Figure 28. A key aspect specific to RDE analysis is the determination of the average rotational speed of the detonation wave. This can be estimated through a digital image processing method to track the angular displacement of the wave across successive frames. The corresponding average wave speed is then computed using the following formula:

$$s = \frac{\pi D\,\theta/360}{n\tau} \tag{31}$$

where:

- D is the outer diameter of the RDE channel;
- $\tau$ is the time interval between consecutive frames;
- $n$ is the number of frames required for one full rotation of the wave;
- $\theta$ represents the angular displacement of the wave (in degrees) observed over $n$ frames.

These velocity measurements can be compared with those obtained from other diagnostic techniques, such as ion probes.

It is important to note that, regardless of the total tube length, only a single high-speed camera is required for the PDE/RDE visualization setup, as illustrated in Figure 28.

### 2.5.3 Fuel/oxidizer system

**Tanks** The system includes dedicated tanks for the oxidizer, the fuel and the purge gas (nitrogen). As previously stated, the maximum initial pressure for the propellants is 11 bar for experimental purposes; therefore, pressurized tanks are required.

- Pressurized Hydrogen Tank: a stainless steel tank certified for high-pressure hydrogen storage is selected. Given the lower density of hydrogen compared to air, a larger volume is required. This type of tank is commonly available through various suppliers and is often already present in university facilities. An indicative model is the 2000 L hydrogen storage tank provided by Wenzhou Rayen Machinery® (China), made of stainless steel and rated for a working pressure of up to 60 bar. Estimated cost: €1320.
- Compressed Air Tank: a 10-liter stainless steel tank (316L), rated for 11 bar. This type of tank is widely available and can typically be sourced within the university. An indicative model is the SERB0010-OR-INOX316L by APIPlus® (Italy), priced at approximately €550.

  - Nitrogen ($N_2$) Tank: a 10-liter steel tank rated for 200 bar. The selected model is the ALPHAGAZ 1 by Air Liquide® (Spain), with an estimated price of €111,32.

For simplicity, the dependency on the size of the experimental setup is not considered here, as the selected tank capacities are deemed sufficient for standard PDE configurations.

**Injectors** The selected gas injector is the AFS Gs60-05 5-C series, manufactured by Alternative Fuel Systems Inc® (Canada), as shown in Figure 29. This model is chosen due to its compatibility with hydrogen, air and nitrogen, as well as its fast response time, making it well-suited for high-frequency pulsed injection applications. Each injector is priced at €438,27. In the present study, they are used to achieve precise control over the timing and delivery of the propellants. The injectors are actuated by signals originating from the proximity sensor and the rotary valve, as described in the following paragraph. These signals are processed by the driver, which converts standard inputs into control currents necessary to operate the injectors' high-speed solenoids. The injectors demonstrate typical response times of less than 2 ms: this characteristic makes the AFS Gs60-05 5-C series particularly suitable for high-frequency gas injection in PDE systems.
The number of injectors is independent of the PDE tube length; it remains fixed at three units: one for hydrogen, one for air and one for nitrogen. As a result, the total injector cost is constant regardless of the scale of the experimental setup.

Figure 29: AFS Gs60-05 5-c series, Alternative Fuel Systems Inc ® [23]

With regard to the potential versatility for use in an RDE configuration, the same type of injectors can be employed to introduce the propellants into the predetonator, as illustrated in Figure 22, which corresponds to a standard PDE tube. Consequently, the injector configuration remains unchanged from that of the PDE, as the PDE can be considered an integral component of the RDE—specifically, serving as the predetonator section.

**Rotary Valve** The development of an effective valve system is critical to the practical realization of a PDE. The ability to intermittently supply the propellants while preserving the PDE's simplified structure demands a valve solution capable of achieving high mass flow rates and operating frequencies. This requirement is especially crucial for obtaining a high thrust-to-weight ratio.

Fuel and oxidizer injection in PDEs has traditionally been achieved through mechanical systems such as high-speed solenoid valves or rotary valves. While solenoid valves are widely used due to their fast actuation and simplicity, they exhibit critical limitations. Residual magnetism in the valve body often causes delays in valve closure,

limiting their operational frequency. Although high-speed solenoid valves can exceed 100 Hz, their individual flow capacity is typically insufficient for practical applications in PDEs. Scaling the flow by using multiple solenoid valves becomes infeasible for larger detonation tubes due to complexity, cost and system bulk. Therefore, solenoid valves cannot work efficiently beyond a certain frequency.
Given the shortcomings of solenoid valves, rotary valves have emerged as a promising alternative for high-frequency injection. Rotary valves can handle larger mass flow rates per unit and operate efficiently at elevated frequencies. Although these systems often require additional driving mechanisms—such as electric motors—and incorporate more complex mechanical structures, they offer a more scalable and robust solution. Additionally, rotary valves can be configured for single- or multi-tube PDEs. A multi-tube design can serve for an RDE, where multiple PDE tubes operate in sequence, as shown in Figure 22. Several rotary valve designs are reported in the literature, typically featuring a rotating component that opens and closes propellant passages.

This setup follows the recent trend toward rotary valve solutions and presents a coaxial rotary valve capable of injecting three separate gases—fuel, oxidizer, and purge gas—into the PDE combustor. The valve consists of three main components:

1. a top cover;
2. a rotary disk;
3. a casing.

All the components are constructed from aluminum alloy (A7075). Based on the dimensions used in a previous experiment, the rotary disk (diameter: 92.6 mm) is enclosed between a top cover and a square casing (100 mm × 100 mm). It is driven by an external electromagnetic motor, as illustrated in Figure 30.

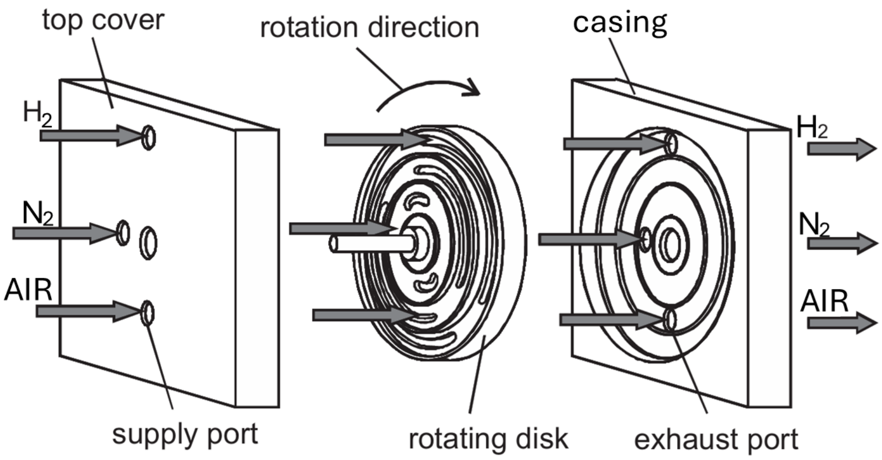

Figure 30: Schematic of a coaxial rotary valve [24]

The rotary disk features elongated ports that align with the supply and exhaust holes on the top cover and casing during operation. As the disk rotates clockwise, the long holes intermittently match the ports (marked as black dots in the top view in Figure 31), enabling gas injection into the combustor.

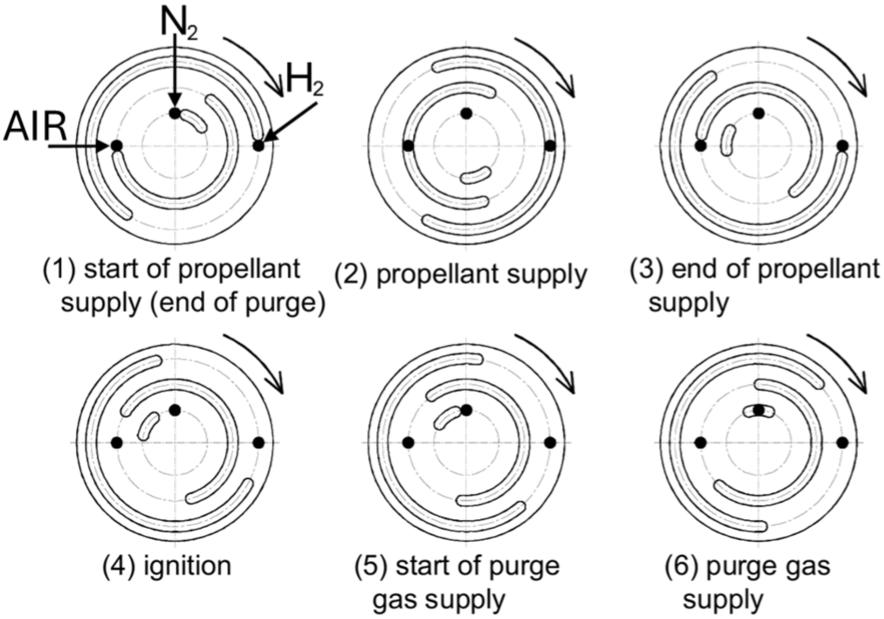

Figure 31: Positions of the rotary disk during various phases of the PDE cycle as viewed from the top cover side [25]

Figure 31 illustrates the positions of the rotary disk during the different phases of the PDE cycle. When the rotor valve is open (i.e., the combustor entrance is open), air is allowed to enter and fuel is injected. The fuel mixes with the air as it passes through the combustor entrance. When the rotor valve closes, the fuel/air mixture is injected. The spark igniter is then activated, leading to detonation and blowdown before the rotor reopens to initiate the next cycle. The rotary disk is positioned within the space between the top cover and the casing, and external torque is applied via the rotating shaft attached to the disk. The top cover and casing contain holes, shown as black dots in Figure 31, which serve as the supply and exhaust ports for propellant and purge gas, respectively.

Gas leakage highlights the importance of effective sealing strategies: teflon rings are to be installed at the sliding interfaces for sealing (surfaces of the rotary disk) and lubricated with silicon oil.

The rotary valve is actuated by an electromagnetic motor. The selected model is the Tamagawa Seiki TS4613, provided by Tamagawa Europe GmbH® (Germany), as shown in Figure 32. It is priced at €1050. This high-voltage model (AC 200V) has a power consumption of 600 W [26]. The rated torque of 1.91 Nm is well-suited to this application, where the expected torque demand lies between 0.34 and 0.45 Nm. Additionally, the motor's nominal speed of 3000 rpm enables an operating frequency exceeding 200 Hz.

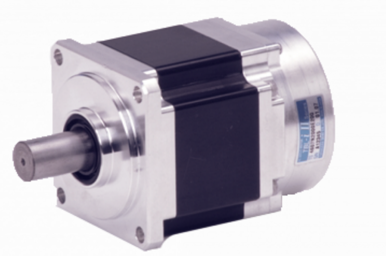

Figure 32: Tamagawa Europe GmbH® electromagnetic motor Seiki TS4613 [26]

Commercially available rotary valves are not suitable for this application, and thus a custom-designed solution is required. The motor must be mounted coaxially with the valve shaft to ensure proper alignment and performance.
A flexible coupling is required between the motor and the shaft to absorb dynamic loads and ensure mechanical integrity during operation. The selected coupling must be capable of withstanding the motor's rotational speed (i.e, 3000 rpm [26]). The proposed solution is the BoWex-ELASTIC® highly flexible flange coupling [51]. It is priced at €169.
The rotary valve, as shown in Figure 30, is custom-built and requires several aluminum alloy components: the top cover, rotating disk, casing and shaft. Aluminum alloy A7075 has been selected due to its exceptional mechanical properties and widespread use in high-performance applications. The estimated total cost for the aluminum material and, more significantly, the machining of these components is approximately €600.
For sealing, Polytetrafluoroethylene (PTFE) O-rings (model OR-13X2-PTFE) are selected from Rollakin® (France) [52]. PTFE sealing material is considered thermally stable and retains its mechanical properties within a temperature range of -200°C to +260°C. The cost is €1,8 per unit.

Spark igniter and fuel injection timing are accomplished via a custom LabVIEW® routine which monitors the rotor position, or alternatively via MATLAB®. A digital input/output board (selected in Section 2.5.6) receives input from an inductive proximity sensor, mounted in the rotor housing, to determine the rotor position. The selected proximity sensor is the Omron® TL-Q5MC1-Z inductive proximity sensor (Europe division) [53]. The sensor is priced at €29,65. The TL-Q5MC1-Z operates based on the inductive effect, detecting the presence of metallic or ferromagnetic materials to activate an output signal. It is employed to detect a specific rotor position, thereby synchronizing ignition timing with the rotary valve. This allows for precise control of the ignition phase, enabling repeatable experimental conditions. When the sensor detects the trigger (i.e., the correct rotor position), it sends a digital signal to the ignition system, which then actuates the spark plug.
A schematic representation of the test apparatus is provided in Figure 33, showing the rotary valve integrated into the PDE configuration.

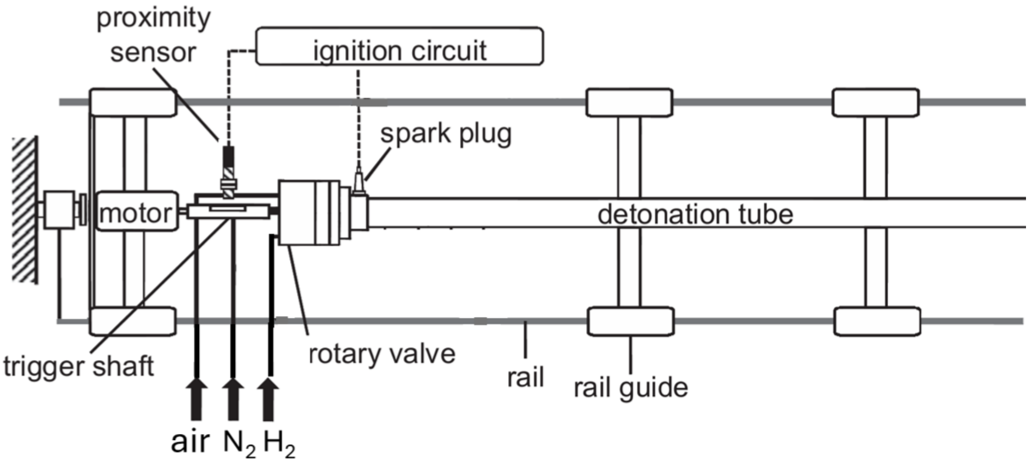

Figure 33: Schematic diagram of the PDE test setup (top view) [27]

Regarding compatibility with an RDE, the rotary valve design is transferable. In typical RDE setups, ignition is initiated via a predetonator (a short detonation tube). As shown in Figure 22, the same valve can be employed in this role, benefiting from the initial testing and development conducted using the PDE configuration. This modularity is advantageous: by first validating the rotary valve's operation in a PDE, it can later serve as the predetonator in an RDE. This staged approach enables better experimental control and understanding through step-by-step subsystem validation.

**One way valves** For safety purposes, one-way valves (check valves) are installed on all gas lines. These components allow fluid (air or fuel mixture) to flow in only one direction, thereby preventing any backflow.
The selected model is the AKM2000-F01-A SMC Pneumatic® Check Valve (Europe division), as shown in Figure 34.

Figure 34: AKM2000-F01-A SMC Pneumatic® Check Valve [28]

- Main body: made of PBT (polybutylene terephthalate), a high-performance plastic known for its mechanical strength and chemical resistance;
- Seals: while Nitrile Butadiene Rubber (NBR) seals are standard, for high-temperature or chemically aggressive environments, it is advisable to use FKM (Viton) or PTFE seals.

The selected seal manufacturer is Rehm Dichtungen Ehlers GmbH® (Germany), which offers PTFE gaskets that can be custom-made to match the dimensions of the valve. For this purpose, the CAD model provided by the manufacturer is essential [28]. The current cost of the valve is €21,82.
All three gas lines are equipped with check valves. It is recommended to install a one-way valve on each supply line, positioned immediately upstream of the injectors, as shown in the final schematic (Figure 38). This configuration ensures that, in the event of flashback or pressure fluctuations, reverse flow cannot reach the supply sources. The number of check valves is independent of the PDE tube length, as there are always three, corresponding to the three fluid lines.
This installation strategy remains valid for RDE configurations as well, with no change in valve positioning compared to the PDE case.

**Flame arrestors** For safety purposes, flashback arrestors, like check valves, are installed on each of the three gas lines. While check valves are designed to prevent reverse gas flow, they are not always sufficient to stop flame propagation or withstand shock waves resulting from a flashback. Therefore, flashback arrestors are employed as an additional and more robust safety measure. A flame arrestor is a device that allows gas to flow in the intended direction while preventing flame transmission through the pipeline. Its primary function is to halt flashbacks, which are sudden reverse flame fronts that can travel back toward the gas supply. This is especially critical when using hydrogen, which has an exceptionally high flame propagation speed and a wide flammability range, as demonstrated in Section 1.9 using the NASA CEA code.

The flashback arrestor selected for this experiment is the F100N-ES model, manufactured by WITT-Gasetechnik GmbH & Co. KG® (Germany), as shown in Figure 35.

Figure 35: Flashback Arrestor F100N-ES, WITT-Gasetechnik GmbH & Co. KG® [29]

This device is suitable for hydrogen and air at pressures up to 17 bar and is constructed from stainless steel. It incorporates three integrated safety components, as detailed in Figure 36:

1. gas non-return valve (1): prevents the backflow of gas. In the event of reverse flow, the spring-loaded non return valve (2) activates immediately, stopping the return flow and preventing the formation of an explosive mixture;
2. flame arrestor element (3): in the event of a flashback, the flame is instantly extinguished by a chrome-nickel steel cylinder. The porous structure dissipates the flame's energy, cooling it and stopping it in a fraction of a second;
3. temperature-sensitive cut-off valve (4): protects against flashbacks. If internal temperatures rise to dangerous levels, the integrated plastic component melts, triggering the spring-loaded valve that halts the gas flow before ignition conditions can develop at the gas inlet.

An alarm indicator (5) is also included to alert the user if a flashback occurs, allowing for prompt intervention and system reconfiguration.

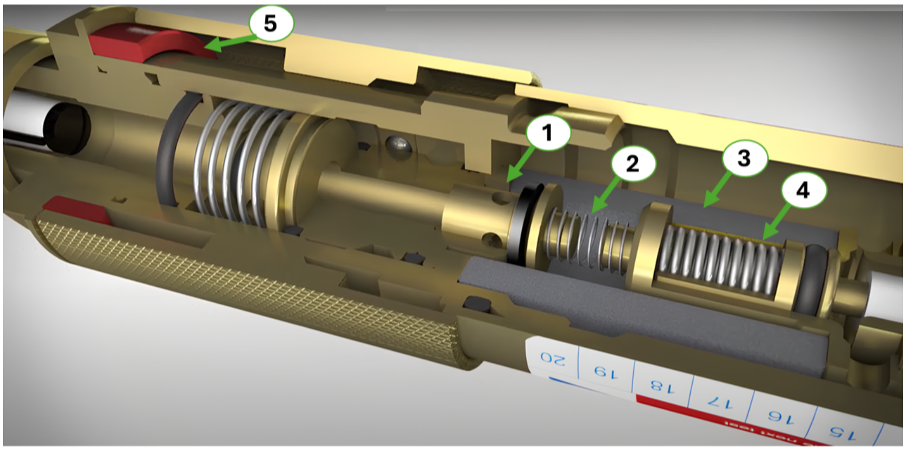

Figure 36: Components of Flashback Arrestor F100N-ES, WITT-Gasetechnik GmbH & Co. KG® [29]

In this setup, each flashback arrestor is mounted downstream of the check valve, and immediately upstream of the injector, as illustrated in Figure 38. This location ensures

that in the event of a flashback, the flame is stopped before reaching the fuel supply, thus protecting the tanks from explosion. Since it is placed before the detonation chamber, the operating pressure limit of 17 bar is more than sufficient for the expected conditions.
At present, a valve diameter of 48 mm has been selected, as specified in the datasheet [29]. However, if future system requirements demand larger diameters, WITT® offers a wide range of flashback arrestors with similar functionality and price range. Each flashback arrestor of this type is priced at €1775.
As with check valves, the number of flashback arrestors is fixed at three, corresponding to the three gas supply lines, and is independent of the PDE tube length. Furthermore, these devices are also used in RDEs for the same purpose and in the same configuration.

**Flow nozzles** Critical flow nozzles regulate the fuel and oxidizer flow rates, ensuring a stable and controlled flow: a repeatable and regulated flow is required to enable consistent comparisons between tests. They guarantee that the engine receives the correct mixture for efficient detonation. It is also necessary to avoid flow instability.
Since hydrogen is very light and sensitive to flow variations, using a critical flow nozzle can help prevent unwanted changes in the mixture. Additionally, critical flow nozzles, which can determine flow rates based solely on the nozzle exit pressure, are effective provided the supply pressures and temperatures are known. While confirming the flow meter measurements with thermocouples and pressure sensors is useful, it is not strictly necessary.
The selected flow nozzle is the ISA 1932 model, produced by KROHNE® (Germany), as shown in Figure 37.

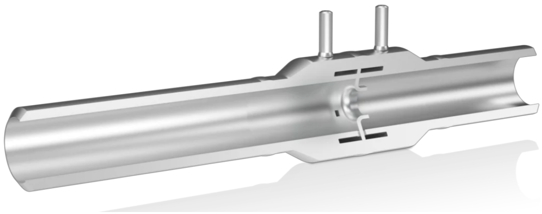

Figure 37: ISA 1932 nozzle KROHNE® [30]

This nozzle is suitable for applications involving hydrogen and air under high velocity and pressure conditions. Similar to flashback arrestors, the company offers different sizes of flow nozzles, with comparable prices and features. As the nozzle size has not yet been finalized, this model is indicative, with the final configuration expected to share similar features, even if the size changes. This nozzle is suitable for applications requiring high accuracy.
The nozzle is positioned between the check valve and the flame arrestor, as shown in Figure 38. It is priced at approximately €2000.
Similar to check valves and flashback arrestors, the number of flow nozzles is fixed at three, corresponding to the three gas supply lines. This configuration remains unchanged regardless of the length of the PDE tube. Additionally, these devices are also employed in RDEs for the same purpose and in the same setup.

In conclusion, to better illustrate the arrangement of the components within the fuel/oxidizer system, the schematic shown in Figure 38 is provided.

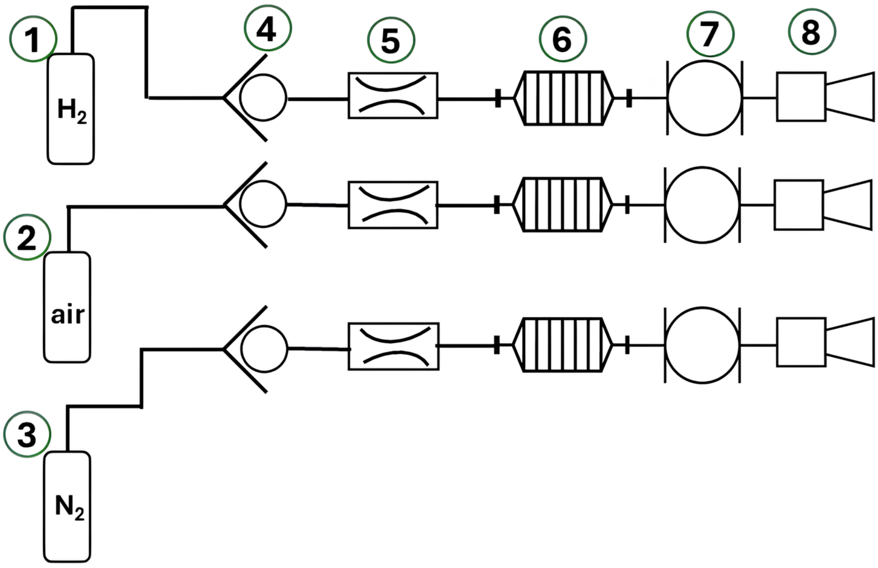

Figure 38: Schematic diagram of the fuel/oxidizer system. 1) Hydrogen tank; 2) Air tank; 3) Nitrogen tank; 4) Check valves; 5) Critical flow nozzles; 6) Flame arrestors; 7) Rotary valve; 8) Injectors

It should be noted that the flow meters, although present in the system, are not depicted in Figure 38. This is because the figure is intended to illustrate only the components of the fuel/oxidizer supply system, excluding instrumentation elements. The complete system, including all sensors and instrumentation, is presented later in Figure 48 in Section 2.7.

### 2.5.4 Ignition and control

**Spark Plug** The choice of ignition energy is crucial because the energy imparted by the spark significantly impacts the process of DDT. Inside the detonation chamber, a spark plug ignites the mixture, generating a combustion wave. The intensity of the spark is determined during the experimental campaign by adjusting the firing energy to produce a detonation wave that closely aligns with Chapman–Jouguet conditions. These conditions are easily calculated using the CEA code, as discussed in Section 1.9. However, based on previous experiments, it is known that the energy required to initiate the detonation of a hydrogen-air mixture is approximately between 50 and 150 mJ.

The position of the spark plug is shown in Figure 33: it is placed before the Schelkin spiral and after the injectors. The ignition system employed in this PDE setup consists of an automotive ignition control module and coil set, capable of delivering up to 150 mJ per spark. Ignition timing is controlled by a TTL signal generated by the proximity sensor, as described in Section 2.5.3. Specifically, the signal from the proximity sensor is sent to the DAQ system, which is discussed in Section 2.5.6. This TTL signal determines the precise moment of the spark, enabling precise synchronization between the propellant injection and ignition.
An ordinary automobile spark plug is used to initiate combustion: the Bosch® FR8DPX spark plug (Germany), as shown in Figure 39.

Figure 39: FR8DPX Spark Plug, Bosch® [31]

This spark plug features double iridium electrodes, providing enhanced durability and consistent ignition performance [31]. It is engineered for high-performance engines and is well-suited for applications requiring reliable ignition under demanding conditions, as in this case. The cost of the model is €6,15.

The ignition coil plays a critical role in the ignition system by transforming low battery voltage (12 V) into the high voltage required to generate a spark across the electrodes of the spark plug. This high-voltage discharge is essential for initiating combustion of the hydrogen-air mixture within the detonation tube. The ignition coil chosen for this application is the Beru® ZSE150 Ignition Coil (Germany) [54]. Its technical characteristics and compatibility with high-frequency operation make it an excellent candidate for use in the current experimental ignition system. The Beru® ZSE150 ignition coil is particularly suitable for this setup due to its compact design, making it ideal for integration into experimental configurations such as PDEs and RDEs. It is designed to deliver high-energy sparks, with reported ignition energies of approximately 150 mJ, which is ideal for hydrogen ignition. Additionally, when paired with an appropriate ignition control module, the coil can be triggered by a TTL signal, allowing precise timing control in synchronization with other system components such as proximity sensor and rotary valve. The cost of the coil is €201,59.
The programmable timing controller is managed using LabVIEW® software (or MATLAB®), which allows precise and repeatable control of the various valves and spark plug, as well as a centralized data acquisition system.
The number of ignition units used is independent of the length of the detonation tube; it remains constant at one.

Regarding the versatility of the setup for RDE configurations, the same system and control setup can be used. This is because the predetonator in an RDE essentially functions as a PDE, as explained earlier.

**Emergency shutoff button** The emergency shutoff button is a safety feature designed to disable the test cell by closing all supply gas valves and interrupting fuel injection and ignition trigger signals in the event of overpressure, early detonation, or fuel leakage. The button prevents the escalation of mechanical or thermal errors. If the system freezes or LabVIEW® crashes, the emergency shutoff button operates independently of the software.
There is a physical connection between the button and:

- valve power supply;

  - ignition system (spark plug).

Two relays are employed, one for the spark coil and another for the rotary valve: they interrupt the high-current power supply used. Pressing the emergency stop button opens the circuit, deactivates the relay and closes all critical lines. These electrical relay switches control power within the rig for engine control and instrumentation. When this switch is activated, power is cut off to these components, meaning fuel cannot be injected, the spark plug cannot fire and the tube is vented to the atmosphere. This ensures that operators can safely enter the laboratory without risk of ignition. The selected models are:

1. Siemens® 3SB3500-0AA12 Switch Access Round Actuator Push Button Switch (Germany) [55]. The cost is €22,22;
2. Omron Electronics Inc® G2R-1-E DC12 Relay 12VDC (Europe division) [56]. This relay is compatible with the igniter coil, as indicated by the voltage [54]. The cost is €6,61;
3. Finder® Relay 220V AC Serie 40.52 (Italy) [57]. This relay is compatible with the rotary valve since it operates at 220V AC (from datasheet of the rotary valve [26]). The cost is €7,29;
4. Mean Well® Power Supply 12VDC PSU 12V 2A (Europe division) [58]. This power supply is used to power the 12V relay controlling the spark coil. The cost is €25,73.

The cost of these components is fixed, regardless of the length of the PDE tube. Moreover, the same configuration can be adopted for an RDE.

### 2.5.5 Detonation Enhancement: Shchelkin Spiral

Currently, there are several conceptual approaches to achieving detonations in PDE systems, which can be broadly categorized into two types:

1. high-energy sources, such as arc discharges, lasers, or explosives, are used to directly detonate the fuel-oxidizer mixture. These methods aim to induce detonation rapidly but are inefficient, and the associated circuitry is often heavy and bulky;
2. low-energy ignition sources are combined with DDT-enhancing mechanisms, such as spirals, grooves or other obstacles along the deflagration path. Previous studies have shown that Shchelkin spirals are effective in promoting DDT, thus reducing the required length of the PDE tube.

Among various DDT enhancement devices, Shchelkin spirals have shown superior performance, followed by groove configurations and convergent-divergent throat designs.
Consequently, the Shchelkin spiral is the most widely used obstacle, designed to create eddies that facilitate flame acceleration while offering minimal resistance to the moving fuel/air/exhaust mixture. These eddies cause the flame to separate into multiple fronts, some of which move backward, collide with others and accelerate the fronts ahead of them. The behaviour of the spiral is difficult to model and predict, and research into this phenomenon is ongoing.
A key parameter for the Shchelkin spiral is the blockage ratio (BR), which is the ratio

of the area occupied by the spiral to the total internal area of the detonation tube. Additionally, Shchelkin spirals lead to blockage within the detonation tube, which can cause significant thrust losses if the spiral size is not properly selected. The spiral coils should be large enough to promote successful DDT while minimizing blockage within the detonation tube. In general, increasing the BR positively impacts the DDT phenomenon.

There is a challenge with damage to the spirals during long firing periods: the spirals could melt or disintegrate, leading to the spirals being expelled from the detonation tube and replacing the spirals after each test, making long-duration testing problematic. Therefore, the material selection for the spirals must ensure they can withstand the harsh conditions of the PDE environment, and practical systems may require cooling mechanisms for the spirals.

In conclusion, Shchelkin spirals are chosen as the preferred DDT enhancement mechanism due to their ability to avoid the heavy and bulky systems associated with high-energy ignition sources.

Figure 40: Stainless Steel Shchelkin Spiral

This spiral is installed at the beginning of the PDE tube to initiate the DDT from the outset. It is typically made of stainless steel to withstand the harsh conditions within the PDE. The price of the Shchelkin spiral is determined once the dimensions of the detonation tube are analysed, allowing for an accurate estimate of the amount of bulk material required for its fabrication. The spirals can be easily manufactured by spring manufacturers at a low cost. For instance, the company DIM® (Europe division) offers a wide range of stainless steel spirals at competitive prices.

### 2.5.6 Data acquisition system

As stated in the datasheets, the operating frequency of the pressure transducers is 2.6 kHz [10]. According to the Nyquist–Shannon sampling theorem, the acquisition frequency must be at least twice this value. However, literature from previous experimental campaigns indicates that increasing the data acquisition (DAQ) sampling frequency to values greater than 1 MS/s is beneficial for avoiding data integrity issues during PDE firings [42]. Simultaneous sample-and-hold capability is essential to ensure synchronized data acquisition—critical for accurate shockwave synchronization and velocity calculations.

A LabVIEW®-based program (or MATLAB®) interfaces with a multi-channel DAQ system through a signal conditioning module. The signal conditioning for the load cell and thermocouples is already integrated within the amplifiers connected to these sensors. Additionally, the pressure transducers and the flow meters can be directly connected to the DAQ system without the need for a conditioning circuit, as explained in Section 2.5.2. Therefore, the only sensors requiring dedicated signal conditioning are:

- accelerometers: the selected model is the PCB® 480B21 (German division) [59]. This model can accommodate up to three accelerometers. The cost is €315;
- ion sensors: a custom conditioning circuit is required to convert the current signal into a measurable voltage for the DAQ system. This circuit should include a high-input impedance operational amplifier, a low-pass filter to attenuate high frequencies and surge protection (TVS or clamping Zener diodes). One conditioning circuit is required per sensor (total: two circuits). The operational amplifier selected is the OPA627AP from Texas Instruments® [60]. The cost of the OPA627AP is €34,44. The estimated cost of the entire conditioning circuit per ion sensor is €100.

Thus, the cost of the signal conditioners remains constant regardless of the setup size, as the number of accelerometers and ion sensors is fixed.

The DAQ communicates with a remote PC (running LabVIEW® or MATLAB®) via an MXI-4 fiber optic cable, which ensures robust EMI shielding and enables real-time monitoring and control from the safety of the control room.

For system control—especially the actuation of gas injectors—digital TTL high-low signals generated by the DAQ are routed to the injector driver module. These signals control the opening and closing of injectors, with necessary delays incorporated into the control routine to accommodate the dynamic response of system components.

To achieve the required performance, a National Instruments® PXI-based system (USA) is used. It integrates control and acquisition via LabVIEW® and supports precise timing and synchronization. The selected components include:

1. DAQ card: National Instruments® PXIe-6133 [61].
    - Type: simultaneous sample-and-hold;
    - Channels: 8 analog input channels;
    - Resolution: 16-bit (chosen for higher precision over 14-bit alternatives);
    - Sampling Rate: 2.5 MS/s per channel, exceeding the minimum required by the Shannon theorem;
    - Interface: PXI backplane, LabVIEW®-compatible;
    - Connection Box: each PXIe-6133 is paired with an 8-channel BNC-2110 interface box via coaxial cables;
    - Data Handling: supports double buffering, a crucial technique for high-speed acquisition to avoid data loss during transfer. While Buffer A acquires real-time data, Buffer B transfers previously acquired data to the PC. This enables continuous acquisition, especially for transient signals such as those in PDE testing;
    - Cost: €3168,68.
2. Controller: the selected model is the National Instruments® PXIe-8840 [62].
    - Manages PXIe-6133 DAQ cards;

  - Synchronizes acquisition clocks across devices;
  - Handles data transfer and real-time display;
  - Specifications: 2.3 GHz bandwidth; integrated system controller for real-time or Windows-based operation;
  - Cost: €6251,44.

3. Chassis: the selected model is the National Instruments® PXIe-1062Q [63].
   - Slots: 8;
   - Function: houses multiple PXIe-6133 cards;
   - Communication: connected to the remote PC via a 200 m MXI-4 fiber optic cable, ensuring EMI immunity;
   - Cost: €9121.
4. Digital I/O (TTL Control): the selected model is the NI 9401 [64].
   - Function: generates TTL signals to control valves and ignition;
   - Cost: €556;
   - Usage: TTL channels are utilized for controlling purge nitrogen, fuel-air injection and ignition. Each control signal is managed by a dedicated counter channel. A representative TTL waveform for three such channels—purge nitrogen, fuel-air filling, and ignition—is illustrated in Figure 41.

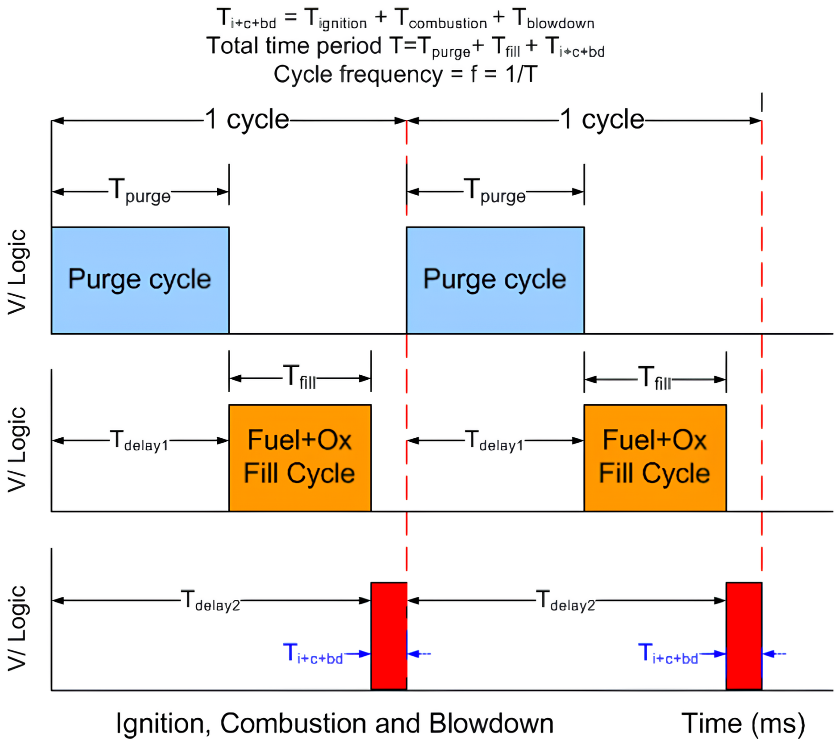

Figure 41: A typical TTL output from the PDE control program [32]

As shown in Figure 41, the rise/fall times of the TTL is negligible compared to the response time of the valves and the TTL signals may be assumed to be perfectly rectangular for all practical purposes.

5. Communication Cable: National Instruments® 781402-200 (MXI-Express Fiber Optic Cable, Gen 1 x4) [65].
    - Length: 200 m;
    - Purpose: remote chassis control and EMI-shielded data transfer;
    - Cost: €2040.

To summarize, the measured analog signals from the sensors are conditioned and digitized by a PXIe-6133-based DAQ system housed in a PXIe-1062Q chassis. Control and acquisition tasks are managed by a PXIe-8840 controller. The system ensures synchronized, high-speed data acquisition and real-time control through TTL signals. Post-processing is conducted using MATLAB®.

The number of required components depends on the length of the detonation tube, as this directly influences the number of sensors needed. Consequently, this determines whether more than one DAQ card is necessary, which would in turn increase the overall system cost. It is worth noting that these components are equally suitable for an RDE configuration; therefore, no modifications are required if the experimental setup is adapted for RDE testing.

### 2.5.7 Cooling system

For hydrogen-air mixtures, the need for effective cooling is particularly critical due to the extremely high temperatures reached during detonation. In the CEA results (Table 3), the temperature ratio $T_2/T_1 = 9.8$, meaning that for a stoichiometric mixture starting at 300 K, the detonation temperature reaches approximately 2940 K. Such conditions demand a robust thermal management strategy to protect critical components of the PDE, including the combustion chamber, valves, sensors and diagnostic instruments, and to extend operational time.

Active external water cooling is selected for the experimental setup. Compared to internal film cooling, water cooling is more efficient, easier to implement for long-duration tests and does not interfere with the flow dynamics, making it ideal for precise flow characterization. In contrast, film cooling introduces flow disturbances due to the interaction between the detonation wave and the cooling film, including risks of reverse flow within the cooling holes. While film cooling is more compact and lighter, its disruptive nature renders it less suitable for fundamental studies. However, it remains a promising solution for future applications and could be integrated into an RDE setup, once the PDE testing is complete.

Given the high thermal loads, especially in hydrogen-air detonations, a dual-cooling strategy may be necessary:

1. external active water cooling: for complete structural coverage, spiral and critical zone cooling, and sensor/spark plug housing protection;
2. internal film cooling: to locally shield the inner wall, reduce direct thermal exchange with hot gases, and prevent premature ignition from wall heating.

The final cooling strategy should be defined based on results from CFD simulations conducted during the experimental phase.

The water cooling system follows an open-loop configuration, where fresh cool water is continuously fed into the cooling channels and the heated water is discharged directly to the drain, eliminating the need for heat exchangers. This configuration is shown in Figure 42. Water cooling has been the predominant approach in prior PDE experiments. It is implemented using copper tubing (6–10 mm in diameter) brazed onto the combustion tube and spiral regions, and flattened to enhance thermal contact. Copper is chosen for its high thermal conductivity, ease of fabrication, corrosion resistance and affordability. A 2-meter copper tube typically costs less than €14, making the system economical.

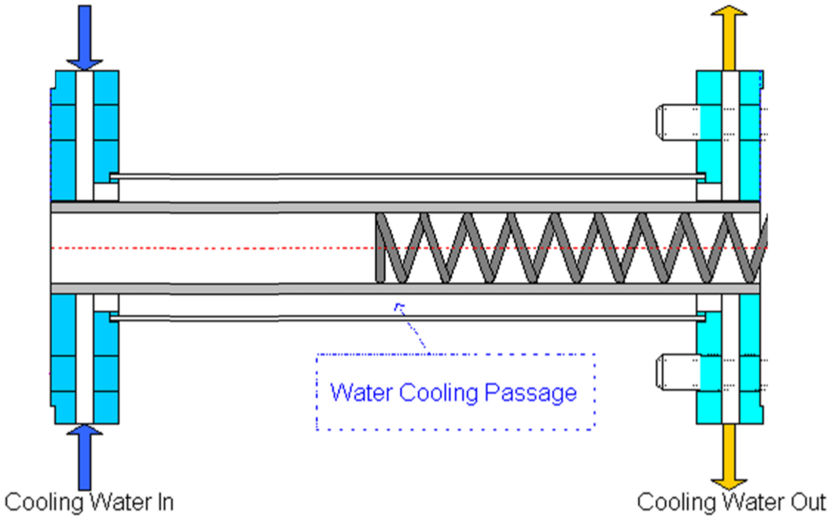

Figure 42: Schematic representation of the external water-cooling system for the detonation tube in an open-loop configuration [33]

In addition to tubing, several key components are required:

1. High-pressure water pump: a GRUNDFOS ® España CR 5-10 model pump (Spain) is selected, capable of delivering flow rates at approximately 50 ft/s, which is optimal for convective heat transfer [66]. The cost is €2916.
2. Cold water supply tank: a non-recirculating tank provides a continuous supply of cool water. A specific model is not selected, as such tanks are widely available and can also be sourced from within the university facilities.
3. Flow control and safety valve: electric ball valve DN50 PN40 A251 HPControl® is used to enable both automation and safety [67]. This valve allows for:
    - selective cooling of specific zones (e.g., spiral, sensors). Independent zone management is essential, as the system can be divided into distinct cooling areas. For instance, the combustion tube section housing the Shchelkin spiral requires a higher cooling water flow rate due to elevated temperatures and pressures;
    - emergency shut-off during anomalies, and activation only during testing to prevent unnecessary water consumption.

    The selected model costs €267,56.
4. Cooling for pressure transducers: when selecting pressure sensors for PDE applications, thermal resistance and signal stability under prolonged exposure to high temperatures are critical factors. Among available technologies, piezoresistive

transducers are significantly less susceptible to thermal shock compared to piezoelectric transducers, making them a more suitable choice for environments with sustained high thermal loads. To mitigate thermal stress, pressure transducers are installed within custom-designed water-cooled jackets, which create a localized stable thermal environment. These jackets enable sensor operation even when the surrounding gas temperatures exceed the transducer's rated range. They are manufactured from high-strength stainless steel, which ensures structural integrity, corrosion resistance and effective heat transfer. Even if the detonation tube's outer wall is actively cooled, these jackets remain essential due to the high internal gas temperatures and the critical importance of maintaining optimal sensor function. These jackets have to be produced by collaborating with a specialized machining workshop, since the manufacturer of the pressure transducers, as well as other similar suppliers, does not offer this type of accessory.
The water jackets are integrated into the overall open-loop cooling system, which eliminates the need for heat exchangers. Cold water flows directly through the jackets and is discharged after absorbing heat. This configuration is simple to implement, cost-effective and easy to maintain, especially in laboratory test environments. Additionally, this setup is more effective than ceramic coatings or recessed mounting. A typical jacket is illustrated in Figure 43.

Figure 43: Example of a water jacket for a pressure transducer

The jacket in the image is transparent for illustrative purposes only, in order to show the presence of water inside. In the actual setup, the jacket is made of stainless steel.

5. Spark plug and ion sensor: since automotive spark plugs like the FR8DPX are not designed for PDE environments, they are protected with custom water-cooled adapters. This prevents premature ignition and avoids thermal failure of the spark plug insulation. At this stage, the FR8DPX spark plug is considered; however, since the ion sensor employs a structurally similar plug, the analysis remains equally applicable to both cases. The water-cooled adapter consists of a threaded adapter made of stainless steel, compatible with the M14x1.25 thread of the FR8DPX plug. A surrounding chamber is then constructed to allow water to circulate around the body of the spark plug, as shown in Figure 44. Two fittings for 6–8 mm tubing (inlet/outlet) are integrated into the design, enabling water flow through the jacket, clearly visible in the Figure 44. Only the electrode should be exposed to the internal flow, while the rest of the spark plug body is actively cooled. 304 stainless steel is recommended for structural components due to its corrosion resistance and strength, with Viton seals or high-integrity O-rings to ensure leak-proof assembly. A water pressure between 2 and 5 bar is typically

sufficient, even for open-loop cooling systems.

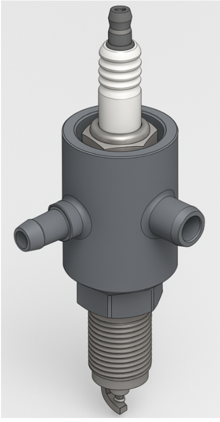

Figure 44: Illustration of custom water jacket for the FR8DPX spark plug

Typical operating parameters are as follows:

- flow rate: 1-2 L/min;
- inlet water temperature: 15-25°C;
- operating pressure: 2-5 bar.

These values provide an effective balance between cooling performance and system simplicity.

Other sensors—such as flow meters, load cell and accelerometers—are not considered here, as they are not positioned along the detonation tube and therefore are not subject to the same thermal loads. Additionally, active cooling is not required for certain devices like thermocouples, as discussed in their dedicated paragraph in Section 2.5.2.

6. Injector cooling: injectors are shielded from thermal stress using water-cooled housings with integrated safety features such as check valves. A schematic is shown in Figure 45. The system is cost-effective and easy to implement. In particular, the cost associated with water cooling for the injectors, spark plug and pressure transducers is not considered, as these basic components are either readily available within the university or can be easily purchased at low cost from any store selling standard mechanical parts.
   For safety purposes, a check valve is also integrated into the system. It was not previously discussed as its selection is primarily driven by compatibility with the cooling system used for the injector measurements. The chosen model is the Parker® 8M-C8L check valve (USA) [68]. This component is priced at €356.

7. Shchelkin spiral cooling: the Shchelkin spiral is the hottest region of the combustion tube, and its cooling is of utmost importance. Without adequate cooling, it can lead to pre-ignition, ablation and even mechanical failure. Specifically, pre-ignition causes fuel and oxidizer wastage, loss of thrust, unwanted vibrations and possible damage to valves and other components. Extreme thermal and pressure conditions within the PDE can cause severe degradation of the Shchelkin spiral. High temperatures weaken the metal structure, while intense pressure compresses the helix. In some cases, this leads to partial melting or fusion of the coils.

In more severe scenarios, the spiral may disintegrate and be expelled at high velocity from the detonation tube. The water cooling setup for the spiral is depicted in Figure 46.

The cost of the cooling system is influenced by the length of the detonation tube. However this dependency concerns only the length of the copper tube used for cooling. Given the relatively low price of copper tubing, its impact on the overall cost remains negligible.

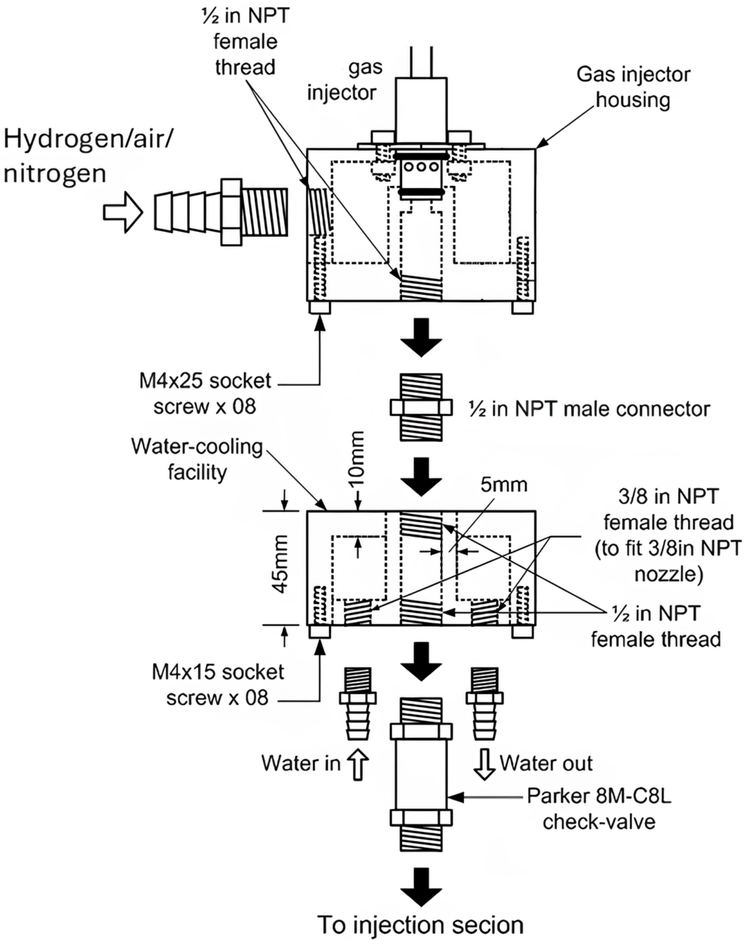

Figure 45: Gas injector housing with integrated water cooling and safety check valve [34]

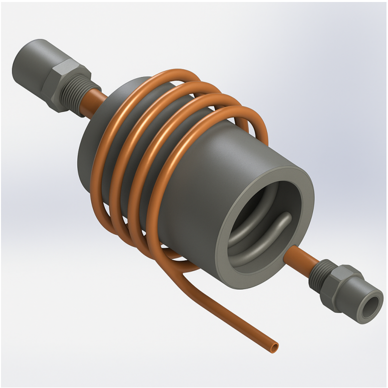

Figure 46: Water cooling arrangement for the Shchelkin spiral, showing inlet (left) and outlet (right)

When transitioning the experimental setup to an RDE, additional thermal management measures become necessary to ensure prolonged operation of the test model. In this proposed configuration, a water jacket is integrated around the outer wall of the combustion chamber, complementing the previously described cooling setup for the pre-detonator (which functions as a PDE tube, see Figure 22). As discussed in Section 1.10, the inner wall of an RDE is subject to a significantly higher heat flux than that of a PDE, making enhanced cooling essential.

The physical model comprises an annular combustion chamber, a surrounding coolant channel, and a single row of six film cooling holes, each with carefully defined dimensions and an inclination angle of 30°, as illustrated in Figure 47.

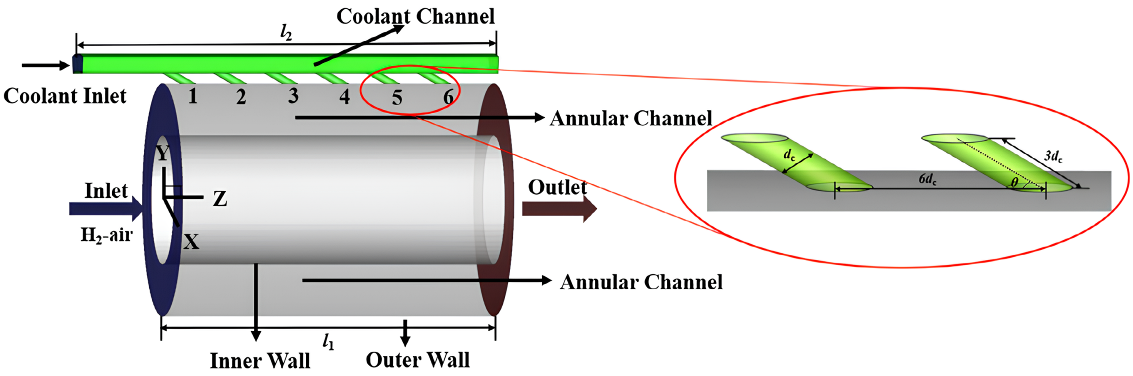

Figure 47: Schematic diagram of film cooling in an RDE [35]

In this context, even more critically than in PDEs, a thorough CFD study is essential to guide the design of the cooling holes. Additionally, the inherently unsteady nature of detonation in RDEs makes the dynamics of film cooling particularly complex.

### 2.5.8 Purge system

The purge process is implemented to fully expel the burned gases between cycles, preventing the premature ignition of the fresh fuel–oxidizer mixture. If not applied, residual combustion products may remain in the detonation tube after the exhaust phase. These remnants can lead to undesired pre-ignition of the incoming mixture, altering the initial conditions, such as the equivalence ratio, and potentially compromising detonation stability and performance. This principle has already been discussed in Chapter 1 (Section 1.4), which outlines the PDE operating cycle. Therefore, this must be taken into account when configuring the LabVIEW® program (or MATLAB®) for valve timing control.

At low operating frequencies (e.g., 10 Hz), the purge phase may not be required, since the exhaust gases have sufficient time to be cleared naturally. However, as the frequency increases, the residence time of the exhaust gases decreases, and purging becomes necessary. Moreover, the fraction of purge gas required typically increases with the frequency. It is important to note that the purge process does not contribute to thrust generation; on the contrary, it reduces engine efficiency by occupying time and space in the cycle. Nonetheless, this penalty may be acceptable at higher frequencies, where the thrust is inherently greater. The optimal purge gas fraction must be determined experimentally, ensuring that the additional purge mass flow does not significantly reduce the fuel-based specific impulse.

A practical criterion is to monitor whether deflagrative combustion appears during the later stages of operation, for example using ion sensors. If this occurs, it indicates incomplete purging.

In this experimental setup, nitrogen is used as the purge gas due to its inert properties, widespread availability and effectiveness in preventing pre-ignition. Like the fuel and oxidizer, it is injected through the rotary valve and cleans the detonation tube between cycles.
The required nitrogen pressure and mass flow rate must be tuned during the experimental campaign, as these parameters are highly dependent on the geometry, valve dynamics, and operating conditions of each specific setup. There are no general guidelines that can be applied across all cases. The entire purge process is automated via the DAQ system, which controls the rotary valve timing.
Although nitrogen is the preferred choice for its inert characteristics, air can also be used as a substitute, especially in later stages of development or for field-deployable systems, without requiring hardware changes. While air is less effective at inerting the detonation tube, it may be sufficient in cases where lower-frequency operation or reduced sensitivity to pre-ignition is acceptable.
Lastly, it is important to highlight that the purge process, together with the non-zero valve response time, introduces non-idealities that reduce the actual performance of the system when compared to the ideal predictions computed via chemical equilibrium analysis (CEA) in Chapter 1 (Section 1.9).
The purge strategy described here is equally valid for RDEs, as it employs the same control architecture and injection configuration.

## 2.6 Innovations

To summarize the innovations applied with respect to the majority of the previous experiments are briefly illustrated in Table 11.

| **Innovation Element** | **Description** | **Why It Is Innovative (Compared to Previous Experiments)** |
|---|---|---|
| Versatility with respect to RDEs | Use of piezoresistive and non-piezoelectric pressure transducers | These transducers are usually used in RDEs, not in PDEs |
| Ion sensors | Allow more precise measurements | Ion sensors are not typically used in hydrogen–air mixtures |
| Load cell without spring-damper configuration | Higher measurement accuracy, especially for single-cycle tests | Prior works used load cells with spring-damper setups |
| High-speed camera (NOVA S-Series) | Enhanced sensitivity, image quality and resolution | Previous setups employed the FASTCAM SA-5, which is inferior |
| Camera setup using BOS | BOS reduces costs and simplifies the setup | Earlier works used traditional Schlieren systems |
| Rotary valve | Enables higher frequency and larger mass flow rates | Most prior experiments used solenoid valves |

Table 11: Summary of innovations in the experimental setup

## 2.7 Cost

Figure 48 illustrates all the various components previously selected.

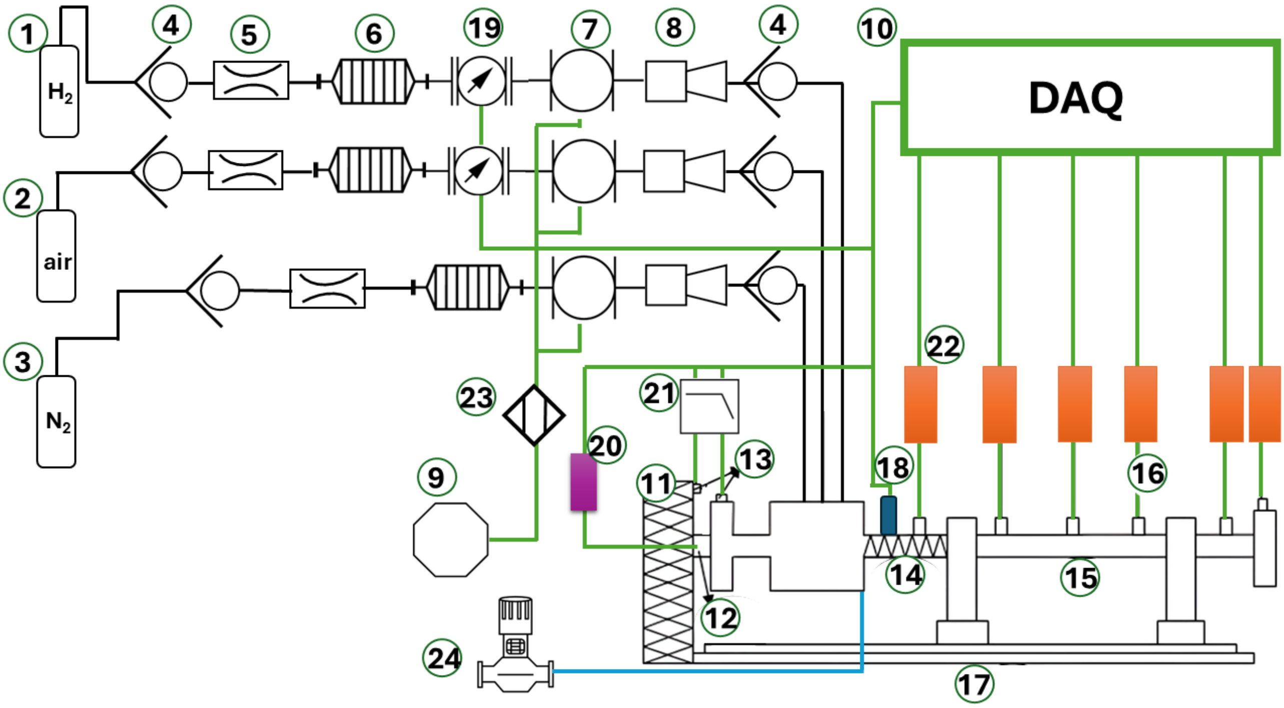

Figure 48: Schematic representation of the PDE setup. 1) Hydrogen Tank; 2) Air Tank; 3) Nitrogen Tank; 4) Check Valves; 5) Critical Flow Nozzles; 6) Flame Arrestors; 7) Rotary Valve; 8) Injectors; 9)TTL Control; 10) DAQ system; 11) Thrust Stand; 12) Load Cell; 13) Accelerometers; 14) Shchelkin Spiral; 15) PDE tube; 16) Pressure Transducers/Thermocouples; 17) Slide; 18) Ion Probes; 19) Flow Meters; 20) Amplifier For Load Cell; 21) Butterworth Low Pass Filter For Accelerometers; 22) Amplifier For Thermocouples; 23) Proximity Sensor; 24) Water Pump

For the sake of simplicity and clarity:

- the DAQ system is not depicted in full detail: the block labelled DAQ includes the conditioning modules for the accelerometers and ion probes, the DAQ cards, the controller and the chassis, as described in Section 2.5.6;
- only one ion sensor is shown; however, two are installed along the section with the spiral;
- wherever a pressure transducer is indicated, a thermocouple is also present in the same section;
- the external camera setup, positioned outside the detonation tube, is not shown. It is clearly illustrated in Figure 28, Section 2.5.2;
- the number of sensors depicted is indicative: the actual number depends on the final length of the detonation tube, which is analysed later.

To estimate the cost independently of the experimental setup's dimensions, the tables presented below are used. The total indicated in the last row of Table 14 refers solely to the combined price of components whose quantities do not depend on the number of units.

| **Component Name** | **Unit Price [€]** | **Length Dependent** | **Number of Units** | **Total Price [€]** |
|---|---|---|---|---|
| Structural bearings | 126,63 | No | 2 | 253,26 |
| Rail | Depends on dimension | Yes | 1 | TBD |
| Aluminum Plate | 55,70 | No | 2 | 111,4 |
| Detonation tube | Depends on dimensions | Yes | Depends on tube length-/thickness | TBD |
| Aluminum profile | 27,40 | No | 4 | 109,6 |
| Pressure Transducer | 163,54 | Yes | Depends on tube length | TBD |
| Thermocouples + M2 thread | 1195+80 | Yes | Depends on tube length | TBD |
| Epoxy Paste | 7,15 | Yes, but one unit is always sufficient | 1 | 7,15 |
| Amplifier for thermocouples | 2480 | Yes | Depends on tube length | TBD |
| Ion sensors | 6,68 | No | 2 | 13,36 |
| Oxidizer flow meter | 2592 | No | 1 | 2592 |
| Fuel flow meter | 4300 | No | 1 | 4300 |
| Load Cell | 2300 | No | 1 | 2300 |
| Amplifier for load cell | 5000 | No | 1 | 5000 |
| Accelerometers | 560 | No | 2 | 1120 |
| Filter for accelerometers | 9,62 | No | 2 | 19,24 |
| High speed camera | 40 000 | No | 1 | 40 000 |
| LED | 128,48 | No | 1 | 128,48 |
| Glass diffuser | 17,75 | No | 1 | 17,75 |

Table 12: Component cost breakdown

| **Component Name** | **Unit Price [€]** | **Length Dependent** | **Number of Units** | **Total Price [€]** |
|---|---|---|---|---|
| Nitrogen Tank | 111,32 | No | 1 | 111,32 |
| Air Tank | 550 | No | 1 | 550 |
| Hydrogen Tank | 1320 | No | 1 | 1320 |
| Injectors | 438,27 | No | 3 | 1314,81 |
| Rotary valve motor | 1050 | No | 1 | 1050 |
| Rotary valve material | 600 | No | 1 | 600 |
| Elastic coupling | 169 | No | 1 | 169 |
| O rings | 1,8 | No | 4 | 7,2 |
| Proximity sensor | 29,65 | No | 1 | 29,65 |
| One way valves | 21,82 | No | 3 | 65,46 |
| Flame arrestor | 1775 | No | 3 | 5325 |
| Flow nozzles | 2000 | No | 3 | 6000 |
| Spark plug | 6,15 | No | 1 | 6,15 |
| Ignition Coil | 201,59 | No | 1 | 201,59 |
| Push Button | 22,22 | No | 1 | 22,22 |
| Relay for coil | 6,61 | No | 1 | 6,61 |
| Relay for valve | 7,29 | No | 1 | 7,29 |
| Power supply for relay | 25,73 | No | 1 | 25,73 |
| Shchelkin Spiral | Depends on dimensions | Yes | 1 | TBD |
| Conditioners for accelerometers | 315 | No | 1 | 315 |
| Conditioners for ion sensors | 100 | No | 2 | 200 |
| DAQ card | 3168,68 | Yes | Depends on number of sensors | TBD |
| Controller | 6251,44 | No | 1 | 6251,44 |
| Chassis | 9121 | No | 1 | 9121 |
| Digital I/O | 556 | No | 1 | 556 |
| Communication Cable | 2040 | No | 1 | 2040 |

Table 13: Component cost breakdown

| Component Name | Unit Price [€] | Length Dependent | Number of Units | Total Price [€] |
|---|---|---|---|---|
| Copper tubing | 14/2m | Negligible | TBD | 14 |
| Water pump | 2916 | No | 1 | 2916 |
| Ball valve | 267,56 | No | 1 | 267,56 |
| Check valve for injector | 356 | No | 3 | 1068 |
|  |  |  | **Total** | **95533,27 €** |

Table 14: Component cost breakdown

## 2.8 Dimensions

Three different experimental setups are considered, listed in order of increasing physical dimensions:

1. Air Force Configuration: as described in Section 2.5.1, the PDE consists of a stainless-steel tube with a total length of 660 mm, an internal diameter of 48 mm, and a wall thickness of 6.35 mm;

2. Nanjing University of Aeronautics and Astronautics, China: the PDE has a total length of 155 cm and an inner diameter of 86 mm. Based on Equation (18), the required wall thickness is calculated as follows:

$$t = \frac{P_2 \times R}{\sigma_{\text{allow}}} \cdot \phi \times FS = \frac{18.04 \times 43}{792} \cdot 4 \times 3 = 11.75 \text{ mm} \tag{32}$$

3. Aoyama Gakuin University, Japan: the PDE tube is 5 meters long with an internal diameter of 100 mm. The wall thickness required in this case is:

$$t = \frac{P_2 \times R}{\sigma_{\text{allow}}} \cdot \phi \times FS = \frac{18.04 \times 50}{792} \cdot 4 \times 3 = 13.67 \text{ mm} \tag{33}$$

To estimate the cost associated with each configuration, the following considerations are made:

- instrumentation spacing: pressure transducers and thermocouples are assumed to be placed every 100 mm along the detonation tube, in accordance with literature [69]. However, for configurations exceeding 2 meters in length (e.g., the third setup), this spacing is increased to 250 mm to reduce overall cost. This adjustment is also supported by references in the literature [70]. Accordingly, the number of sensors is determined by dividing the tube length by 100 mm for the first two setups and by 250 mm for the third;

- Shchelkin spiral: reference values are taken from the Air Force setup, which is most similar to the configurations under consideration. The spiral consists of a 76.2 mm (3 in.) long steel spring coil with a diameter of 9.52 mm (3/8 in.) and a pitch of 6 turns per inch [71]. It provides a blockage ratio of 34%, sufficient to ensure consistent DDT without obstructing the tube. This spiral can be manufactured by DIM® (Italy) at a cost of €9,90.

To maintain similarity, the spiral dimensions are scaled accordingly for different configurations. For instance, in the second configuration, the spiral dimensions are:

  - length $l = 76.2/660 \cdot 1550 = 178.95$ mm;
  - diameter $d = 9.52/48 \cdot 86 = 17.06$ mm

with a pitch of 6 turns per inch maintained. This spiral can be manufactured by DIM® at a cost of €14,90.
Similarly, for the third configuration, the spiral dimensions are: length $l = 577.27$ mm and diameter $d = 19.83$ mm, also maintaining a pitch of 6 turns per inch. This spiral can be manufactured by DIM® at a cost of €14,90;

- tank cost: the cost of the propellant tank is assumed to be independent of the setup dimensions, as discussed in Section 2.5.3, since the selected size is adequate for all configurations;
- cooling cost: as explained in Section 2.5.7, the cost of cooling is considered dimension-independent, due to its relatively low impact and the use of a standard water pump, which is adequate for all configurations.

As shown in Tables 12, 13 and 14, the following factors contribute to increased cost as the physical size of the setup increases:

1. rail dimensions;
2. length and diameter of the detonation tube;
3. number of pressure transducers and thermocouples (proportional to tube length). As each thermocouple amplifier supports a maximum of 10 sensors (Section 2.5.2), additional amplifiers may be required;
4. size of the Shchelkin spiral;
5. number of DAQ cards: one DAQ card supports up to 8 sensors and must accommodate pressure transducers, thermocouples, one load cell, two accelerometers, two ion sensors and two flow meters. For example, in the Air Force configuration, the total number of sensors is:
    - 6 pressure transducers;
    - 6 thermocouples;
    - 1 load cell;
    - 2 accelerometers;
    - 2 ion sensors;
    - 2 flow meters,

   Total: 19 sensors; 3 DAQ cards required.

Therefore, three separate tables are presented for the configurations considered. Each table includes both the fixed costs (dimension-independent, evaluated in Table 14) and the variable costs related to setup size.

| **Component Name** | **Unit Price [€]** | **Number of Units** | **Total Price [€]** |
|---|---|---|---|
| Fixed cost | | | 95533,27 |
| Rail (SR20-800L) | 100,8 | 1 | 100,8 |
| Detonation tube | 120 | 1 | 120 |
| Pressure transducers | 163,54 | 6 | 981,24 |
| Thermocouples (+ M2 thread) | 1275 | 6 | 7650 |
| Amplifier for thermocouples | 2480 | 1 | 2480 |
| Shchelkin spiral | 9,90 | 1 | 9,90 |
| DAQ card | 3168,68 | 3 | 9506,04 |
| | | **Total** | **116381,25 €** |

Table 15: Total cost of the first configuration (Air Force)

| **Component Name** | **Unit Price [€]** | **Number of Units** | **Total Price [€]** |
|---|---|---|---|
| Fixed cost | | | 95533,27 |
| Rail (SR20-1500L) | 180,28 | 1 | 180,28 |
| Detonation tube | 627,75 | 1 | 627,75 |
| Pressure transducers | 163,54 | 15 | 2453,10 |
| Thermocouples (+ M2 thread) | 1275 | 15 | 19125 |
| Amplifier for thermocouples | 2480 | 2 | 4960 |
| Shchelkin spiral | 14,90 | 1 | 14,90 |
| DAQ card | 3168,68 | 5 | 15843,4 |
| | | **Total** | **138737,7 €** |

Table 16: Total cost of the second configuration (Nanjing University)

| **Component Name** | **Unit Price [€]** | **Number of Units** | **Total Price [€]** |
|---|---|---|---|
| Fixed cost | | | 95533,27 |
| Rail (SR20-5000L) | 577,65 | 1 | 577,65 |
| Detonation tube | 2475 | 1 | 2475 |
| Pressure transducers | 163,54 | 20 | 3270,8 |
| Thermocouples (+ M2 thread) | 1275 | 20 | 25500 |
| Amplifier for thermocouples | 2480 | 2 | 4960 |
| Shchelkin spiral | 14,90 | 1 | 14,90 |
| DAQ card | 3168,68 | 6 | 19012,08 |
| | | **Total** | **151343,7 €** |

Table 17: Total cost of the third configuration (Aoyama Gakuin University)

These three configurations are then used to construct a cost–dimension relationship, as shown in Figure 49. The dimensionless parameter $\lambda$ is defined as the length of the detonation tube divided by 1000 mm:

$$\lambda = \frac{L_{\text{tube}}}{1000\ \text{mm}} \tag{34}$$

This representation allows for interpolation and trend estimation across setups of varying scale.

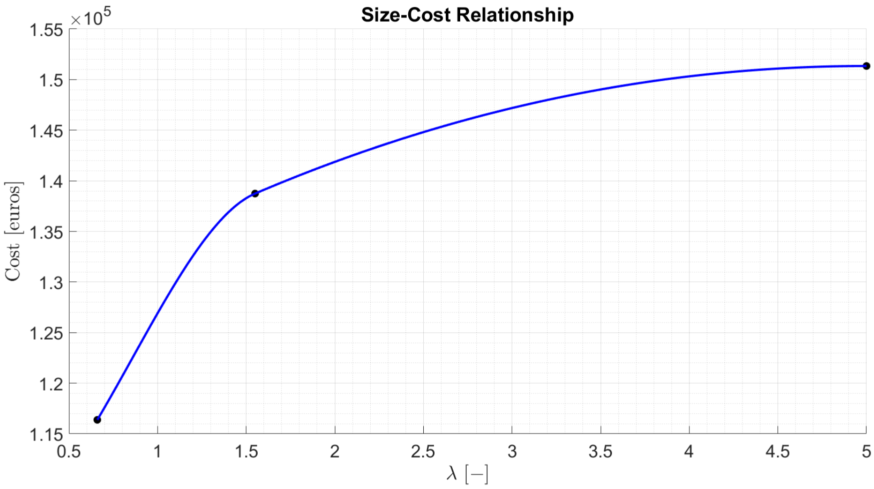

Figure 49: Plot of the cost of the experimental setup with respect to $\lambda = L/(1000mm)$

# Chapter 3

# 3 Numerical Simulation

The simulation of the experimental apparatus, using the components selected in Chapter 2, is performed in Simulink® to gain a thorough understanding of how elements such as valves and sensors influence the gas conditions along the supply line, and, most importantly, how these effects ultimately impact engine performance in real-world scenarios. Furthermore, once the experimental setup has been constructed, this model can serve as a reference to verify the correctness of the assembly process and to assess the accurate implementation of the physical system.

A script has been developed in MATLAB® to support the Simulink® model by allowing direct modification of several key parameters—such as pressure, temperature (with automatic density updates), and the diameter of the detonation tube—within the MATLAB® environment, thereby eliminating the need to manually adjust these values within the simulation model blocks.

## 3.1 Integration Method

The solver ode15s is employed because it is a multi-physics system: hence, the different systems, such as the gas and mechanical, have different characteristic time-scales. For this reason, the problem is stiff. In this simulation, indeed, ode45 results to be highly inefficient. Additionally, both ode113 and ode23 are also found to be very inefficient. On the other hand, the efficiency is significantly improved with ode23s and ode15s, as these solvers, which employ multi-step methods, are specifically designed for stiff systems, whereas the other solvers mentioned are intended for non-stiff problems. Therefore, ode15s is selected as, in general, it yields more accuracy than ode23s.

## 3.2 Feeding Line Model

Figure 50 presents the Simulink® implementation of the scheme illustrated in Figure 38. The same numbering of components is retained, as clarified in the figure caption.

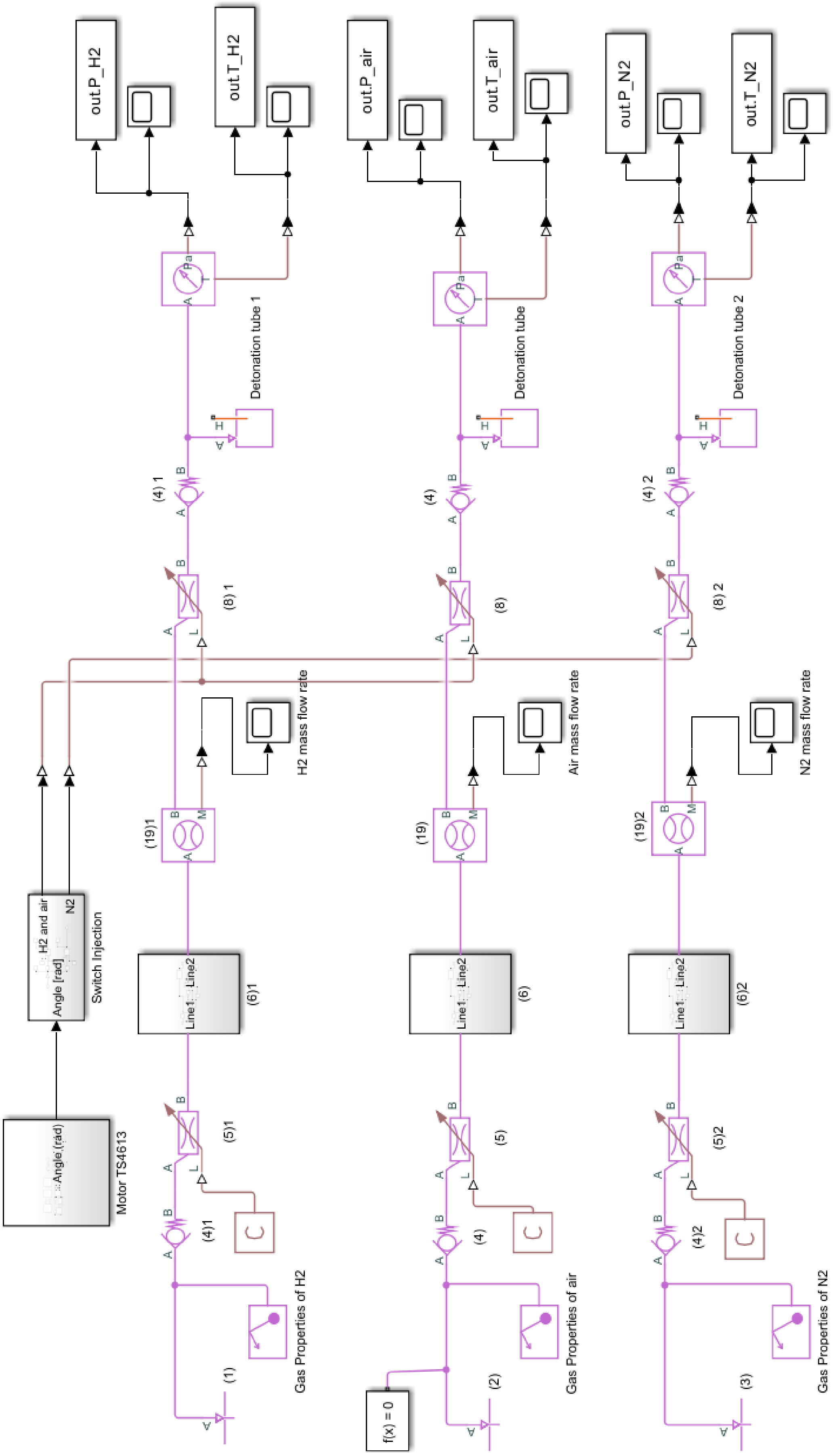

Figure 50: Feeding line system - Simulink® 1) Hydrogen Tank; 2) Air Tank; 3) Nitrogen Tank; 4) Check Valves; 5) Critical Flow Nozzles; 6) Flame Arrestors; 8) Injectors; 19) Flow Meters

The model is based on the ideal gas assumption, and therefore, the ideal gas law is employed to calculate the gas density for any given combination of initial temperature and pressure in the MATLAB® script. Figure 51 provides a detailed view of the components along the feeding lines.

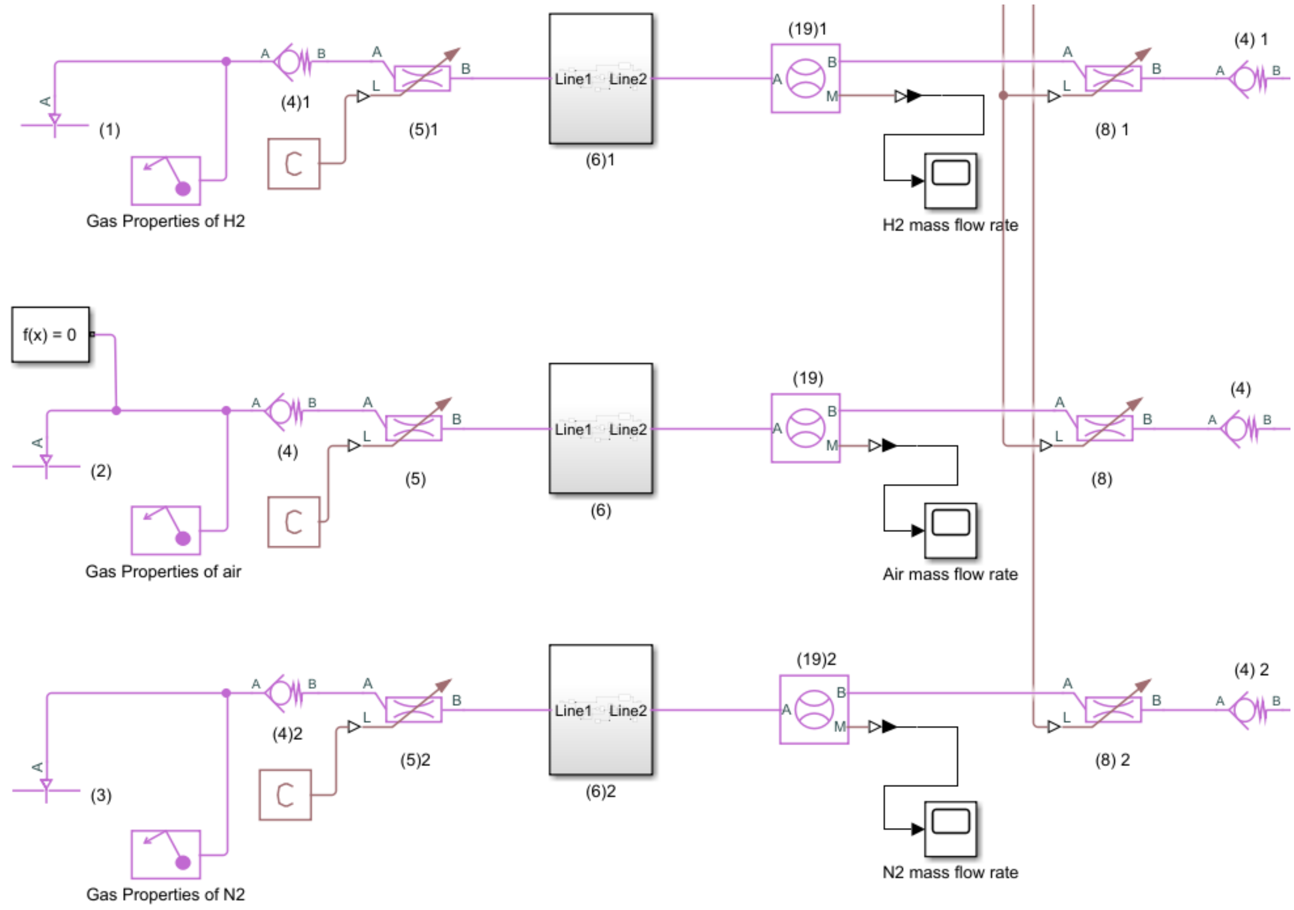

Figure 51: Fuel-oxidizer system feeding lines - Simulink® 1) Hydrogen Tank; 2) Air Tank; 3) Nitrogen Tank; 4) Check Valves; 5) Critical Flow Nozzles; 6) Flame Arrestors; 8) Injectors; 19) Flow Meters

The **Reservoir** blocks (labelled as (1), (2) and (3) in Figure 51) represent the gas tanks. These blocks are initialized through a MATLAB® script that sets the initial pressure, temperature and feeding line diameter.

The **Gas Properties** block is configured based on the ideal gas assumption. It computes property variations according to the defined temperature and pressure, thus requiring parameter input only for a reference state. The values at reference conditions $T = 298.15$K, $P = 1$ bar are reported in Table 18.

| **Property** | **Hydrogen ($H_2$)** | **Air** | **Nitrogen ($N_2$)** |
|---|---|---|---|
| Specific gas constant $R$ [J/(kg·K)] | 4124.0 | 287.0 | 296.8 |
| Specific enthalpy at reference temperature $h_{\text{ref}}$ [kJ/kg] | 0 | 299.6 | 0 |
| Specific heat at constant pressure $c_p$ [J/(kg·K)] | 14306 | 1005 | 1041 |
| Dynamic viscosity $\mu$ [$\mu$Pa·s] | 8.9 | 18.5 | 17.8 |
| Thermal conductivity $k$ [mW/(m·K)] | 186 | 26.3 | 25.8 |

Table 18: Thermophysical properties of gases at reference conditions: $T = 298.15$ K and $P = 1$ bar [37] [1]

The remaining components match the elements presented in Figure 38. The parameters of the **Check Valve** and **Orifice** blocks are defined based on manufacturer datasheets, the experimental pressure range (up to 10 bar according to the Reduced Order Model (ROM)), and standard values ensuring numerical stability in simulation (e.g., pressure differential ratio factor for choked flow $x_T = 0.7$ and smoothing factor = 0.01). Since the selected valves are high-efficiency, the leakage flow fraction is set to very low values ($10^{-6}$), ensuring near-total closure in reverse flow. The maximum $C_v$ values are sufficiently high to avoid flow limitations: $C_{v,H_2} = 8.5$, $C_{v,N_2} = 7$, $C_{v,air} = 7.5$.
Despite the low leakage, its impact must be considered: during the purge phase, the nitrogen injection valve is closed, yet a small flow of $N_2$ enters the detonation tube due to leakage — this flow is directly tied to the leakage coefficient.

The **Orifice** block is employed to simulate:

- critical flow nozzles, modelling compressible flow through restrictions;
- injectors, with dynamic opening behaviour governed by control signals.

The opening fraction is controlled by the physical signal port L:

- L=0: orifice closed;
- L=1: fully open.

No active control is applied to the critical flow nozzles (L = constant 1), whereas injector control is performed via the rotary valve (not shown here, but discussed later).

Flow meters are modeled using **Flow Rate Sensor** blocks. Their temperature limitations, as per manufacturer specifications (see Section 2.5.2), are enforced through logic in the Flame Arrestor subsystem.
For the flame arrestor (element (6) in Figure 51), no standard Simulink® block exists. Following the description in Section 2.5.2, the configuration in Figure 52 is adopted (shown only for the air line; other lines are equivalent, differing only in temperature thresholds).

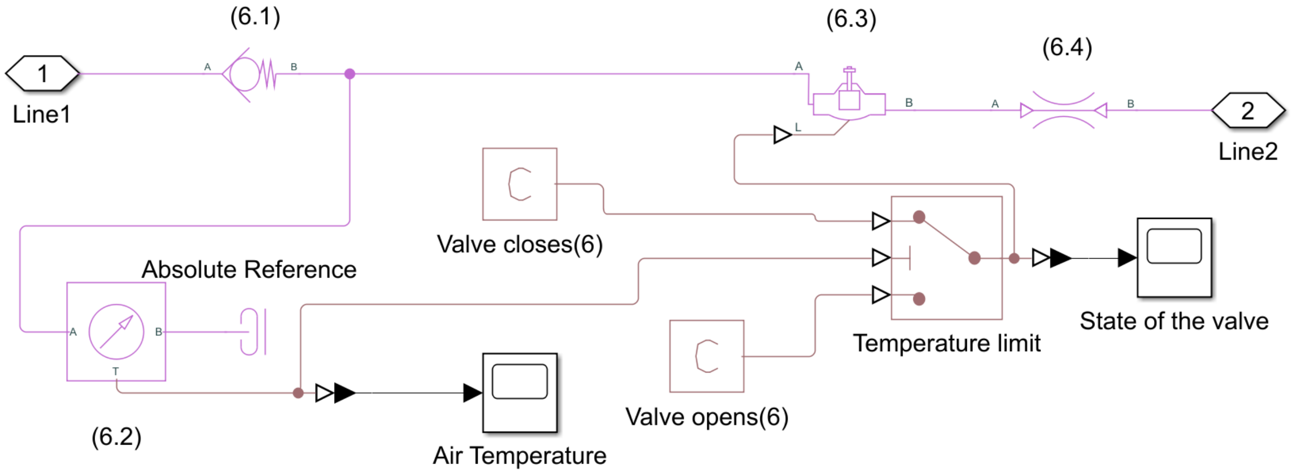

Figure 52: Flame arrestor subsystem (6) - Simulink®. 6.1) Gas non-return valve; 6.2) Temperature sensor; 6.3) Shut-off valve; 6.4) Pressure loss block

- The non-return valve (6.1) is modeled as a check valve, using the same parameters discussed previously.
- The **Temperature Sensor**, **PS Switch** and **Gate Valve** represent the thermal shut-off mechanism. If the temperature exceeds a critical threshold, the valve interrupts the gas flow to prevent the onset of ignition conditions along the line. The **PS Switch** block is configured to enforce this behaviour: when the temperature surpasses the predefined limit—set by the flow meter specifications, as described in Section 2.5.2 of Chapter 2 (70°C for air and $N_2$, and 180°C for $H_2$)—it sets the input to port L of the **Gate Valve** to 0, thereby commanding the valve to close.

Parameters for the **Gate Valve** are aligned with the general modelling approach (same leakage and smoothing factors). Pressure losses in the flame arrestor are simulated using a **Local Restriction** block with discharge coefficient $C_d = 0.7$, in line with manufacturer data (WITT® datasheet [29]).

Additionally, maximum flow rate limits imposed by the arrestor must be respected throughout the simulation:

- 0.287 kg/s for air and $N_2$;
- for hydrogen, the limit depends on the desired pressure drop. Example: with 10 bar inlet and 4 bar outlet ($\Delta P = 6$ bar), the max flow is approximately 0.023kg/s.

There is no standard Simulink® block available for modelling a rotary valve. Therefore, its behaviour is implemented using mechanical components, with control logic based on angular position. Initially, the electromagnetic motor TS4613, which drives the valve, is modeled using the **Induction Machine Squirrel Cage** block, representing a three-phase asynchronous motor, as shown in Figure 53. This Simulink® model implements a three-phase asynchronous motor coupled to a rotary valve, which acts as a mechanical load. Both a **Grid-Side Converter (GSC)** and a **Machine-Side Converter (MSC)** are used within the Motor Controls subsystem to regulate energy flow and motor dynamics. The rotary valve is modelled using mechanical elements such as the **Inertia** block, and its operation is controlled by a logic system based on an **Angle Sensor**. Key components of the Motor TS4613 Subsystem are illustrated in Appendix A.

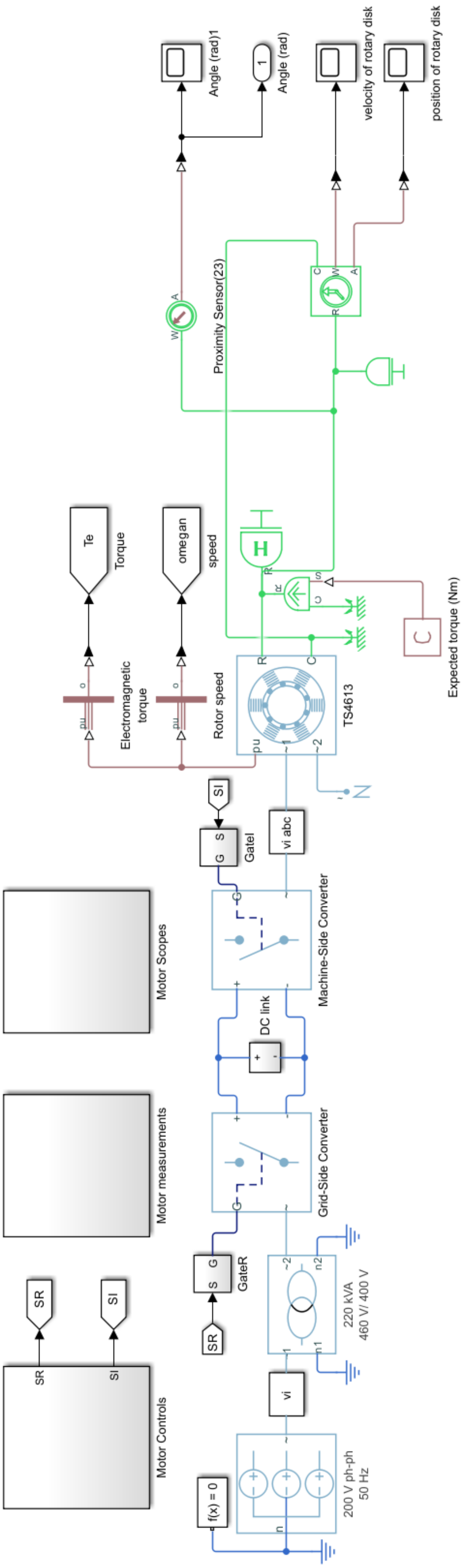

Figure 53: Motor TS4613 Subsystem - Simulink®

As an illustrative example, Figure 54 shows the output of the **Angle sensor** block within the Motor TS4613 subsystem.

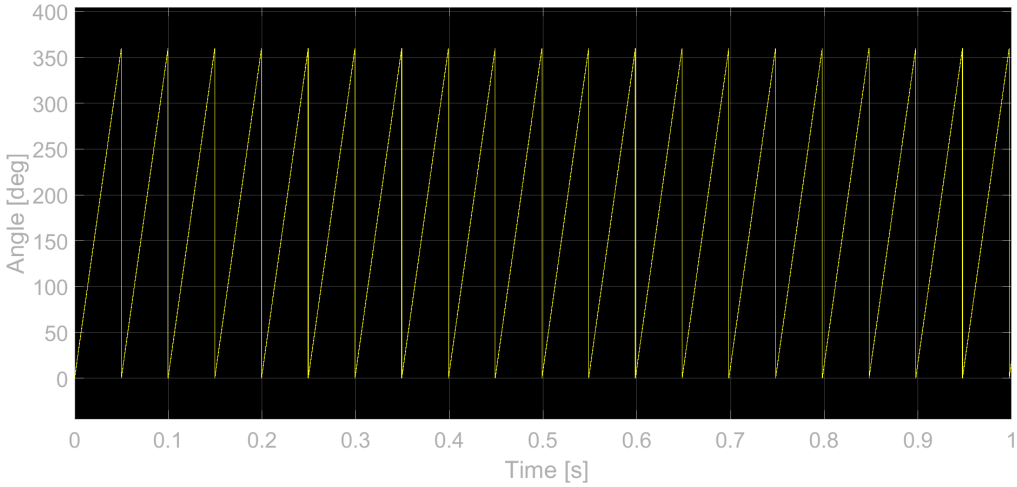

Figure 54: Angle Scope inside Motor TS4613 Subsystem for a frequency of 20 Hz - Simulink®

Depending on the selected operating frequency, different angular profiles are generated. The variation between plots lies in the number of rotations (cycles) per unit time.
As shown in Figure 31, the injection of air and $H_2$ takes place during the clockwise rotation of the valve disk between $0^\circ$ and $240^\circ$, followed by the ignition phase from $240^\circ$ to $310^\circ$, and finally the purge injection phase occurs from $310^\circ$ to $365^\circ$, completing the cycle. These angular boundaries can be modified based on the desired mass flow rates, filling fraction, and oxidizer-to-fuel ratio.
As illustrated in Figure 50, the Injection Subsystem receives the output of the **Angle Sensor** (labelled as `Angle [rad]`) from the Motor TS4613 subsystem. This value is processed using a switch-based logic system, shown in Figure 55, to generate the binary control signals for the injectors (elements labelled as (8) in Figure 50).

The control logic in Simulink® is implemented using the following blocks:

1. **Compare To Constant**;
2. **Switch**.

If the angular position of the rotary disk is $\leq 240^\circ$, the system triggers the injection of $H_2$ and air. In this case, the **Compare To Constant** block, relative to $H_2$ and air, outputs a logical 1, which satisfies the condition of the **Switch** block (i.e., input $> 0$), and the switch outputs a constant value of 1. This value corresponds to the command signal for opening the $H_2$ and air injectors.
Similarly, for the $N_2$ purge injection, the logic is activated when the angle is $\geq 310^\circ$, following the same implementation principle as the propellant injection.
Continuing with the same example presented earlier at a rotational frequency of 20 Hz, the output signals corresponding to the **Command H2 and air Scope** and the **Command N2 Scope** are shown in Figures 56 and 57, respectively. These plots are taken directly from the Simulink® model and illustrate the activation signals sent to the injectors.

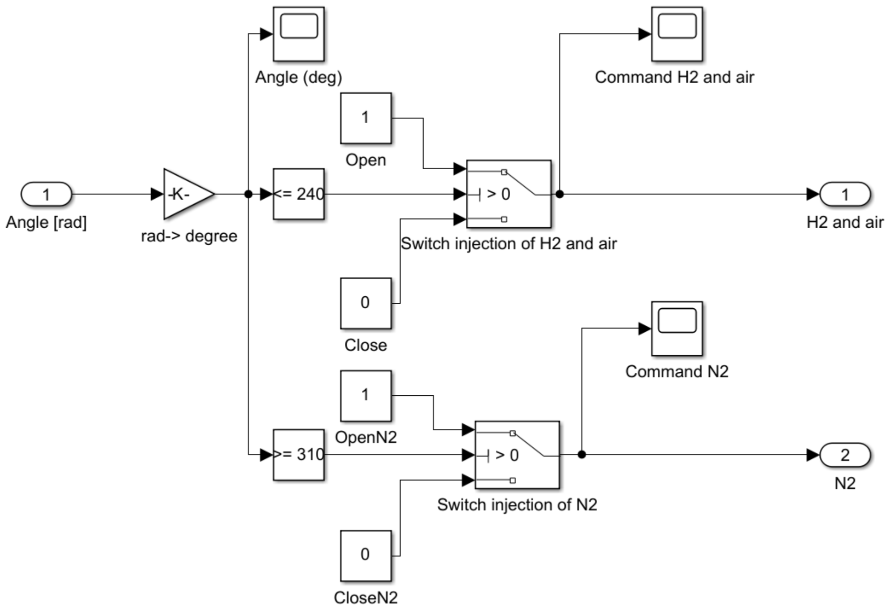

Figure 55: Switch Injection Subsystem - Simulink®

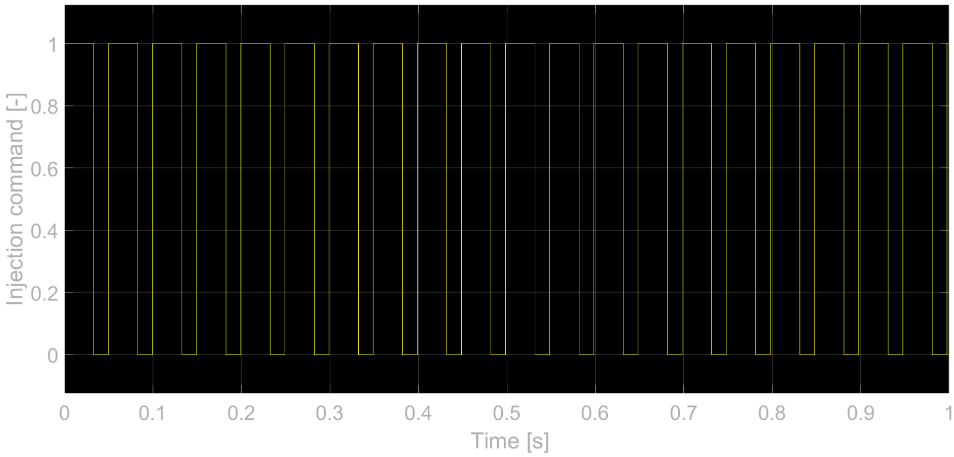

Figure 56: Command $H_2$ and air plot inside Switch Injection Subsystem for a frequency of 20 Hz - Simulink®

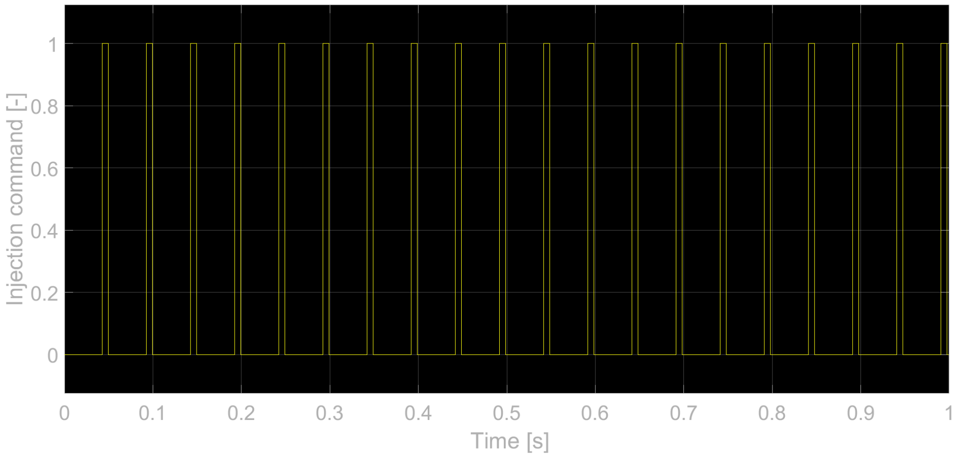

Figure 57: Command $N_2$ plot inside Switch Injection Subsystem for a frequency of 20 Hz - Simulink®

As previously stated, a command value of 1 corresponds to an open signal for the injection valve, as it is passed to the L port of the **Orifice** block (see Figure 50). Conversely, a command value of 0 closes the valve.

As shown in Figure 50, the detonation tube is represented by a **Constant Volume Chamber** block, configured with the same dimensions as the actual detonation tube. The temperature and pressure at the outlet of the feeding line serve as inputs to the ROM used to simulate the detonation process. This approach allows for the inclusion of pressure losses and non-ideal effects of the components along the feeding line in the performance evaluation of the PDE. These pressure and temperature values are transferred to the MATLAB® script via the **To Workspace** block.

## 3.3 Reduced Order Model

A reduced-order model was developed using high-order singular value decomposition (HOSVD) applied to a data tensor derived from computational fluid dynamics (CFD) simulations performed by Universidad Politécnica de Madrid and Universidad de Vigo (Spain) [36]. Their method is used in this model. Their methodology is intended to address both the direct (performance prediction) and inverse (design optimization) problems encountered during the conceptual design phase of a PDE.
In the direct problem, prescribed operational and geometric parameters are used to predict the engine's performance outputs. Conversely, in the inverse problem, desired performance metrics are used to infer the required input conditions. The tool developed was found to produce results that, on average, deviate by less than 10% from high-fidelity CFD data.
From a practical perspective, this method significantly reduces the online computational burden by shifting the intensive CFD computations offline. The resulting ROM-based framework, which combines CFD with tensor decomposition, maximizes information extraction from a limited number of high-fidelity simulations, making it suitable for rapid performance assessment and conceptual design of PDEs.
A key innovation of this work lies in its ability to maintain a high level of model fidelity-featuring 1D CFD with detailed 10-species chemical kinetics and a modeled blowdown phase- while achieving response times typical of zero-dimensional algebraic methods (i.e., under 0.1 seconds). This efficiency is made possible by solving both performance and design problems on a reduced-order representation of the PDE simulation database, rather than on the PDE model itself.
The PDE configuration considered is idealized as a cylindrical tube of constant diameter, without a nozzle. Propellants are injected from the closed end, while the open end allows for thrust generation. The engine cycle is divided into four phases:

1. filling: fresh propellants with a specified mixture ratio are injected into the tube, displacing the inert gas. Ideal mixing is assumed;
2. ignition: a detonation wave is initiated at the closed end and propagates through the tube;
3. exhaust: high-pressure combustion products are expelled through the open end, generating thrust;
4. purging: once pressure drops below a threshold, an inert gas is injected to purge combustion products, preparing the tube for the next cycle.

The PDE model is described by six input parameters (P1–P6), which define its geometry, configuration and operational settings:

- P1: initial gas temperature, $T_0$ [K];
- P2: equivalence ratio, $\phi$;
- P3: initial pressure, $P_0$ [bar];
- P4: tube length, L [m];
- P5: tube diameter, D [m];
- P6: relaxation time between detonations, $t_{off}$ [s], accounting for both purging and refilling.

Corresponding output performance parameters (Q1–Q7) include:

- Q1: initial temperature, $T_0$ [K];
- Q2: total impulse per cycle, $I_T$ [Ns];
- Q3: specific impulse, $I_{sp}$ [m/s];
- Q4: detonation frequency, $f$ [Hz];
- Q5: peak thrust, $E_{max}$ [N];
- Q6: peak pressure, $P_{max}$ [bar];
- Q7: ejected mass per cycle, $M_T$ [kg].

The allowable ranges for these input parameters are summarized in Table 19.

| **Parameter** | **Range** |
|---|---|
| $T_0$ [K] | 250–350 |
| $P_0$ [bar] | 0.5–10 |
| $\phi$ | 0.5–1.05 |
| $L$ [m] | 0.4–1.5 |
| $D$ [m] | 0.01–0.25 |
| $t_{\text{off}}$ [s] | 0–0.1 |

Table 19: Ranges of the input parameters

The methodology was structured into two main components:

1. PDE Model Development
    - Step 1: Numerical Simulation. A 1D CFD solver was used, following precedents in the literature but extended to include:
        - a 10-species, 25-reaction detailed chemistry model;
        - discharge into a low ambient pressure environment.

      A total of 480 simulations were performed.
    - Step 2: Data Reduction. Simulation data were reduced using a structured approach to populate the performance database.
2. Data Processing Algorithm

- Step 3: Database Generation. Seven 6-dimensional tensors were created, each corresponding to one output parameter (Q1–Q7), structured over the six input dimensions (P1–P6).
- Step 4: Database Decomposition. The HOSVD method was employed to decompose each tensor and extract dominant modes (eigenpatterns) that capture most of the database's variance.
- Step 5: Inverse Problem Solution. The ROM enables fast evaluation of inverse problems by interpolating within the compressed feature space.

The assumptions include a one-dimensional flow model, applicability only to hydrogen–air mixtures, and fixed boundary conditions: a closed end at $x = 0$ and an open end at $x = L$.
The inputs values are rescaled from normalized coordinates [0,1] to their physical representations. The ROM function mapping input parameters (P1–P6) to output predictions (Q1–Q7) can be expressed as:

$$(T_0, I_T, I_{sp}, f, E_{max}, P_{max}, M_T) = f_{\mathrm{DR}}(T_0, P_0, \phi, L, D, t_{off}) \tag{35}$$

The relaxation time $t_{off}$ accounts for purging, refilling, and any optional delay between cycles.
The internal flow of the PDE is modeled as an unsteady, one-dimensional compressible flow with chemical reactions. This approach captures the essential physical phenomena—detonation wave propagation and post-detonation gas expansion—while maintaining computational efficiency. The governing equations are the one-dimensional compressible Euler equations, which conserve mass, momentum, energy and species mass fractions. For a reactive mixture, the conservative variables are defined as:

$$\mathbf{U} = \begin{bmatrix} \rho \\ \rho u \\ \rho E \\ \rho Y_k \end{bmatrix} \tag{36}$$

Here, $\rho$ denotes the density of the gas mixture, $u$ is the velocity, $E$ is the specific total energy, and $Y_k$ is the mass fraction of species $k$.
The chemical kinetics mechanism for the $H_2$-air mixture includes N=10 species and M=25 elementary reactions. The reactions and their respective forward Arrhenius coefficients are listed in Table 23, Appendix A.
The initial and final species mass fractions resulting from hydrogen combustion in air (considered as a mixture of $O_2$ and $N_2$ in a 1:3.76 molar ratio) are determined under the assumption of complete combustion. The equivalence ratio $\phi$ characterizes the fuel-air mixture as:

- fuel-rich if $\phi > 1$;
- stoichiometric if $\phi = 1$;
- fuel-lean if $\phi < 1$.

Before combustion, the mixture consists of hydrogen $H_2$, oxygen $O_2$, and nitrogen$N_2$, with mass fractions summing to one. These are calculated as:

$$Y_{H_2,i} = \frac{2 \cdot W_{H_2}}{2 \cdot W_{H_2} + \frac{1}{\phi}(W_{O_2} + 3.76 \cdot W_{N_2})} \tag{37}$$

$$Y_{O_2,i} = \frac{\frac{1}{\phi} \cdot W_{O_2}}{2 \cdot W_{H_2} + \frac{1}{\phi}(W_{O_2} + 3.76 \cdot W_{N_2})} \tag{38}$$

$$Y_{N_2,i} = \frac{3.76 \cdot \frac{1}{\phi} \cdot W_{N_2}}{2 \cdot W_{H_2} + \frac{1}{\phi}(W_{O_2} + 3.76 \cdot W_{N_2})} \tag{39}$$

$$Y_{H_2O,i} = 0 \tag{40}$$

Here, $W_{H_2}, W_{O_2}, W_{N_2}$ represent the molar masses of hydrogen, oxygen, and nitrogen, respectively. After combustion, the final species are water vapor $H_2O$ and nitrogen, with potential residual hydrogen or oxygen depending on $\phi$.

**Case 1: Fuel-rich mixture** ($\phi > 1$)

$$Y_{H_2O,f} = \frac{2 \cdot \frac{1}{\phi} \cdot W_{H_2O}}{2 \cdot \frac{1}{\phi} \cdot W_{H_2O} + \frac{1}{\phi} \cdot 3.76 \cdot W_{N_2} + (2 - 2 \cdot \frac{1}{\phi}) \cdot W_{H_2}} \tag{41}$$

$$Y_{H_2,f} = \frac{(2 - 2 \cdot \frac{1}{\phi}) \cdot W_{H_2}}{2 \cdot \frac{1}{\phi} \cdot W_{H_2O} + \frac{1}{\phi} \cdot 3.76 \cdot W_{N_2} + (2 - 2 \cdot \frac{1}{\phi}) \cdot W_{H_2}} \tag{42}$$

$$Y_{O_2,f} = 0 \tag{43}$$

$$Y_{N_2,f} = \frac{\frac{1}{\phi} \cdot 3.76 \cdot W_{N_2}}{2 \cdot \frac{1}{\phi} \cdot W_{H_2O} + \frac{1}{\phi} \cdot 3.76 \cdot W_{N_2} + (2 - 2 \cdot \frac{1}{\phi}) \cdot W_{H_2}} \tag{44}$$

**Case 2: Fuel-lean mixture** ($\phi < 1$)

$$Y_{H_2O,f} = \frac{2 \cdot W_{H_2O}}{2 \cdot W_{H_2O} + \frac{1}{\phi} \cdot 3.76 \cdot W_{N_2} + \left(\frac{1}{\phi} - 1\right) \cdot W_{O_2}} \tag{45}$$

$$Y_{H_2,f} = 0 \tag{46}$$

$$Y_{O_2,f} = \frac{\left(\frac{1}{\phi} - 1\right) \cdot W_{O_2}}{2 \cdot W_{H_2O} + \frac{1}{\phi} \cdot 3.76 \cdot W_{N_2} + \left(\frac{1}{\phi} - 1\right) \cdot W_{O_2}} \tag{47}$$

$$Y_{N_2,f} = \frac{\frac{1}{\phi} \cdot 3.76 \cdot W_{N_2}}{2 \cdot W_{H_2O} + \frac{1}{\phi} \cdot 3.76 \cdot W_{N_2} + \left(\frac{1}{\phi} - 1\right) \cdot W_{O_2}} \tag{48}$$

These formulations ensure mass conservation and accurately represent the stoichiometry of hydrogen-air combustion, with adjustments for any excess reactants.
The mixture-specific gas constant $R$ is calculated as:

$$R = R_u \left( \frac{Y_{H_2}}{W_{H_2}} + \frac{Y_{O_2}}{W_{O_2}} + \frac{Y_{N_2}}{W_{N_2}} \right) \tag{49}$$

where $R_u$ is the universal gas constant. The initial density of the mixture is given by:

$$\rho_0 = \frac{P_0}{R \cdot T_0} \tag{50}$$

Additional definitions:

- initial fuel mass per unit area:

$$M_\mathrm{f} = \rho_0 \cdot Y_{H_2,i} \cdot L_\mathrm{tube} \tag{51}$$

- specific chemical energy release per unit mass of fuel, assuming complete combustion:

$$q_0 = \frac{1}{Y_{\mathrm{H}_2,i}} \left| \Delta h_\mathrm{products} - \Delta h_\mathrm{reactants} \right| \tag{52}$$

  Expanded as:

$$q_0 = \frac{1}{Y_{H_2,i}} \cdot \left| \left( \frac{Y_{H_2,f}}{W_{H_2}} \cdot \Delta H^\circ_{f,H_2} + \frac{Y_{H_2O,f}}{W_{H_2O}} \cdot \Delta H^\circ_{f,H_2O} + \frac{Y_{O_2,f}}{W_{O_2}} \cdot \Delta H^\circ_{f,O_2} + \frac{Y_{N_2,f}}{W_{N_2}} \cdot \Delta H^\circ_{f,N_2} \right) \right.$$
$$\left. - \left( \frac{Y_{H_2,i}}{W_{H_2}} \cdot \Delta H^\circ_{f,H_2} + \frac{Y_{H_2O,i}}{W_{H_2O}} \cdot \Delta H^\circ_{f,H_2O} + \frac{Y_{O_2,i}}{W_{O_2}} \cdot \Delta H^\circ_{f,O_2} + \frac{Y_{N_2,i}}{W_{N_2}} \cdot \Delta H^\circ_{f,N_2} \right) \right| \tag{53}$$

  where:

  - $q_0$ : specific chemical energy per unit mass of hydrogen fuel [J/kg];
  - $Y_i$ and $Y_f$ : initial and final mass fractions of each chemical species, respectively;
  - $W_x$ : molar mass of species $x$;
  - $\Delta H^\circ_{f,x}$: standard enthalpy of formation of species $x$, [J/mol];
  - the use of the absolute value ensures that the resulting quantity is positive, corresponding to the energy released during the combustion process;
  - the entire expression is normalized by the initial mass fraction of hydrogen fuel, $Y_{H2,i}$, in order to express the energy on a per-unit-mass-of-fuel basis, rather than per unit mass of the entire mixture.

  This formulation quantifies the net chemical energy released by the combustion reaction, referenced specifically to the mass of the fuel. It captures the total enthalpy difference between reactants and products and is essential for assessing the thermodynamic performance of the PDE.

A dimensional analysis was first performed to guide the scaling process. Then, a trial-and-error procedure was employed to identify the dimensionless variables that best collapse the data. The following normalized variables and parameters were introduced:

$$\tilde{x} = \frac{x}{L} \tag{54}$$

$$\tilde{t} = \frac{t}{\phi^{-3/8} L / \sqrt{q}} \tag{55}$$

$$\tilde{\rho} = \frac{\rho}{\phi^{-1} M_f / L} \tag{56}$$

$$\tilde{u} = \frac{u}{\phi^{3/8} \sqrt{q}} \tag{57}$$

$$\tilde{p} = \frac{p}{\phi^{-1/4} M_f q / L} \tag{58}$$

$$\tilde{T} = \frac{T}{\phi^{3/4} q / R_{g,0}} \tag{59}$$

$$\tilde{F}_x = \frac{F_x}{\phi^{-1/4} M_f q / L} \tag{60}$$

$$\tilde{\dot{m}} = \frac{\dot{m}}{\phi^{-5/8} M_f \sqrt{q} / L} \tag{61}$$

$$\tilde{M} = \frac{M}{\phi^{-1} M_f} \tag{62}$$

$$\tilde{I} = \frac{I_t}{\phi^{-5/8} M_f \sqrt{q}} \tag{63}$$

$$\tilde{t}_{wave} = \frac{t_{wave}}{\phi^{-3/8} L / \sqrt{q}} \tag{64}$$

$$\tilde{t}_{end} = \frac{t_{end}}{\phi^{-3/8} L / \sqrt{q}} \tag{65}$$

$$\tilde{FV} = \frac{FV}{\phi^{3/8} \sqrt{q}} \tag{66}$$

where:

- $M_f$ : initial mass of fuel per unit area;
- $q$ : total heat released per unit mass of fuel (based on JANAF data and complete combustion);
- $t_{wave}$ : time required for the detonation wave to reach the tube exit ($x = L$);
- $t_{end}$ : total simulation time, including detonation and blowdown phases.

The following physical quantities are reconstructed from dimensionless CFD simulation data, using appropriate scaling laws derived from dimensional analysis. Each dimensionless profile is retrieved from the database `DDBB.nondim` and multiplied by a corresponding dimensional scaling factor to obtain the final physical quantity:

$$t = \tilde{t} \cdot \phi^{-3/8} \cdot \frac{L_{\text{tube}}}{\sqrt{q_0}} \tag{67}$$

$$P_{\text{outlet}} = \tilde{P} \cdot \phi^{-1/4} \cdot \frac{q_0 \cdot M_{\text{fuel}}}{L_{\text{tube}}} \tag{68}$$

$$T_{\text{outlet}} = \tilde{T} \cdot \phi^{3/4} \cdot \frac{q_0}{R} \tag{69}$$

$$\rho_{\text{outlet}} = \tilde{\rho} \cdot \phi^{-1} \cdot \frac{M_{\text{fuel}}}{L_{\text{tube}}} \tag{70}$$

$$U_{\text{outlet}},\ a_{\text{outlet}} \propto \phi^{3/8} \cdot \sqrt{q_0} \tag{71}$$

$$M_{\text{outlet}} = \tilde{M}_{\text{outlet}} \cdot 1 \tag{72}$$

$$\left(\frac{G}{A}\right)_{\text{outlet}} = \left(\frac{\tilde{G}}{A}\right)_{\text{outlet}} \cdot \left(\phi^{-5/8} \cdot \frac{\sqrt{q_0} \cdot M_{\text{fuel}}}{L_{\text{tube}}}\right) \tag{73}$$

where:

- $\sqrt{q_0}$: square root of the chemical energy per unit mass of fuel;
- $M_{\text{fuel}}/L_{\text{tube}}$: fuel mass per unit tube length;
- $\phi^p$: empirical scaling exponent from similarity analysis (with p a rational number).

The outlet thrust per unit area is given by:

$$\left(\frac{E}{A}\right)_{\text{outlet}} = \left(\frac{\tilde{E}}{A}\right)_{\text{outlet}} \cdot \left(\phi^{-1/4} \cdot \frac{q_0 \cdot M_{\text{fuel}}}{L_{\text{tube}}}\right) \tag{74}$$

This expression scales with:

- $q_0 \cdot M_{\text{fuel}}/L_{\text{tube}}$: total available energy per unit length;
- $\phi^{-1/4}$: scaling coefficient to match the ROM.

The Mach number does not require rescaling, as it is inherently dimensionless:

$$Y_{\text{H}_2\text{O,outlet}} = \tilde{Y}_{\text{H}_2\text{O,outlet}} \cdot 1 \tag{75}$$

Mass fractions, being dimensionless, are also left unscaled. All the rescaled variables match the profiles stored in the `DDBB.nondim` database. Several key performance metrics are computed from the rescaled data:

- Total impulse:

  $$I_T = A \cdot \int_0^{t_{\text{end}}} \frac{E}{A}(t)\, dt \tag{76}$$

  Total expelled mass:

  $$G_{\text{tot}} = A \cdot \int_0^{t_{\text{end}}} \left(\frac{G}{A}\right)(t)\, dt \tag{77}$$

  where

  - $G_{\text{tot}}$ : total ejected mass [kg];
  - $\left(\frac{G}{A}\right)(t)$ : mass flow rate per unit area over time [kg/(s·m$^2$)];
  - $A$ : cross-sectional area of the detonation tube [m$^2$];
  - $t_{\text{end}}$ : duration of the blowdown phase [s].

  In the MATLAB® implementation, the integral is approximated using the trapezoidal rule:

  ```
  Gtot = trapz(outs.GA_outlet(1:end-1) .* diff(outs.time)) * A;
  ```

- Specific impulse:

  $$I_{sp} = \frac{I_T}{\text{Total Mass Flow}} = \frac{I_T}{G_{\text{tot}}} \tag{78}$$

- Operating frequency:

  The PDE Cycle duration consists of three phases:

  1. $t_{\text{end,dim}}$: dimensional duration of the detonation phase.

  $$t_{\text{end,dim}} = t_{\text{end}} \cdot \phi^{-3/8} \cdot \frac{L_{\text{tube}}}{\sqrt{q_0}} \tag{79}$$

2. $t_{\text{refill}}$: estimated refill time (assumed to be 20 times the characteristic flow time).

$$t_{\text{refill}} = 20 \cdot \phi^{-3/8} \cdot \frac{L_{\text{tube}}}{\sqrt{q_0}} \tag{80}$$

3. $t_{\text{off}}$: idle time between cycles (user-defined input).

The total cycle time and frequency are:

$$t_{\text{cycle}} = t_{\text{end,dim}} + t_{\text{refill}} + t_{\text{off}} \tag{81}$$

$$f = \frac{1}{t_{\text{cycle}}} \tag{82}$$

As implemented in MATLAB®:

```
tenddim = DDBB.tend*(ERatio^(-3/8)*Ltube/sqrt(q0));
tref = 20*(ERatio^(-3/8)*Ltube/sqrt(q0));
tcic = tenddim + tref + toff;
f = 1/tcic;
```

- Peak thrust and pressure:

$$\max(E/A), \quad \max(P_{\text{outlet}}) \tag{83}$$

- Total ejected mass: $\int \dot{m}(t)dt$
- Alternative (Energy-Based) Specific Impulse: computed by integrating momentum and pressure forces:

$$I_{sp,\text{fuel}} = \frac{1}{M_{\text{fuel}} \cdot g} \int_0^{t_{\text{end}}} \left(\rho U^2 + P\right) \, dt \tag{84}$$

The final output vector is normalized to the [0,1] interval using min-max normalization:

```
outs.outsapp = (outs.outsapp - DDBB.mins)./(DDBB.maxs - DDBB.mins);
```

This method was benchmarked against full CFD simulations by Universidad Politecnica de Madrid. The comparison revealed that, for all performance parameters, the maximum mean errors (ranging between 5% and 10%) occurred in the estimation of specific impulse and peak cycle pressure. For all other parameters, mean errors remained below 2%.

In the context of current industrial practice, such levels of accuracy are considered acceptable during the conceptual design phase, where rapid evaluation of performance trends is prioritized over high-fidelity precision. Naturally, these error margins would be unacceptable in the context of a detailed design phase, where precise performance predictions are required. However, within the early-stage conceptual design, these approximations offer a suitable trade-off between accuracy and computational efficiency.

The authors acknowledge two principal limitations of the proposed approach:

1. assumption of one-dimensional flow: the method relies on a 1D flow approximation within the PDE, while the actual physical system exhibits fully three-dimensional behaviour. As a result, important 3D phenomena such as non-uniform mixing, discrete fuel injection and transverse instabilities are not captured. While

simplified correction models could, in principle, be introduced to account for some of these effects, doing so would add complexity on top of an already simplified framework—potentially undermining the original objective of efficiency;

2. limited information from sparse databases: the method depends on a ROM derived from a finite number of CFD simulations. Consequently, the quality of predictions depends on the density of the database. If the training set is too sparse, the HOSVD used to interpolate results may introduce significant errors. The user should monitor the eigenmode decay in the decomposition to assess the reliability of interpolated results and determine an acceptable level of sparsity.

Despite these limitations, the proposed methodology effectively fulfills the primary goal of a conceptual design tool: to enable fast and cost-effective performance screening. It helps to quickly identify the operating conditions that yield optimal performance, reducing the time and computational cost associated with exhaustive parametric CFD studies in early-stage designs. This efficiency can significantly shorten the path to a more detailed and refined design process, which may later involve high-fidelity simulations and experimental validation.

## 3.4 Results

One of the most significant results to present is the pressure loss caused by components along the feeding line, such as check valves and flashback arrestors.

To verify the reliability of both the results and the model, a representative case is considered with an inlet pressure of 10 bar and an inlet temperature of 293.15 K for all three feeding lines. By running the simulation in Simulink®, the resulting pressure at the end of the feeding line for hydrogen (denoted as `out.P`$_{H_2}$ in Figure 50) is shown in Figure 58.

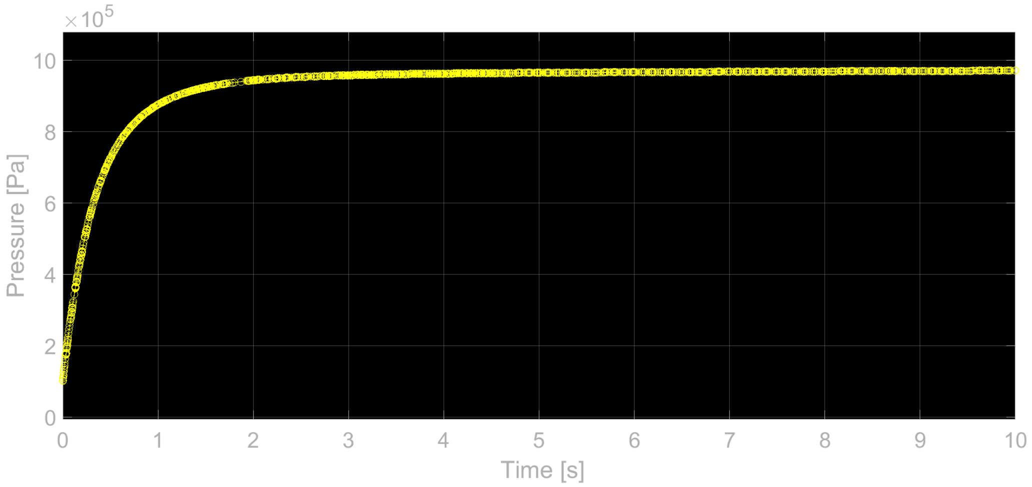

Figure 58: Pressure of $H_2$ at the end of the feeding line - Simulink®

Similar pressure trends are observed in the simulations of the other feeding lines. As illustrated in Figure 58, once the system reaches steady-state conditions, the pressure at the end of the line is 9.70 bar—slightly lower than the initial 10 bar. This result aligns with the data provided in the datasheets of the components discussed in Chapter 2. In particular, the primary sources of pressure loss along the line are:

1. flashback arrestors: these typically induce a pressure drop in the range of 0.1 to 0.5 bar

for air and hydrogen, depending on the operating conditions;

2. critical flow nozzles: the pressure loss is approximately $6{\cdot}10^{-3}$ times the difference between the inlet pressure and atmospheric pressure (i.e., around 0.06 bar for an inlet pressure of 10 bar).

Other sources of pressure loss are considered negligible.
Therefore, the observed pressure drop of 0.3 bar is fully consistent with the specifications provided by the component manufacturers.
It should be noted that, for clarity of presentation in Figure 58, the intermittent behaviour of the rotary valve is not included. The purpose of this plot is to demonstrate that the pressure losses in the Simulink® model align with those specified for the selected components.
Additionally, the temperature is slightly affected by the elements in the feeding line, stabilizing at 293.42 K in this case. However, as this variation is minimal, the primary factor to consider remains the pressure change, which significantly influences the performance of the PDE.

As previously illustrated, the initial conditions for the ROM input are derived using the Simulink® model. Specifically, in the case of an initial pressure of 10 bar and an initial temperature of 293.15 K, the corresponding ROM inputs are 9.70 bar and 293.42 K.
The remaining inputs, as discussed in Section 3.3, include the equivalence ratio $\phi$, tube length $L$, diameter $D$, and the relaxation time $t_{off}$. Once the ROM is implemented in MATLAB®, it becomes possible to analyse the variation in PDE performance with respect to different inputs and thereby determine the optimal configuration.
To ensure maximum performance, an initial pressure of 10 bar (equivalent to 9.70 bar at the ROM inlet) is used, as this provides the highest thrust, as shown in Figure 59. This was also confirmed by the CEA results presented in Chapter 2, making Figure 59 a validation of the implemented model.

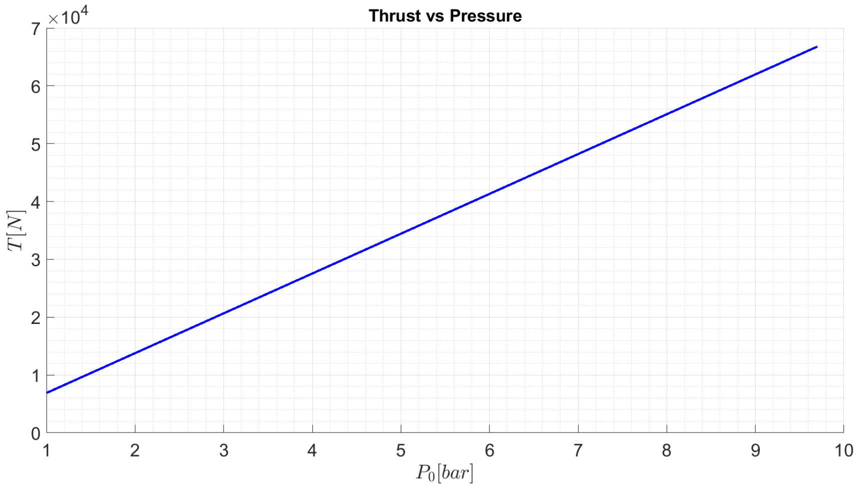

Figure 59: Maximum thrust as a function of initial pressure ($T_0 = 293.42$ K, $ER = 1.05$, $L = 0.66$ m, $D = 0.05$ m, $t_{off} = 0.005$ s) - MATLAB®

In this context, thrust is considered a more relevant performance parameter than specific impulse, as the latter remains nearly constant with pressure changes in a PDE, provided the propellant pair is fixed. This is demonstrated in Figure 60.

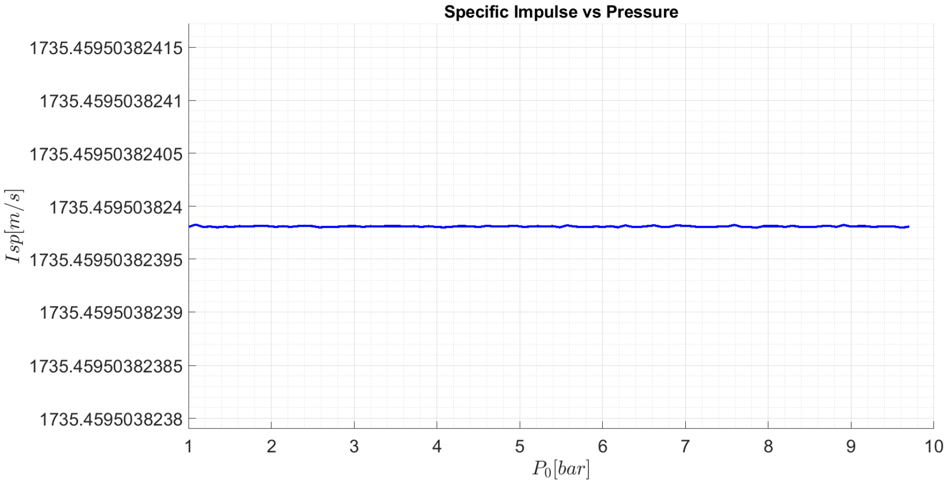

Figure 60: Specific impulse as a function of initial pressure ($T_0 = 293.42$ K, $ER = 1.05$, $L = 0.66$ m, $D = 0.05$ m, $t_{off} = 0.005$ s) - MATLAB®

To simplify both the problem and the experimental setup, the initial temperature is assumed to be the ambient one—293.15 K—corresponding to 293.42 K at the end of the feeding line. Nevertheless, the ROM suggests that a lower temperature (e.g., 250 K) would yield better performance.
With pressure and temperature fixed, the next step is to explore the optimal geometrical configuration for maximum thrust.

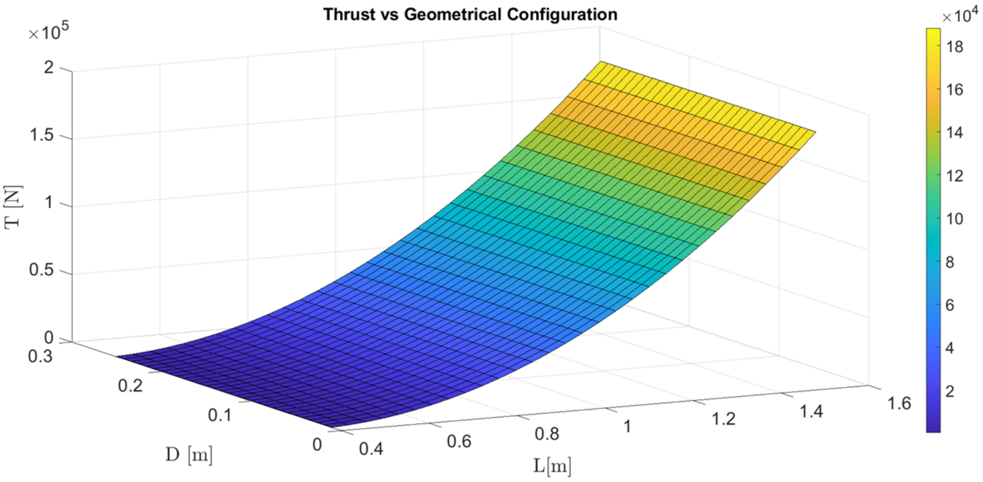

Figure 61: Maximum thrust as a function of geometrical configuration ($P_0 = 9.70$ bar, $T_0 = 293.42$ K, $ER = 1.05$, $t_{off} = 0.005$ s) - MATLAB®

This analysis assumes that distributed pressure losses—scaling with the detonation tube dimensions—are negligible compared to concentrated losses. The latter are considered constant across all configurations, since components such as valves, along the feeding line, remain identical in type and number regardless of the tube geometry. Distributed losses are on the order of Pascals, whereas concentrated losses reach magnitudes of $10^4$ Pa. Consequently, even with changes in $L$ and $D$, $P_0$ and $T_0$ are assumed constant.

As shown in Figure 61, the highest thrust is obtained with the longest tube. Thrust is not influenced by the tube diameter or the cut-off time $t_{off}$ since these are not modelled in the CFD simulation. However, practical constraints limit feasible configurations; pairing a long tube with a small diameter can lead to structural failure, such as buckling or cracking.
Similar to pressure effects, specific impulse remains unaffected by variations in $L$ and $D$ for a fixed propellant combination, so the corresponding plot is omitted.
To assign a suitable diameter for the optimal length of 1.5 m, experimental data are interpolated, as shown in Figure 62. The three data points correspond to configurations discussed in Chapter 2, Section 2.8.

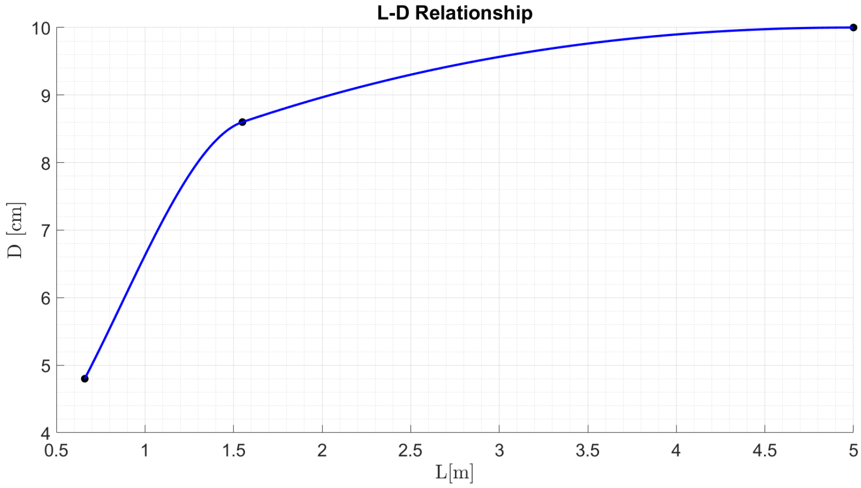

Figure 62: Tube diameter as a function of length - MATLAB®

From this interpolation, the diameter corresponding to $L = 1.5$ m is found to be 8.39 cm. The wall thickness, calculated using Equation (18) as in Section 2.8, is:

$$t = \frac{P_2 \times R}{\sigma_{\text{allow}}} \cdot \phi \times FS = \frac{18.04 \times 41.95}{792} \cdot 4 \times 3 = 11.47 \text{ mm} \tag{85}$$

According to the cost analysis (Figure 49), this configuration results in a cost of €137481,72. With these parameters defined, the remaining ones are the equivalence ratio and $t_{off}$. For $t_{off}$, which is external to the CFD model, a standard value of 0.005 s is adopted. $\phi$ is optimized following the same approach as the previous parameters.

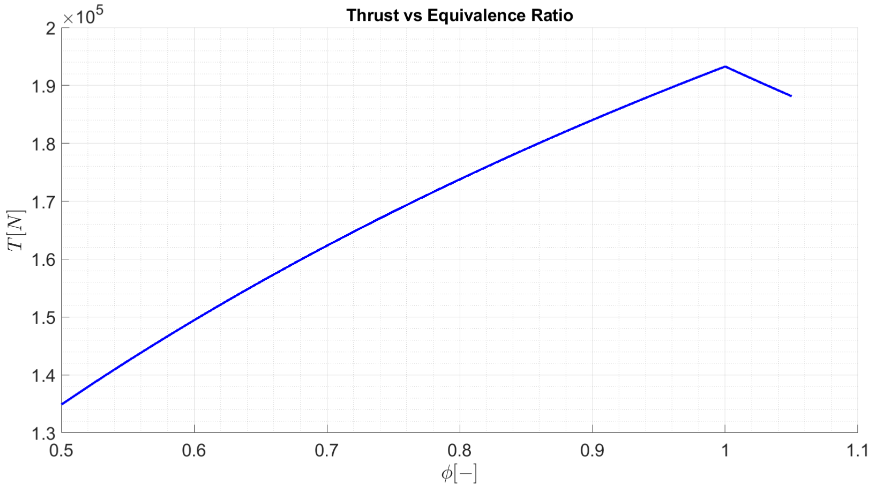

Figure 63: Maximum thrust as a function of equivalence ratio ($P_0 = 9.70$ bar, $T_0 = 293.42$ K, $L = 1.50$ m, $D = 0.0839$ m, $t_{off} = 0.005$ s) - MATLAB®

A similar trend is observed in specific impulse, shown in Figure 64.

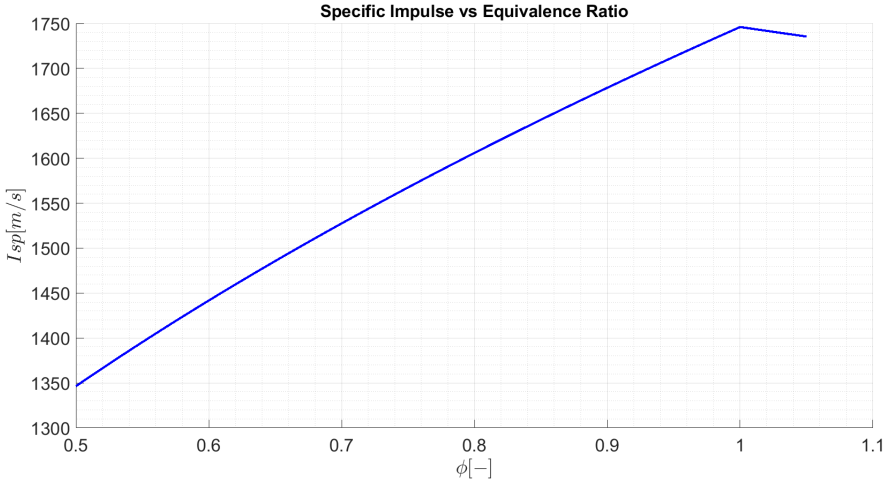

Figure 64: Specific impulse as a function of equivalence ratio ($P_0 = 9.70$ bar, $T_0 = 293.42$ K, $L = 1.50$ m, $D = 0.0839$ m, $t_{off} = 0.005$ s) - MATLAB®

In conclusion, the following input parameters are selected for maximum performance:

- $P_0 = 9.70$ bar;
- $T_0 = 293.42$ K;
- $L = 1.50$ m;
- $D = 0.0839$ m;
- $\phi = 1$;
- $t_{off} = 0.005$ s.

This configuration yields a maximum thrust of $1.933 \cdot 10^5 \pm 0.0387 \cdot 10^5$ N and a specific impulse of $1746.1 \pm 174.61$ m/s. The specific impulse (180 s) is comparable to that of hydrazine monopropellants, while the thrust greatly exceeds that of monopropellants (typi-

cally 0.5–500 N). Similar thrust levels are found in upper-stage liquid engines (e.g., LE-5B at 137 kN) or in the Pratt & Whitney F135 engine (191 kN). It should be noted, however, that the thrust generated by a PDE is not continuous, as illustrated in Figure 69, resulting in a substantially lower average thrust.
The fuel-based specific impulse is 6171.2 s, consistent with literature (see Figure 7).
If the feeding line is not modeled, and ideal inlet conditions ($P_0 = 10$ bar, $T_0 = 293.15$ K) are used, keeping all other parameters fixed, the resulting performance is:

- Specific impulse $I_{sp}$ = 1746.1 ±174.61 m/s;
- Maximum thrust $T = 1.994 \cdot 10^5 \pm 0.0399 \cdot 10^5$ N.

Thus, specific impulse remains unaffected, while thrust decreases by 3.1% due to pressure losses.

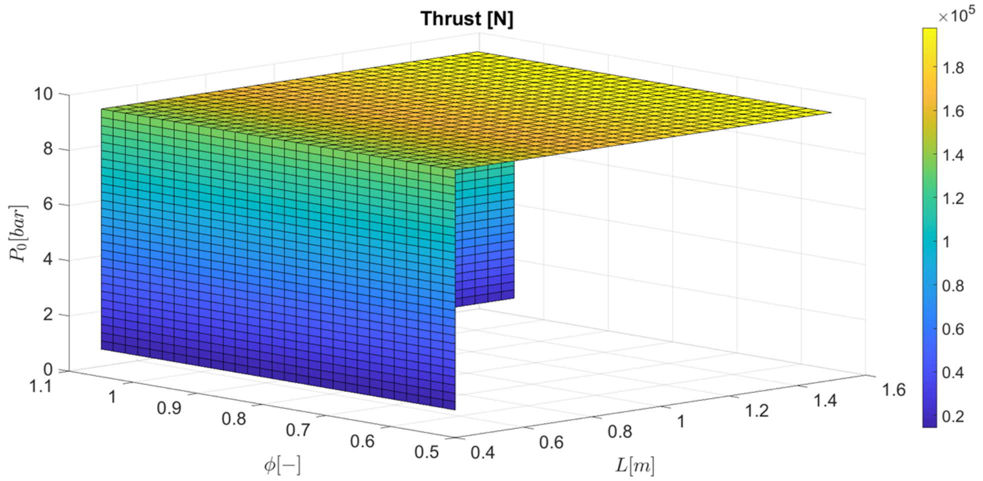

Figure 65: Thrust as a function of $P_0$, $\phi$, and $L$ ($T_0 = 293.42$ K, $D = 0.0839$ m, $t_{off} = 0.005$ s) - MATLAB®

Figure 65 demonstrates that the maximum thrust is achieved when $P_0$ and $L$ are at their maximum values and $\phi = 1$. This confirms that analysing each parameter individually or varying them simultaneously leads to the same optimal configuration, indicating consistency in the optimization approach.

With the configuration now fixed, the transient behaviour of key parameters can be observed using the ROM:

- pressure: Figure 66;
- temperature: Figure 67;
- density: Figure 68;
- thrust: Figure 69;
- mass flow rate: Figure 70.

The peaks in these plots correspond to the moment the flow reaches Mach 1.

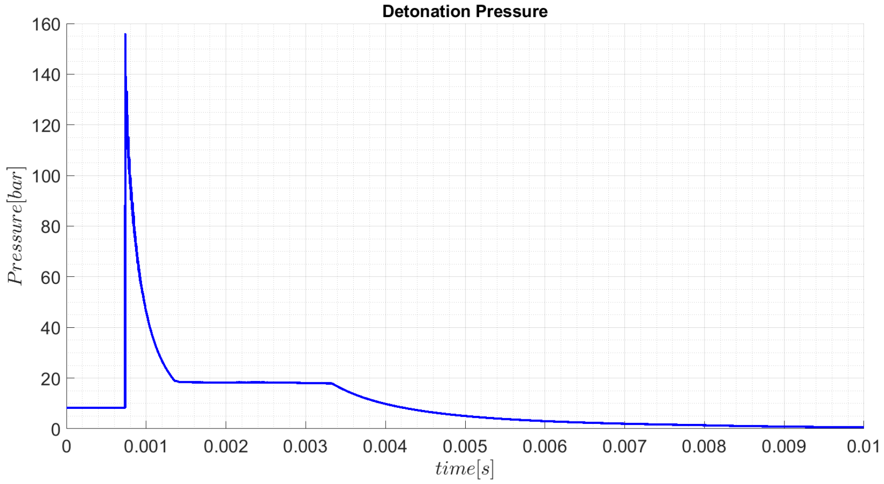

Figure 66: Pressure during the detonation process as a function of time ($P_0 = 9.70$ bar, $T_0 = 293.42$ K, $L = 1.50$ m, $D = 0.0839$ m, $\phi = 1$, $t_{off} = 0.005$ s) - MATLAB®

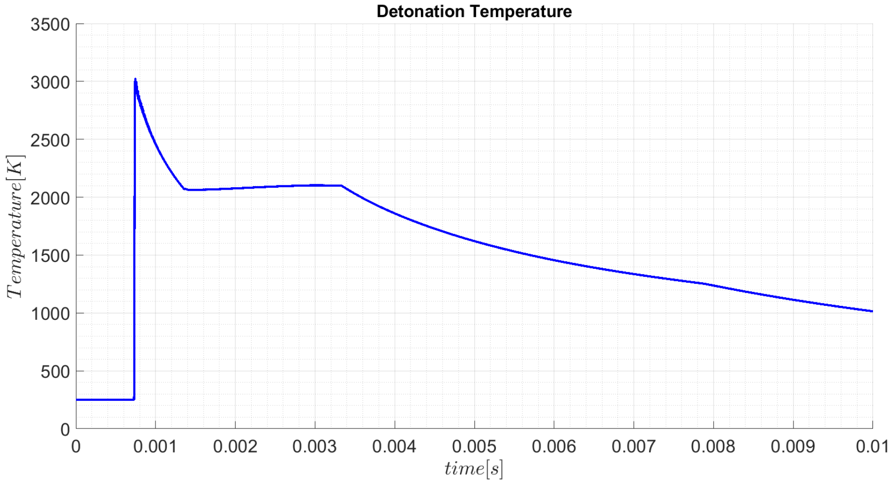

Figure 67: Temperature during the detonation process as a function of time ($P_0 = 9.70$ bar, $T_0 = 293.42$ K, $L = 1.50$ m, $D = 0.0839$ m, $\phi = 1$, $t_{off} = 0.005$ s) - MATLAB®

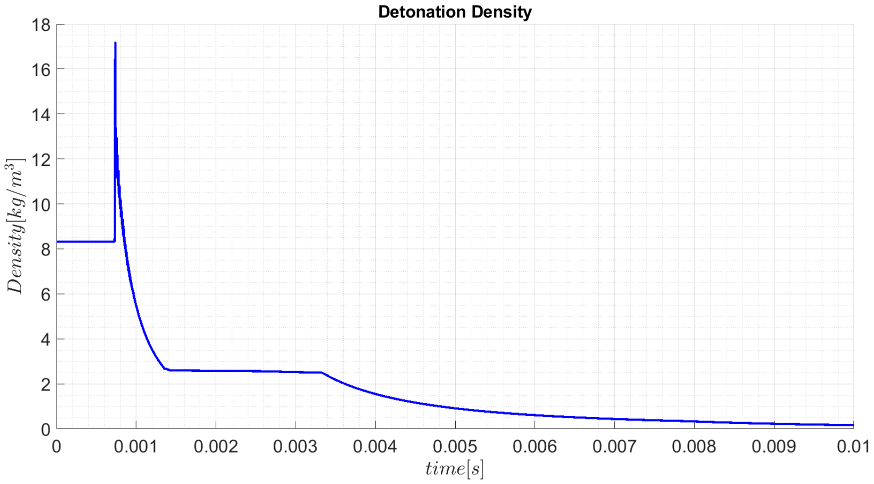

Figure 68: Density during the detonation process as a function of time ($P_0 = 9.70$ bar, $T_0 = 293.42$ K, $L = 1.50$ m, $D = 0.0839$ m, $\phi = 1$, $t_{off} = 0.005$ s) - MATLAB®

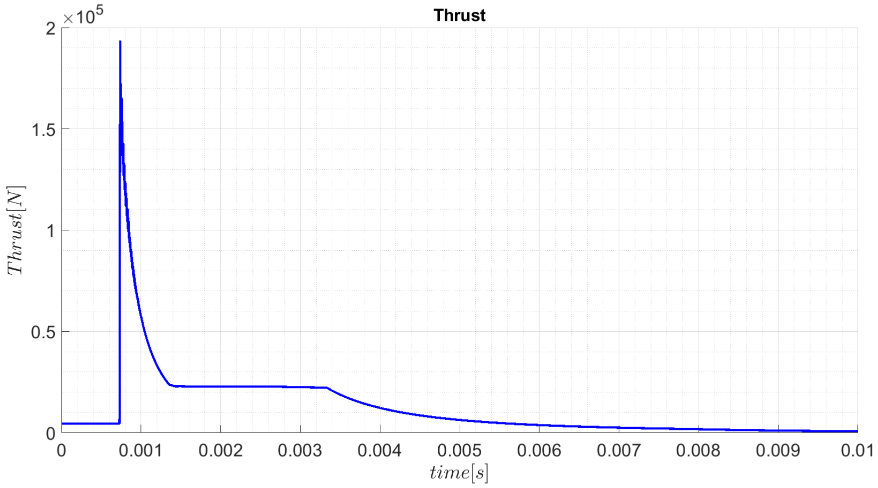

Figure 69: Thrust during the detonation process as a function of time ($P_0 = 9.70$ bar, $T_0 = 293.42$ K, $L = 1.50$ m, $D = 0.0839$ m, $\phi = 1$, $t_{off} = 0.005$ s) - MATLAB®

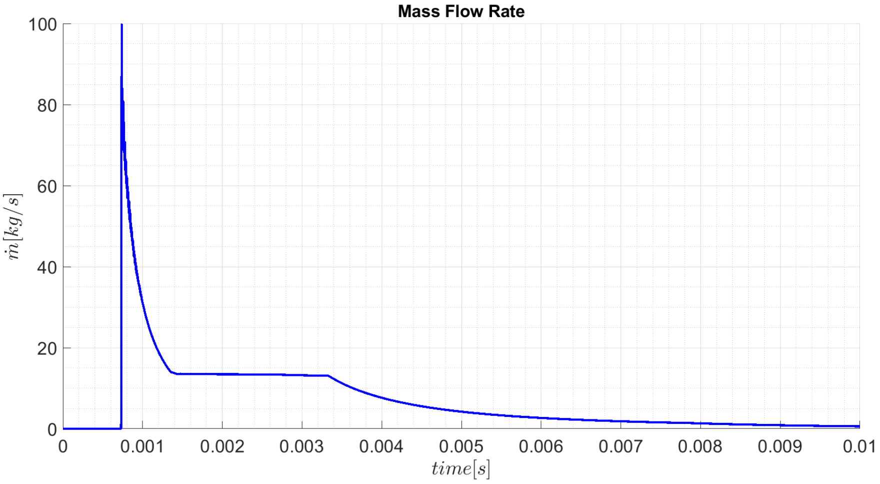

Figure 70: Mass flow rate during the detonation process as a function of time ($P_0 = 9.70$ bar, $T_0 = 293.42$ K, $L = 1.50$ m, $D = 0.0839$ m, $\phi = 1$, $t_{off} = 0.005$ s) - MATLAB®

The working frequency is 83.4 Hz: therefore there is one detonation every 0.01 s, which is the time range of the previous plots. The trend depicted in the plots perfectly align with the phases already described:

- filling : at the beginning;
- ignition : the detonation wave happens in correspondence of the peak found in the figures;
- exhaust : the pressure, and so as the other variables, decreases;
- purging : $N_2$ injected to purge combustion products and prepare for the next cycle.

## 3.5 Validation Of The Results

The verification of the pressure at the end of the feeding line was already carried out in Section 3.4 by comparing the simulation results obtained from Simulink® with the component

data provided in the respective datasheets.
The current focus is on validating the results of the plots generated in MATLAB®, by comparing them with findings from previous studies in the literature.

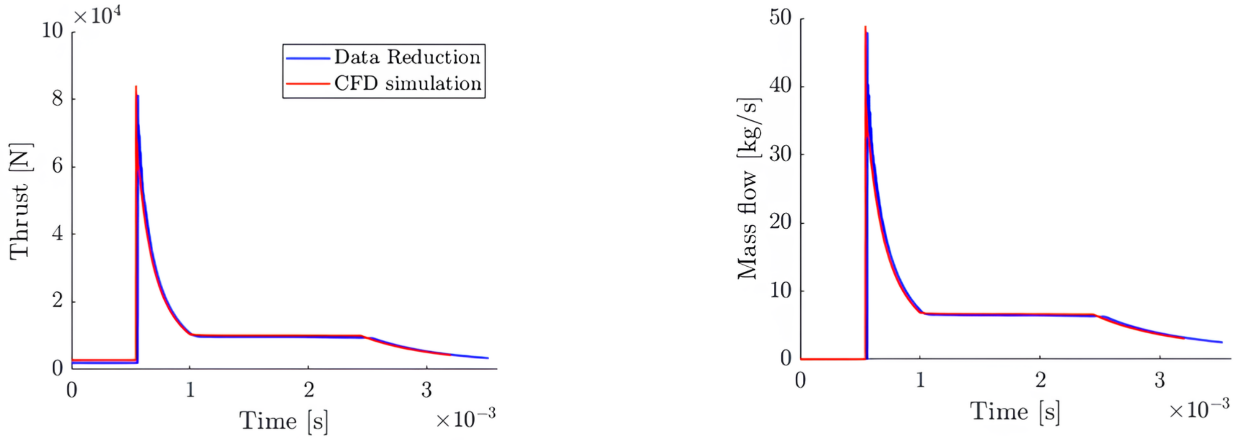

(a) Thrust over time

(b) Mass flow rate over time

Figure 71: Comparison of time evolution of thrust and mass flow rate: data reduction vs CFD. $P_0 = 7.30$ bar, $T_0 = 307$ K, $L = 1$ m, $D = 0.07$ m, $\phi = 0.7$, $t_{off} = 0.071$ s [36]

The trends in Figure 71 exhibit lower values for both thrust and mass flow rate compared to those from the simulations. This discrepancy arises from the fact that the input parameters used in this case are not optimized. Nevertheless, the overall behavior is consistent with the trends reported in other studies from the literature [72] [73] [74].
With the trends now validated, the next step is to confirm the numerical values. This is achieved using NASA's CEA program, which allows the evaluation of whether peak values of temperature, pressure and density are consistent.

| Property | Value |
|---|---|
| $v_{detonation}[m/s]$ | 2007.2 |
| $P_2/P_1$ | 16.3 |
| $T_2/T_1$ | 10.5 |
| $\rho_2/\rho_1$ | 1.8 |

Table 20: CEA results for $H_2$/air mixture at 9.70 bar and 293.42 K

The following table provides a comparison between the CEA results and the numerical simulation data for the same initial conditions:

| Parameter | Simulation | CEA |
|---|---|---|
| $P_{max}$ [bar] | 155.8 | 158.6 |
| $T_{max}$ [K] | 3022.8 | 3086.2 |
| $\rho_2/\rho_1$ | 2.1 | 1.8 |

Table 21: Comparison between CEA and simulation results for $H_2$/air mixture at 9.70 bar and 293.42 K

The results show good agreement with the CEA predictions, thus confirming the validity of the simulation outputs. Minor discrepancies (e.g., 1.8% for $P_{max}$) can be attributed to the differences in the models used, which involve simplifications in describing the detonation process. These differences remain within the range reported in the literature [4].
As shown in Figure 71, the values of thrust and mass flow rate have already been validated. Similarly, the specific impulse and the fuel-based specific impulse are consistent with values reported in the literature (Figure 7, [75] [76] [77]).

## 3.6 Conclusions and Future Developments

The initial objective of designing an experimental setup capable of being adapted into an RDE is achieved through specific design choices, such as the adoption of piezoresistive transducers in place of piezoelectric ones.
Innovations over previous experimental configurations are introduced to enhance measurement accuracy and precision and to reduce the likelihood of process-related errors. These innovations include:

1. use of ion sensors;
2. load cell configuration without a spring-damper system;
3. high-resolution camera;
4. application of the BOS technique instead of traditional Schlieren methods;
5. use of a rotary valve for fuel injection instead of a solenoid valve, enabling higher-frequency operation.

In addition to the sensors used for measuring mass flow rate, temperature, pressure, acceleration, and force, several safety measures are incorporated:

- flashback arrestors to prevent flame propagation;
- check valves to avoid backflow;
- flow nozzle to regulate flow rates;
- emergency shutdown system to halt injection and ignition in the event of overpressure, premature detonation, or fuel leakage;
- EMI shielding to ensure data integrity within the data acquisition system;
- open-loop water cooling system;
- nitrogen purge system to prevent premature ignition of the fuel–air mixture.

A Shchelkin spiral is selected to promote DDT, as it offers an optimal balance between energy efficiency and weight.
Contingency measures are also considered. If water cooling proves insufficient during testing, additional solutions such as film cooling may be implemented.
The cost analysis is based on the selected components and the quantity required for setups of various dimensions. A cost trend plot is created by interpolating data from three configurations documented in previous experiments (Figure 49). This plot assists in selecting system dimensions based on budget constraints, while Figure 61 guides dimensioning based on desired performance levels.
After selecting the components, a Simulink® model is developed to account for non-idealities

introduced by components in the feed system, such as check valves and flashback arrestors. A key output of this model is the temperature and pressure of the propellant at the end of the feed line, just before entering the detonation tube. The pressure losses introduced by these components result in a thrust reduction of approximately 3.1% under an inlet pressure of 10 bar, and this effect must be considered.

A ROM developed by Universidad Politécnica de Madrid is employed. It exhibits a deviation of approximately 10% from high-fidelity CFD results, which is deemed acceptable for preliminary design phases. Using a dimensionless analysis, the ROM enables evaluation of propulsive parameters such as specific impulse and thrust. Input parameters are optimized to maximize performance, with the best results obtained using maximum pressure and detonation tube length, and a stoichiometric fuel–air mixture. The tube diameter is chosen based on interpolation of three configurations from past experiments, as shown in Figure 62.

The resulting optimized configuration yields a maximum thrust of $1.933 \cdot 10^5 \pm 0.0387 \cdot 10^5$ N and a specific impulse of $1746.1 \pm 174.61$ m/s. The total cost of this configuration is €137481,72.

The developed model serves as a predictive and diagnostic tool during the experimental campaign. It allows for anticipating the expected range of values and validating experimental results. In case of discrepancies, the simulation model can be updated accordingly. This work provides a scalable and modular foundation for future propulsion testbeds, contributing to the technological readiness of PDE and RDE systems for aerospace and defense applications.

Validation is performed by comparison with literature references, including analytical models, CFD results, experimental data and NASA's CEA code. The observed discrepancies are within acceptable limits and are attributed to simplifying assumptions such as using a one-dimensional model to approximate inherently three-dimensional shockwave structures and considering perfect mixing.

The specific impulse of the optimized configuration is comparable to that of hydrazine monopropellants, while thrust levels are similar to those of upper-stage liquid engines (e.g., the LE-5B at 137 kN) and military-grade engines such as the Pratt & Whitney F135 (191 kN). It should be noted that the reported performance values are obtained without the inclusion of a nozzle. The addition of a nozzle would further increase both thrust and specific impulse. Consequently, future work should focus on determining the optimal nozzle configuration (type, area ratio) to maximize performance.

Next steps include the physical construction of the test rig, integration of advanced diagnostics during experimental trials and detailed performance testing to validate the numerical predictions under real detonation cycles.

Moreover, since a PDE generates thrust intermittently, the average thrust over time is significantly lower. In contrast, an RDE produces continuous thrust, leading to substantially improved performance. Specific impulses as high as 3600 s—comparable to electric and plasma propulsion systems—have been reported for RDEs [78].

This is why RDEs represent a highly attractive propulsion solution, and the current experimental setup is purposefully designed to allow conversion to RDE operation with minimal modifications and additional cost, once PDE behaviour is fully characterized.

By laying the groundwork for an RDE-compatible PDE testbed, this thesis bridges theoretical propulsion concepts with practical implementation, advancing the state of the art in detonation-based propulsion research.

# A Chapter 3 Appendix: Simulink model

**Motor TS4613 Subsystem** Key Components of the Motor System (Figure 53):

- Power source - **Three-Phase Source** block: provides the grid input to the system, simulating a standard utility network. Both voltage and frequency can be adjusted in this block. According to the motor's datasheet, the input voltage is set to 200 V [26].
- Measurement Block – vi Subsystem: measures phase voltage and current from the source, as shown in Figure 72.

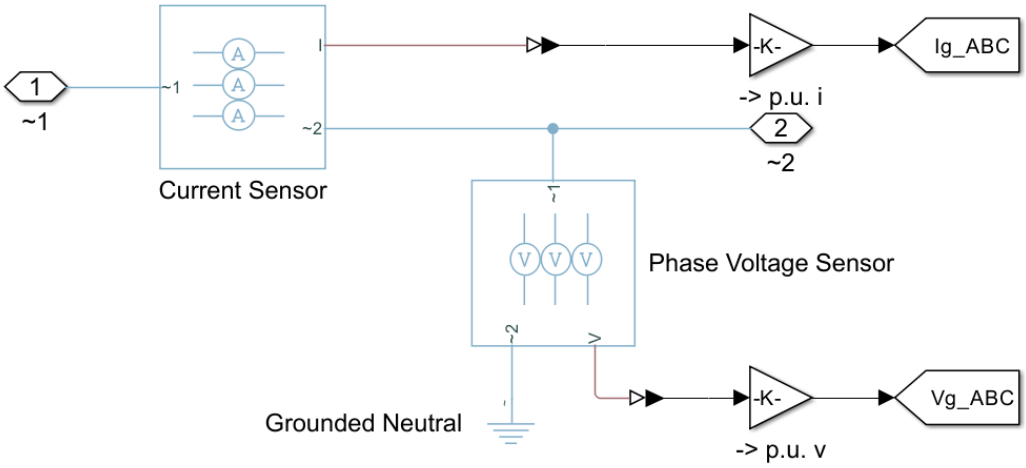

Figure 72: vi Subsystem inside Motor TS4613 Subsystem - Simulink®

It provides signals for the **PLL** and power regulation blocks. A similar subsystem, **vi abc**, outputs the signals $I\_ABC$ and $V\_ABC$.

- Grid-Side Converter (GSC): implemented in the Motor Controls subsystem (Figure 73), it maintains a stable DC-link voltage regardless of transient power demands from the motor side.
  The GSC is modeled as a three-phase voltage source converter, using vector (field-oriented) control in the rotating d-q reference frame. It operates in sensorless mode, dynamically regulating active and reactive power exchange with the grid, using cascaded control loops (outer voltage, inner current). Its internal structure (Figure 74) includes:

  1. Voltage regulator (PI);
  2. Current regulator (d/q);
  3. dq0 to abc modulation;
  4. PWM Generator.

  The reference value of the link voltage, $Vdc_{ref}$, must be at least 1.2 times higher than the AC RMS voltage. For a 200 V motor, 350 V is selected.

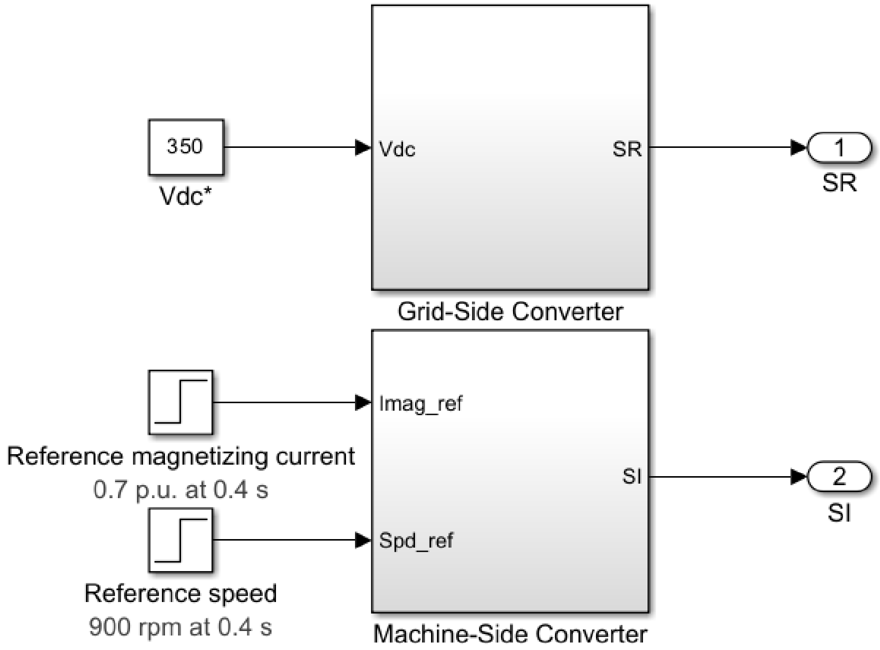

Figure 73: Motor Controls Subsystem inside Motor TS4613 Subsystem - Simulink®

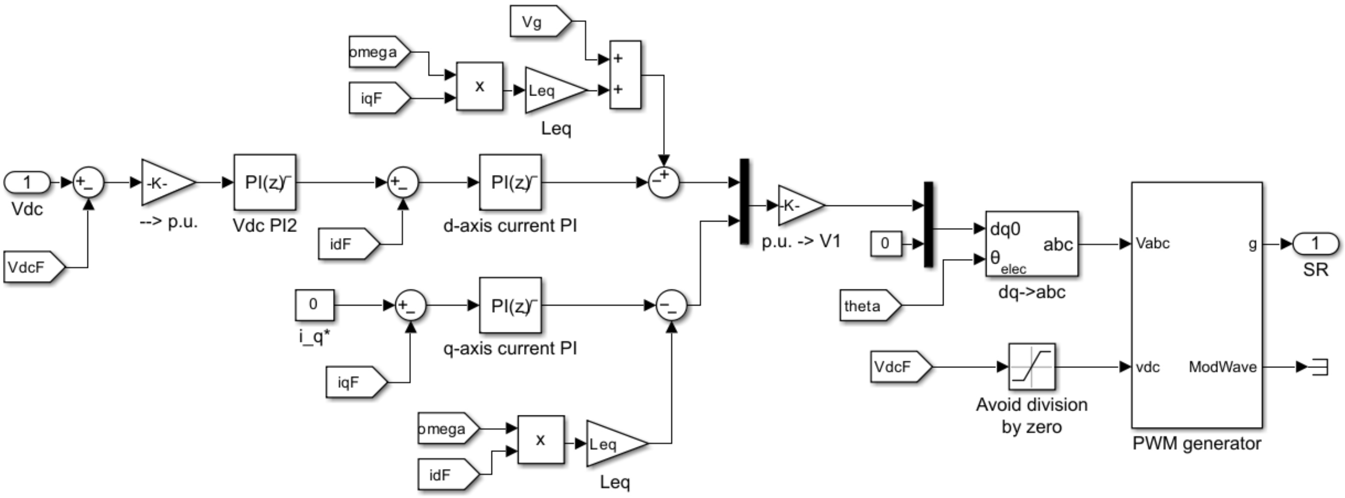

Figure 74: Grid-Side Converter Subsystem inside Motor Controls Subsystem- Simulink®

- Machine-Side Converter (MSC): converts DC into AC to drive the induction motor, as shown in Figure 75.
  It performs speed and torque control via:
  1. dq0 transformations;
  2. PI current regulators;
  3. PWM modulation.

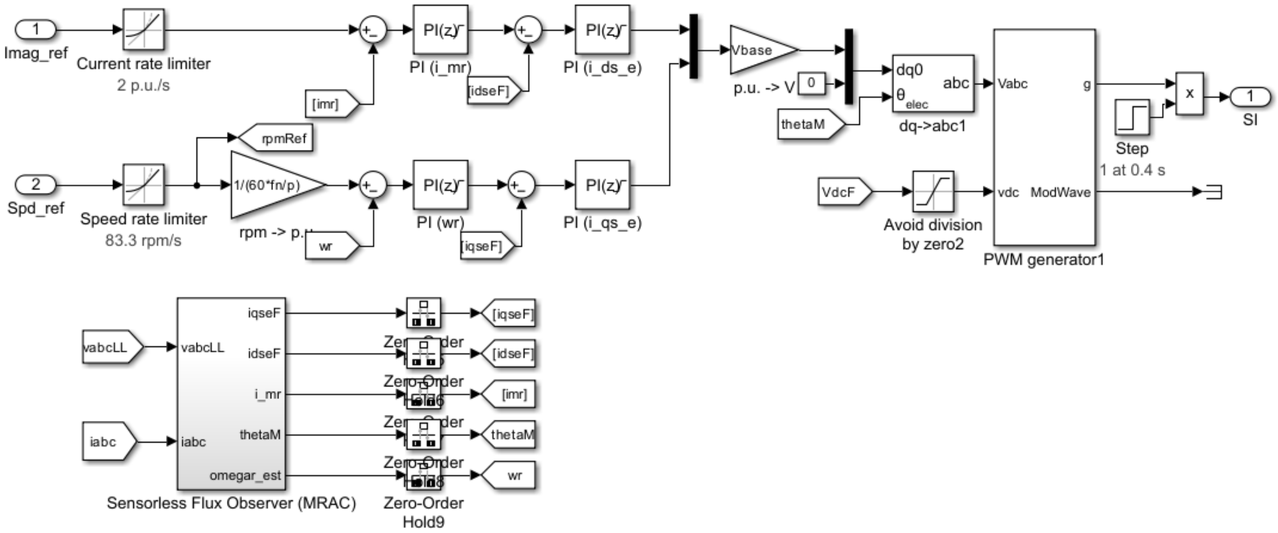

Figure 75: Machine-Side Converter Subsystem inside Motor Controls Subsystem - Simulink®

The MSC regulates the torque and flux of the induction machine by controlling the stator currents in the synchronous rotating $dq$ frame. Figure 75 shows the internal structure of the MSC control system, including current loops, speed controller and a sensorless flux observer. Control inputs include:

- Imag_ref – the magnetizing current reference (typically 0.6 to 0.9 p.u.), which defines the flux linkage;
- Spd_ref – the mechanical speed reference, in rpm (3000 rpm for 200 Hz).

A **Current Rate Limiter** and **Speed Rate Limiter** blocks prevent abrupt changes by applying ramp limits of 2 p.u./s and 83.3 rpm/s respectively. The latter corresponds to the maximum rotational speed of the motor of 5000 rpm/min [26].

A **Model Reference Adaptive Control (MRAC)** flux observer estimates the rotor flux, speed and angle:

- inputs: stator voltages $v_{abc}$ and currents $i_{abc}$;
- outputs: $\hat{i}_{ds}, \hat{i}_{qs}, \hat{\psi}_r, \theta_M, \omega_r$.

Zero-order hold blocks ensure synchronization with the control sampling rate.

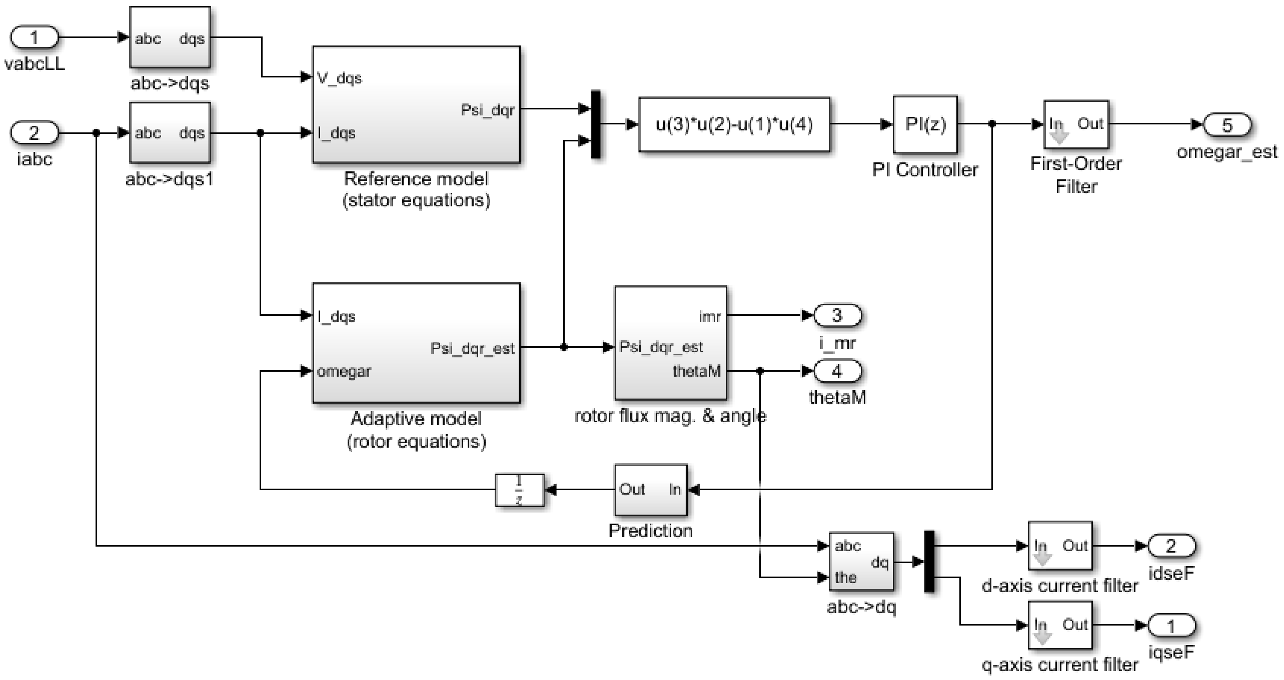

Figure 76: Sensorless Flux Observer (MRAC) Subsystem - Simulink®

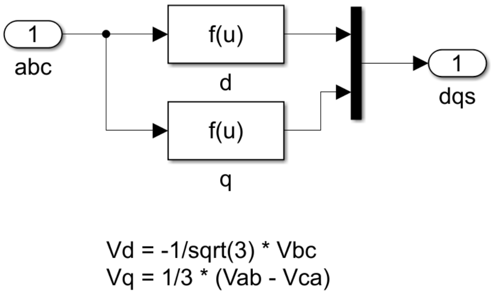

Figure 77: abc→dqs subsystem of Sensorless Flux Observer (MRAC) Subsystem - Simulink®

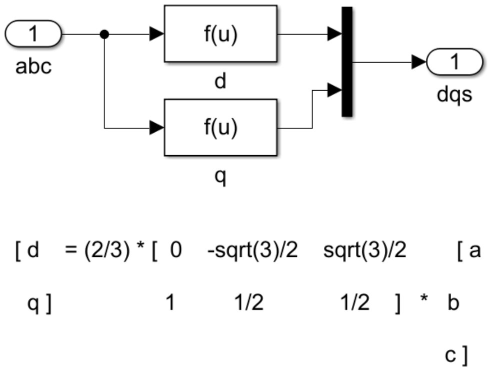

Figure 78: abc→dqs1 subsystem of Sensorless Flux Observer (MRAC) Subsystem - Simulink®

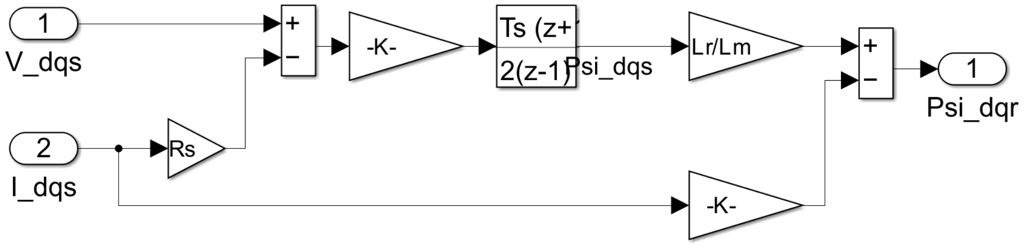

Figure 79: Reference model (stator equations) subsystem of Sensorless Flux Observer (MRAC) Subsystem - Simulink®

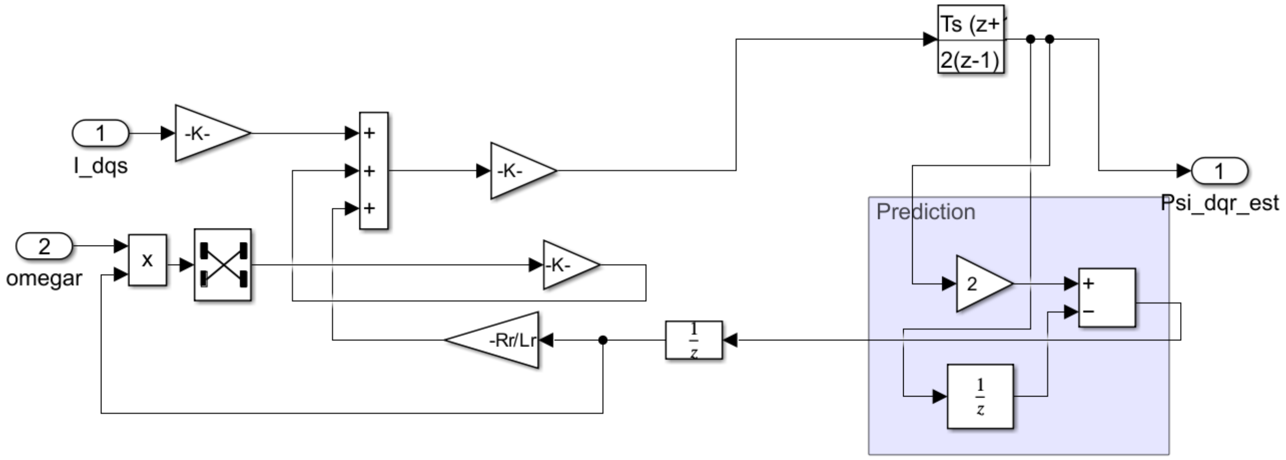

Figure 80: Adaptive model (rotor equations) subsystem of Sensorless Flux Observer (MRAC) Subsystem - Simulink®

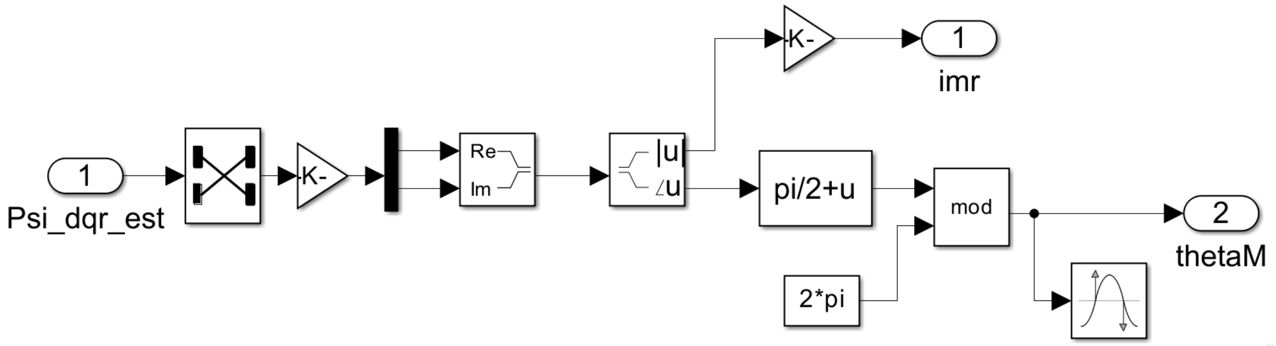

Figure 81: Rotor flux mag. & angle subsystem of Sensorless Flux Observer (MRAC) Subsystem - Simulink®

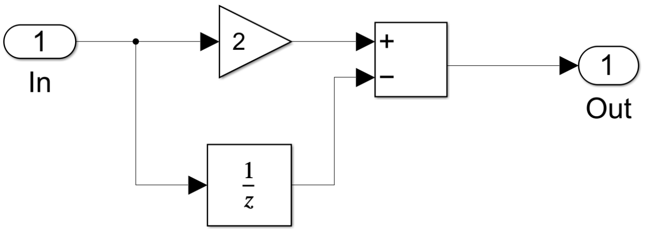

Figure 82: Prediction subsystem of Sensorless Flux Observer (MRAC) Subsystem - Simulink®

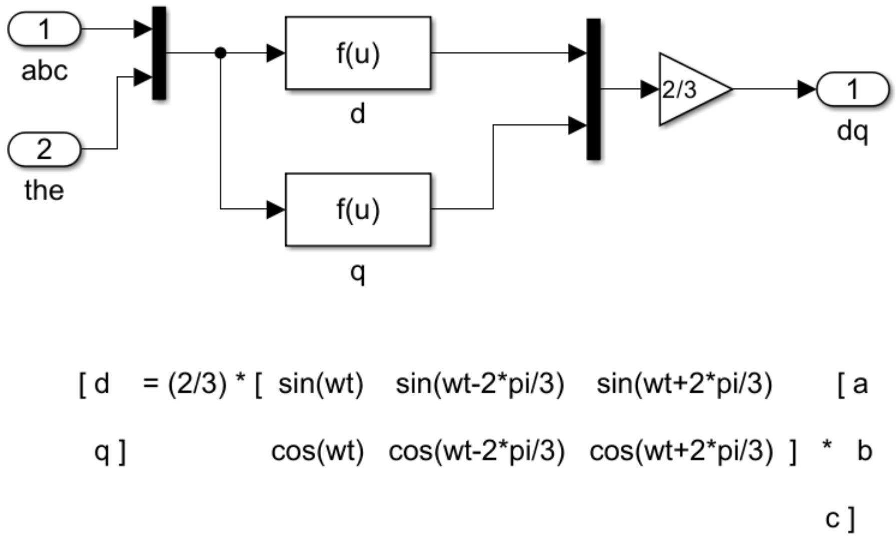

$$\begin{bmatrix} d \\ q \end{bmatrix} = (2/3) * \begin{bmatrix} \sin(wt) & \sin(wt-2*pi/3) & \sin(wt+2*pi/3) \\ \cos(wt) & \cos(wt-2*pi/3) & \cos(wt+2*pi/3) \end{bmatrix} * \begin{bmatrix} a \\ b \\ c \end{bmatrix}$$

Figure 83: abc→dq subsystem of Sensorless Flux Observer (MRAC) Subsystem - Simulink®

- Induction Motor – **Three-Phase Asynchronous Machine (Sensorless)**
  - Block: **Asynchronous Machine SI Units**;
  - Sensorless control: uses flux estimation;
  - Connected to a **Inertia** block representing the rotary valve disk.
- Mechanical Load - **Inertia** block: models the inertia of the rotary valve. The value of the inertia is calculated from:

$$\begin{aligned} J = \frac{1}{2}mr^2 = \frac{1}{2} \cdot \left(\rho \pi r^2 h\right) r^2 \\ = \frac{1}{2} \cdot 8000 \cdot \pi \cdot (0.0463)^2 \cdot 0.0093 \cdot (0.0463)^2 = 5.37 \times 10^{-4}\,\mathrm{kg} \cdot \mathrm{m}^2 \end{aligned} \tag{86}$$

- Mechanical Load - **Ideal Torque Source** + **PS Constant** blocks: apply constant mechanical torque (0.45 $N \cdot m$ as stated in Chapter 2) as resistive load. A constant torque is appropriate for evaluating stationary performance of a rotating valve.
- Mechanical Load - **Machine Inertia** block : to simulate the inertia of the motor, which is specified in the datasheet of the TS4613 as $0.86 \cdot 10^{-4}$ kg·m$^2$ [26].
- Motion Sensor and Angle Estimation - **Motion Sensor** block: measures angular speed and position. **Angle sensor** block is used to generate the valve opening pattern via angle comparison logic.
- Control System – Motor Controls Subsystem (Figure 73):
  - Manages references for:
    1. speed ($Spd_{ref}$);
    2. magnetizing current ($Imag_{ref}$);
    3. DC voltage ($Vdc_{ref}$).
  - Connects to both:
    1. MSC controller;

2. GSC controller.

- Inputs:
  1. $Spd_{ref}$ = 3000 rpm for 200 Hz (as discussed in the rotary valve section, see Section 2.5.2). The value is scaled proportionally for different frequencies;
  2. $Imag_{ref}$ = 0.7 p.u.;
  3. $Vdc_{ref}$ : at least 1.2 times greater than the AC RMS voltage.

- The Measurements subsystem is responsible for acquiring and converting electrical and mechanical quantities necessary for asynchronous motor control. Its structure is shown in Figure 84.

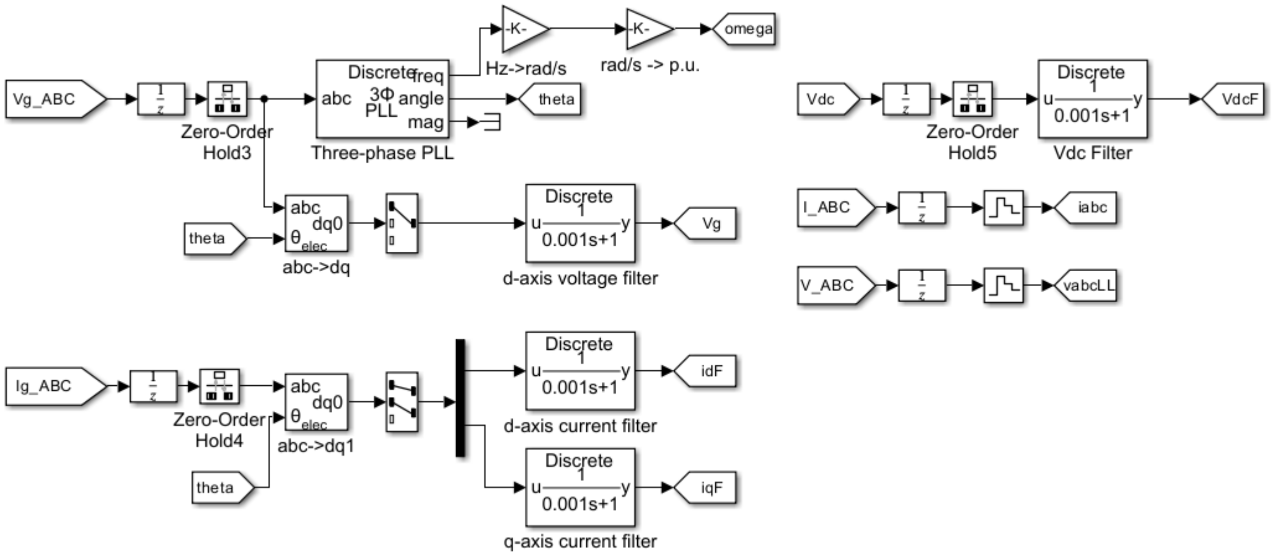

Figure 84: Motor measurements Subsystem inside Motor TS4613 Subsystem - Simulink®

- Functions:

| Task | Output |
|---|---|
| Estimate rotor angle | $\theta$ |
| Estimate electrical speed | $\omega$ (rad/s) |
| Filter DC link voltage | `VdcF` |
| Extract d/q currents (grid side) | `idF, iqF` |
| Provide phase voltages and currents | `V_ABC, I_ABC` |

Table 22: Outputs of the Motor measurements Subsystem inside Motor TS4613 Subsystem - Simulink®

- Main Sections:
  1. PLL Section (Grid Synchronization):
     * input: $Vg_{ABC}$ (three-phase grid voltages);
     * performs **abc** → **dq** transformation using the rotor angle $\theta$;

    - the **PLL** block extracts the grid frequency (Hz) and computes the electrical angle $\theta$;
    - converts frequency from Hz to rad/s and then to p.u. for control use.
  2. Filtering Section:
    - applies first-order filters (H(s) = 1/(0.001s + 1)) to voltages and currents;
    - ensures smoothed signals for the PI controllers.
  3. Pass-through Section: transfers raw $V_{ABC}$ and $I_{ABC}$ for monitoring and visualization.

- The Scopes subsystem contains visual monitoring tools for key electrical and mechanical quantities, as shown in Figure 85. The monitored signals are:
  1. `VdcF`, `Vdc`: filtered and unfiltered DC-link voltage;
  2. `Vg x idF`: active power from the grid;
  3. `omegaR`: actual rotor speed;
  4. $Ig_{ABC}$, $Vg_{ABC}$: grid-side currents and voltages of the asynchronous motor;
  5. $I\_ABC$ : three-phase stator currents;
  6. $Te$ : electromagnetic torque;
  7. omegar : rotor speed (converted to rpm).

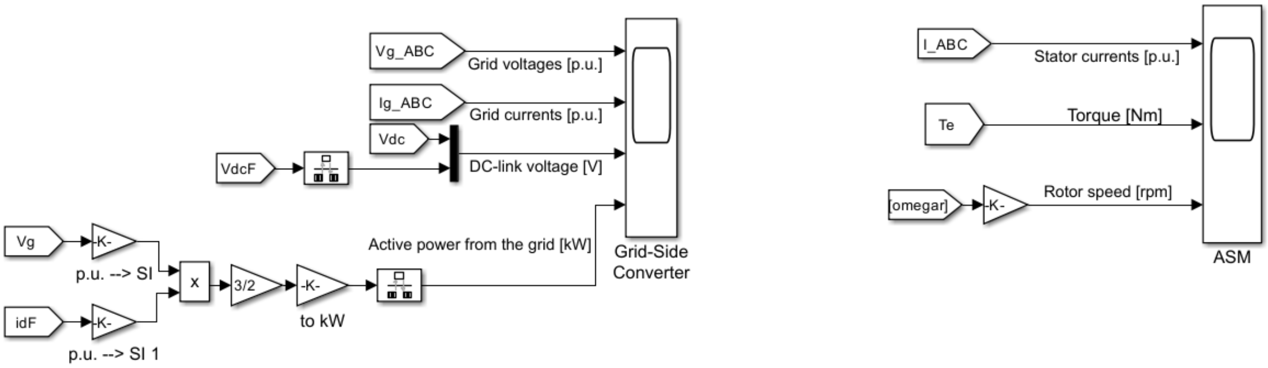

Figure 85: Motor Scopes Subsystem inside Motor TS4613 Subsystem - Simulink®

These scopes are used solely to verify the correct functioning of the motor. As they are not essential to the main objectives of this work, they will not be further analysed.

**Reduced Order Model** The reactions used are listed in Table 23.

| **Reaction** | **Arrhenius Parameters (A, b, $E_a$)** |
|---|---|
| $OH + H_2 \rightleftharpoons H + H_2O$ | $2.14 \cdot 10^{8}, 1.52, 3449.0$ |
| $O + OH \rightleftharpoons O_2 + H$ | $2.02 \cdot 10^{14}, -0.4, 0.0$ |
| $O + H_2 \rightleftharpoons OH + H$ | $5.06 \cdot 10^{4}, 2.67, 6290.0$ |
| $H + O_2\ (+M) \rightleftharpoons HO_2\ (+M)$ | $4.52 \cdot 10^{13}, 0.0, 0.0$ |
| $H + O_2\ (+N_2) \rightleftharpoons HO_2\ (+N_2)$ | $4.52 \cdot 10^{13}, 0.0, 0.0$ |
| $H + O_2\ (+H_2) \rightleftharpoons HO_2\ (+H_2)$ | $2.03 \cdot 10^{20}, -1.59, 0.0$ |
| $H + O_2\ (+H_2O) \rightleftharpoons HO_2\ (+H_2O)$ | $1.52 \cdot 10^{19}, -1.133, 0.0$ |
| $OH + HO_2 \rightleftharpoons H_2O + O_2$ | $2.10 \cdot 10^{23}, -2.437, 0.0$ |
| $OH + HO_2 \rightleftharpoons H_2O + O_2$ | $9.10 \cdot 10^{14}, 0.0, 10964.0$ |
| $H + HO_2 \rightleftharpoons OH + OH$ | $1.50 \cdot 10^{14}, 0.0, 1000.0$ |
| $H + HO_2 \rightleftharpoons H_2 + O_2$ | $8.45 \cdot 10^{11}, 0.65, 1241.0$ |
| $H + HO_2 \rightleftharpoons O + H_2O$ | $3.01 \cdot 10^{13}, 0.0, 1721.0$ |
| $O + HO_2 \rightleftharpoons O_2 + OH$ | $3.25 \cdot 10^{13}, 0.0, 0.0$ |
| $OH + OH \rightleftharpoons O + H_2O$ | $3.57 \cdot 10^{4}, 2.4, -2112.0$ |
| $H + H + M \rightleftharpoons H_2 + M$ | $1.00 \cdot 10^{18}, -1.0, 0.0$ |
| $H + H + H_2 \rightleftharpoons H_2 + H_2$ | $9.20 \cdot 10^{16}, -0.6, 0.0$ |
| $H + H + H_2O \rightleftharpoons H_2 + H_2O$ | $6.00 \cdot 10^{19}, -1.25, 0.0$ |
| $H + OH + M \rightleftharpoons H_2 + M$ | $2.21 \cdot 10^{22}, -1.25, 0.0$ |
| $H + O + M \rightleftharpoons OH + M$ | $4.71 \cdot 10^{18}, -1.0, 0.0$ |
| $O + O + M \rightleftharpoons O_2 + M$ | $1.89 \cdot 10^{13}, 0.0, -1788.0$ |
| $HO_2 + HO_2 \rightleftharpoons H_2O_2 + O_2$ | $4.20 \cdot 10^{14}, 0.0, 11982.0$ |
| $HO_2 + HO_2 \rightleftharpoons H_2O_2 + O_2$ | $1.30 \cdot 10^{11}, 0.0, -1629.0$ |
| $OH + OH\ (+M) \rightleftharpoons H_2O_2\ (+M)$ | $3.04 \cdot 10^{30}, -4.63, 2049.0$ |
| $H_2O_2 + H \rightleftharpoons HO_2 + H_2$ | $1.98 \cdot 10^{6}, 2.0, 2435.0$ |
| $H_2O_2 + H \rightleftharpoons OH + H_2O$ | $3.07 \cdot 10^{13}, 0.0, 4217.0$ |
| $H_2O_2 + O \rightleftharpoons OH + HO_2$ | $9.55 \cdot 10^{6}, 2.0, 3970.0$ |
| $H_2O_2 + OH \rightleftharpoons H_2O + HO_2$ | $2.40 \cdot 10^{0}, 4.042, -2162.0$ |

Table 23: Arrhenius coefficients for the $H_2$-air reaction mechanism based on Marinov et al. [38]. Units are in s, mol, $cm^3$, cal, and K, respectively

# References

[1] S. R. Turns. An introduction to combustion, 2000.

[2] M.L. Coleman. Overview of pulse detonation propulsion technology, 2001.

[3] J. T. Peace and F. K. Lu. Performance modeling of pulse detonation engines using the method of characteristics. 2019.

[4] M. Warimani, M. H. Azami, S. A. Khan, A. F. Ismail, S. Saharin, and A. K. Ariffin. Internal flow dynamics and performance of pulse detonation engine with alternative fuels. Technical report, 2021.

[5] Y. Wang and J. Wang. Coexistence of detonation with deflagration in rotating detonation engines. 2016.

[6] THK. Thk ssr20 xwqzss bearings. https://www.motion.com/products/sku/01488117, 2025.

[7] Nikai. Aluminum plate. https://nikaisl.com/producto/accesorios/, 2025.

[8] D. D. Joshi and F. K. Lu. Unsteady thrust measurement for pulse detonation engines. 2015.

[9] M. R. Haghdoost, B. S. Thethy, D. E.-Mitchell, F. Habicht, J. Vinkeloe, N. Djordjevic, C. O. Paschereit, and K. Oberleithner. Mitigation of pressure fluctuations from an array of pulse detonation combustors. 2021.

[10] Variohm Eurosensor. Ept3100 pressure sensor. https://www.variohm.com/products/pressure-sensors/pressure-sensors/ept3100, 2025.

[11] Muller Instruments. Thermocouple mct 19. https://mueller-instruments.de/fileadmin/Downloads/instruments-medien/Heat_Flux_Thermocouple_MCT_web.pdf, 2025.

[12] Muller Instruments. Mfa 1000 amplifier. https://mueller-instruments.de/en/verstaerker/multi-funktions-verstaerker-mfa-1000/, 2025.

[13] Spark Plugs. Ngk spark plug c9e (7499). https://www.sparkplugs.co.uk/ngk-spark-plug-c9e-7499-2#:~:text=NGK%20Spark%20Plug%20C9E%2C%20NGK%20Stock%20Code%207499.,to%20find%20technical%20data%20and%20vehicle%20compatibility%20information, 2025.

[14] J. Kasahara, M. Hirano, A. Matsuo, Y. Daimon, and T. Endo. Thrust measurement of a multicycle partially filled pulse detonation rocket engine. 2009.

[15] Kistler. 9323aaa load cell. https://www.kistler.com/IT/en/p/piezoelectric-press-force-load-cell-9323aa/000000000018007666, 2025.

[16] Kistler. 5018a amplifier. https://www.kistler.com/IT/en/p/laboratory-charge-amplifier-5018a1000/000000000018004424, 2025.

[17] K. Goto, Y. Kato, K. Ishihara, K. Matsuoka, J. Kasahara, D. Nakata, K. Higashino, and N. Tanatsugu. Thrust validation of rotating detonation engine system by moving rocket sled test. 2020.

[18] PCB Piezotronics. Accelerometer model 353b34. https://www.pcb.com/products?m=353B34, 2025.

[19] Photron. Fastcam nova s-series s9. https://photron.com/fastcam-nova-s/, 2025.

[20] M. R. Haghdoost, C. O. Paschereit D. E.-Mitchell, and K. Oberleithner. High-speed schlieren and particle image velocimetry of the exhaust flow of a pulse detonation combustor. 2020.

[21] G. S. Settles and M. J. Hargather. A review of recent developments in schlieren and shadowgraph techniques. 2017.

[22] K. P. Rouser, P. I. King, F. R. Schauer, R. Sondergaard, L. P. Goss, and J. L. Hoke. Time-accurate flow field and rotor speed measurements of a pulsed detonation driven turbine. 2011.

[23] AFS Gs60-05 5-C series injector. Alternative fuel systems. https://advancedtruckparts.com/products/25-10010-4-genuine-afs-fuel-injector?, 2025.

[24] K. Wang and W. Fan. Efforts on high-frequency pulse detonation engines. 2017.

[25] K. Matsuoka, M. Esumi, J. Kasahara, and S. Ogawa. Study on valve systems for pulse detonation engines. 2010.

[26] Tamagawa Europe GmbH. Tamagawa seiki ts4613 electromagnetic motor. https://tamagawa.eu/products/servo-motors-drivers-controllers/tbl-iii-series-compact-size-ac-servo-motor/, 2025.

[27] K. Matsuoka, M. Esumi, K. B. Ikeguchi, J. Kasahara, A. Matsuo, and I. Funaki. Optical and thrust measurement of a pulse detonation combustor with a coaxial rotary valve. 2011.

[28] SMC Pneumatic. Akm2000-f01-a check valve. https://media.fluid24.eu//catalog/product/documents/8873_pim.pdf, 2025.

[29] WITT-Gasetechnik GmbH & Co. KG . Flashback arrestors f100n-es. https://www.wittgas.com/products/gas-safety-equipment/flashback-arrestors-flame-arrestors/for-pressure-regulators-outlet-points-inline/flashback-arrestor-f100n-es/, 2025.

[30] KROHNE. Isa 1932 critical flow nozzle. https://cdn.krohne.com/pick2/tagged_docs/CA_CATALOGUE_PRESSURE_en_201119.pdf?, 2019.

[31] Bosch. Fr8dpx spark plug. https://www.boschaftermarket.com/xrm/media/images/services/downloads/parts_14/spark_plugs_6/sp_glp_combi_catalog_multi_languages_94658.pdf, 2023.

[32] P. K. Panicker, D. R. Wilson, and F. K. Lu. Operational issues affecting the practical implementation of pulsed detonation engines. 2006.

[33] P. K. Panicker, J.-M. Li, F. K. Lu, and D. R. Wilson. Development of a compact liquid fueled pulsed detonation engine with predetonator. 2007.

[34] T. H. New, P. K. Panicker, K. F. Chui, H. M. Tsai, and F. K. Lu. Experimental study on deflagration-to-detonation transition enhancement methods in a pde. 2007.

[35] J. Tian, Y. s. Wang, J. z. Zhang, and X.-M. Tan. Numerical investigation on flow and film cooling characteristics of coolant injection in rotating detonation combustor. 2022.

[36] L. Sanchez de Leon, F. Sastre, E. Martin, and A. Velazquez. Reduced-order model for performance simulation and conceptual design of rocket-type pulse detonation engines. 2025.

[37] National Institute of Standards Technology. Nist-janaf thermochemical tables. https://janaf.nist.gov/, 1998.

[38] N.M. Marinov, C.K. Westbrook, and W.J. Pitz. Detailed and global chemical kinetics model for hydrogen. 1996.

[39] Motedis. Aluminum profile. https://www.motedis.co.uk/en/Aluminium-plate-10x90-mm, 2025.

[40] A. V. Cojocea, I. Porumbel, M. Gall, and T. Cuciuc. Experimental thrust and specific impulse analysis of pulsed detonation combustor. 2024.

[41] D. M. Valli and T.K. Jindal. Pulse detonation engine: Parameters affecting performance. 2004.

[42] S. Chander and T. K. Jindal. Pulse detonation propulsion system - pec chandigarh experience. 2014.

[43] Ardex Cemento. Epoxy paste (dp55). https://www.ardex.es/product/adipox-ep55/, 2025.

[44] CS Instruments. Cs instruments va 500 flowmeter. https://www.cs-instruments.com/va-500-flow-sensor-for-compressed-air-and-gases/, 2025.

[45] CS Instruments. Cs instruments vd 500 flowmeter. https://www.cs-instruments.com/cs-data/Bedienungsanleitungen/Instruction%20manuals_EN_new/Instruction_manual_VD_500_EN.pdf, 2025.

[46] LCM System. Sta-3 alloy steel s type tension compression load cell. https://www.lcmsystems.com/res/STA-3%20Alloy%20Steel%20Tension%20%20Compression%20Load%20Cell.pdf, 2025.

[47] Burster company. 9236 multichannel amplifier for strain gauge sensors. https://www.burster.com/en/products/p/detail/9236/, 2025.

[48] Maxim Integrated. Max291 butterworth 8-th order lowpass filter. https://www.analog.com/media/en/technical-documentation/data-sheets/MAX291-MAX296.pdf?ADICID=SYND_WW_P682800_PF-spglobal, 2025.

[49] Luminus. Luminus led pt-120-te. https://www.mouser.com/datasheet/2/245/Luminus_PT120TE_Datasheet-540282.pdf, 2025.

[50] Edmund Optics . 50mm diameter 120 grit ground glass diffuser. https://www.edmundoptics.com/p/50mm-diameter-120-grit-ground-glass-diffuser/26543/, 2025.

[51] BoWex-ELASTIC. Elastic coupling he-zs. https://www.ktr.com/fileadmin/ktr/media/Tools_Downloads/kataloge/05_Flanschkupplungen_BoWex_ELASTIC.pdf, 2025.

[52] Rollakin. O-ring or-13x2-ptfe - or-13x2-ptfe. https://www.123cuscinetti.it/getTechnicalSheetPdf/249827, 2025.

[53] Omron . Tl-q5mc1 z-ormon proximity sensor. https://www.dhm-online.com/sensori-vicinanza/10409-sensore-di-prossimita-induttivo-tl-q5mc1-z-omron.html, 2025.

[54] Beru. Beru zse150 ignition coil. https://www.mlperformance.eu/products/beru-zse150-ignition-coil, 2025.

[55] Siemens. 3sb3500-0aa12 button switch. https://www.onlinecomponents.com/en/productdetail/siemens-energy/3sb35000aa12-12373990.html, 2019.

[56] Omron. Relay 12 vdc g2r-1-e dc12. https://www.digikey.it/it/products/detail/omron-electronics-inc-emc-div/G2R-1-E-DC12/153649, 2025.

[57] Finder. Relay 220v ac serie 40.52. https://cdn.findernet.com/app/uploads/ZDPENXX4052.pdf, 2025.

[58] Mean Well. Power supply 12 vdc. https://us.rs-online.com/product/mean-well/hdr-30-12/70968779/#:~:text=MEAN%20WELL%20HDR-30-12%20Power%20Supply%2C%20AC-DC%2C%20DIN%20Rail%2C,input%20%28277VAC%20available%29%20and%20provides%20complete%20models%20%285V%2F12V%2F15V%2F24V%2F48V%29.?msockid=282fc3688b7d696f2019d3a88f7d6b19, 2025.

[59] PCB . Accelerometer conditioner model 480b21. https://www.pcb.com/products?m=480B21, 2025.

[60] Texas Instruments. Operational amplifier opa627ap. https://www.heisener.com/ProductDetail/OPA627AP, 2025.

[61] National Instruments. Pxie-6133 daq. https://www.ni.com/docs/en-US/bundle/ni-6132-6133-specs/resource/371231d.pdf, 2023.

[62] National Instruments. Pxie-8130 controller. https://www.ni.com/pdf/dspdf/en/ds-231, 2014.

[63] National Instruments. Pxie-1062q chassis. https://www.ni.com/docs/en-US/bundle/pxie-1062q-specs/page/specs.html, 2023.

[64] National Instruments. Nni-9401 ttl control. https://www.ni.com/it-it/shop/model/ni-9401.html, 2025.

[65] DIM. Stainless steel spirals. https://www.dim-international.com/en/catalogue/, 2025.

[66] Grundfos. Cr 5-10 water pump. https://product-selection.grundfos.com/es/products/cr-cre-cri-crie-crn-crne-crt-crte/cr/cr-5-10-96455260?pumpsystemid=2650873869&tab=variant-specifications, 2025.

[67] HpControl. Dn50 pn40 a251 ball valve. https://hpcontrol.uk/elektrozawor-kulowy-2-cale-dn50-silownik-a251.html?___SID=S, 2025.

[68] Parker. 8m-c8l check valve. https://ph.parker.com/us/es/product/check-valvepoppet-valve-c-series/8m-c8l-25-ss, 2025.

[69] T. H. New, P. K. Panicker, F. K. Lu, and H. M. Tsai. Experimental investigations on ddt enhancements by shchelkin spirals in a pde. 2006.

[70] F. Y. Zhang, T. Fujiwara, T. Miyasaka, E. Nakayama, T. Hattori, and R. K. Hanson. Detonation studies of high- frequency- operation pulse detonation engine with air/hydrogen. 2003.

[71] T. R. Meyer, J. L. Hoke, M. S. Brown, J. R. Gord, and F. R. Schauer. Experimental study of deflagration-to-detonation enhancement techniques in a h2/air pulsed-detonation engine. 2002.

[72] Z. Xiao, J. Lu, L. Zheng, W. Tan, and Q. Li. Performance analysis of a pulse detonation turbine engine based on unsteady finite-time model. 2023.

[73] V. Buyakofu, K. Matsuoka, K. Matsuyama, and A. Kawasaki. Flight demonstration of pulse detonation engine using sounding rocket s-520-31 in space. 2022.

[74] F. Ma, J.-Y. Choi, and V. Yang. Thrust chamber dynamics and propulsive performance of single-tube pulse detonation engines. 2005.

[75] K. M. Pandey and P. Debnath. Review on recent advances in pulse detonation engines. 2015.

[76] M. Warimani, M. H. Azami, A. F. Ismail, and A. K. Ariffin. Numerical simulation of a pulse detonation engine with hydrogen fuels. 2002.

[77] E. Wintenberger, J.M. Austin, M. Cooper, S. Jackson, and J.E. Shepherd. An analytical model for the impulse of a single-cycle pulse detonation tube. 2003.

[78] S. M. Frolov, V. I. Zvegintsev, V. S. Aksenov V.S. Ivanov, I. O. Shamshin, D.A. Vnuchkov, D. G. Nalivaichenko, A.A. Berlin, and V.M.Fomin. Continuous detonation combustion of hydrogen: Results of wind tunnel experiments. 2018.

[79] S. Gordon and B. J. McBride. Computer program for calculation of complex chemical equilibrium compositions and applications, 1994.

[80] M. H. Azami and M. Savill. Pulse detonation assessment for alternative fuels. 2016.

[81] F. Ma, J.-Y. Choi, and V. Yang. Propulsive performance of airbreathing pulse detonation engines. Technical report, 2006.

[82] Q. Zhang, X. Qiao, W. Fan, K. Wang, F. Tan, and J. Wang. Study on operation and propulsion features of a pulse detonation rocket engine with secondary oxidizer injection. 2020.

[83] N. Alam, K. K. Sharma, and K. M. Pandey. Numerical investigation of combustion phenomena in pulse detonation engine with different fuels. 2018.

[84] D. Schwer and K. Kailasanath. Fluid dynamics of rotating detonation engines with hydrogen and hydrocarbon fuels. 2012.

[85] K. Kailasanath. Recent developments in the research on rotating-detonation-wave engines. 2017.

[86] F. Ma, J.-Y. Choi, and V. Yang. Internal flow dynamics in a valveless airbreathing pulse detonation engine. 2008.

[87] NASA. Cearun. `https://cearun.grc.nasa.gov/`.

[88] F.R. Schauer, C.L. Miser, K.C. Tucker, R.P. Bradley, and J.L. Hoke. Detonation initiation of hydrocarbon-air mixtures in a pulsed detonation engine. 2005.

[89] K. Wang, W. Fan, W. Lu, Q. Zhang, F. Chen, C. Yan, and Q. Xia. Propulsive performance of a pulse detonation rocket engine without the purge process. Technical report, 2014.

[90] M. L. Fotia, F. Schauer, T. Kaemming, and J. Hoke. Experimental study of the performance of a rotating detonation engine with nozzle. 2015.

[91] Japan Aerospace Exploration Agency, Muroran Institute of Technology, Nagoya University, and Keio University. Propulsive performance and heating environment of rotating detonation engine with various nozzles. 2018.

[92] S.-Y. Huang, J. Zhou, S.-J. Liu, H.-Y. Peng, and X.-Q. Yuan. Continuous rotating detonation engine fueled by ammonia. In *11th Propulsion Conference*, 2022.

[93] I. V. Walters, C. L. Journell, A. Lemcherfi, R. M. Gejji, S. D. Heister, and C. D. Slabaugh. Operability of a natural gas–air rotating detonation engine. 2019.

[94] Z. Xia, H. Ma, G. Ge, S. Liu, C. Zhou, and Y. He. Visual experimental investigation on stable operating process of the plane-radial rotating detonation engine. Technical report, 2020.

[95] Nagoya University and Japan Aerospace Exploration Agency. Propulsion performance of cylindrical rotating detonation engine. Technical report, 2019.

[96] H. Qiu, C. Xiong, and J. Li. A theoretical and 1-d numerical investigation on a valve/valveless air-breathing pulse detonation engine. 2020.

[97] S. Carter, A. Ned, J. Chivers, and A. Bemis. Selecting piezoresistive vs. piezoelectric pressure transducers. 2018.

[98] K. Wang, W. Fan, X.-D. Zhu, Y. Yan, and Z. Gao. Experimental investigations on effects of wall-temperature on performance of a pulse detonation rocket engine. 2013.

[99] S. M. Frolov, I. O. Shamshin, V. S. Aksenov, V. S. Ivanov, and P. A. Vlasov. Ion sensors for pulsed and continuous detonation combustors. 2023.

[100] C. Welch, D. Depperschmidt, R. Miller, J. Tobias, M. Uddi, and A. K. Agrawal. Experimental analysis of wave propagation in a methane-fueled rotating detonation combustor. 2018.

[101] R. J. McMillan. Shock tube investigation of pressure and ion sensors used in pulse detonation engine research. 2004.

[102] API Plus. Air tank serb0010-or-inox316l. `https://www.apiplus.it/it/homepage/serbatoi/serbatoi-inox/serbatoio-aria-compressa-inox-316l-10-litri-orizzontale`, 2025.

[103] Air Liquide. Nitrogen tan alphagaz 1. `https://es.airliquide.com/gases/alphagaztm-1-nitrogeno/P0271`, 2025.

[104] Rehm Dichtungen Ehlers GmbH. Ptfe seals. `https://rehmdichtungen.de/en/materials-and-materials/plastic-seals/ptfe-seals/`, 2025.

[105] A. B., T. Cuciuc, A. V. Cojocea, M. Gall, and C. E. Hritcu. Experimental pressure gain analysis of pulsed detonation engine. Technical report, 2024.

[106] National Instruments. 781402-200 cable, fibre optic. `https://es.farnell.com/ni/781402-200/cable-control-remoto-chasis-200m/dp/3620176?`, 2025.

[107] E. Wintenberger and J.E. Shepherd. Model for the performance of airbreathing pulse-detonation engines. 2006.

[108] K. Aizawa, S. Yoshino, T. Mogi, H. Shiina, Y. Ogata, Y. Wada, and A. K. Hayashi. Study of detonation initiation in hydrogen/air flow. 2008.

[109] X. Zhang, H. Sun, D. Guo, Y. Gou, L. Ma, and S. Yong. Buckling behavior and failure mechanism of gas pipeline in explosive shock wave environment. 2024.